Utility of kidney organoids for disease modeling and therapeutic development

Louisa Helms

A dissertation

submitted in partial fulfillment of the

requirements for the degree of

Doctor of Philosophy

University of Washington

2022

Reading Committee:

Benjamin S. Freedman, Chair

Shreeram Akilesh

Michael Regnier

Program Authorized to Offer Degree:

Molecular Medicine and Mechanisms of Disease

University of Washington

Abstract

Utility of kidney organoids for disease modeling and therapeutic development

Louisa Helms

Chair of the Supervisory Committee:
Dr. Benjamin S. Freedman, Associate Professor
Department of Medicine, Division of Nephrology, Department of Lab Medicine & Pathology, Kidney Research Institute, Institute for Stem Cell and Regenerative Medicine, and Department of Bioengineering

Chronic kidney disease (CKD) affects 1 in 7 adults and is the 10th leading cause of death in the United States in 2022. Kidney transplant and dialysis remain the leading treatment strategies for kidney failure despite their expensive and outdated technological innovation. Stem cell derived human kidney organoids aim to provide a vital tool to study complex diseases ranging from infectious to genetic, and a translationally relevant system to discover and probe novel therapeutic pathways to improve our ability to treat kidney disease.

CKD is the greatest risk factor for developing severe COVID-19, the 3rd leading cause of death in the US in 2022, and severe acute respiratory syndrome coronavirus 2 (SARS-CoV-2) infection has been reported to cause acute kidney injury in 1 in 4 hospitalized COVID-19 patients. Utilizing genome-edited kidney organoids, SARS-CoV-2 variants, and clinical data, we investigated viral tropism, mechanism, and therapeutic approaches in the context of the kidney. SARS-CoV-2

infected proximal tubules in kidney organoids via angiotensin converting enzyme 2 (ACE2). Infected organoids produced replication competent virus and displayed apoptotic responses in the context of polycystic kidney disease (PKD), a genetic cause of CKD. Cross-validation of gene expression patterns in organoids reflects proteomic signatures of COVID-19 in the urine of critically ill patients indicating interferon pathway upregulation. SARS-CoV-2 viral variants alpha, beta, gamma, kappa, and delta exhibit comparable levels of infection in kidney organoids. Replication is reduced by remdesivir treated and infection blocked by treatment with de novo–designed spike binder peptides. This work clarifies the impact SARS-CoV-2 infection has on the kidney and enables the assessment of viral fitness and emerging therapies in the context of infectious disease.

Autosomal dominant PKD is a genetic kidney disease affecting 1 in every 400-1000 people worldwide, causing progressive fluid-filled cyst production followed by fibrosis in the kidneys, liver, and other organs, resulting in organ failure. PKD is caused by mutations in the polycystin proteins polycystin-1 (PC1) or polycystin-2 (PC2), but the molecular pathway causing cystogenesis remains elusive. Genome-edited PKD organoids phenocopy cystogenesis and previously identified that the myosin inhibitor blebbistatin resulted in cyst enlargement. I discovered that treatment with the myosin activator, EMD 57033 (EMD), prevented cyst growth and that treatment when cysts were already established was able to slow cyst expansion. Live-imaging of EMD-treated organoids expressing fluorescently-tagged non-muscle myosin II B (NMIIB-GFP) revealed increased apical-basal tubule contractility of PKD organoid tubules compared to controls, indicating that the PKD organoid tubules were poised to contract and may have intrinsic contractile dysfunction. Analysis of the slowly progressing *Pkd1*$^{RC/RC}$ mouse model

reveals a concomitant expansion of phosphorylated myosin light chain 2 (pMLC2) expressing stromal pericytes and cyst growth, suggesting that a therapeutic reducing pMLC2 expression may rescue kidney fibrosis later in disease. Together, this work suggests both a tubular and stromal myosin contribution to PKD pathogenesis that can be therapeutically targeted using myosin activators early in disease and pMLC2 inhibitors in later stage disease progression.

In conclusion, our studies of PKD and COVID-19 reveal great utility of kidney organoids for disease modeling and therapeutic development, advancing the translational applications of organoid technology.

TABLE OF CONTENTS

LIST OF FIGURES

LIST OF TABLES

ACKNOWLEDGEMENTS

I would like to first acknowledge my scientific mentor Beno Freedman and the rest of the Freedman lab for creating a scientific environment where we can try new things and investigate challenging scientific questions. Nelly Cruz and Ivan Gomez for providing me with hands on training and mentorship in the lab. Courtney Vishy, Sophie Blackburn, and Thomas Vincent for being supportive fellow grad students along for the same bumpy ride that getting a PhD entails. Michael Emerman and Molly OhAinle for teaching me how to be a good scientist early and giving me the structure to approach scientific questions thoughtfully and in an organized fashion. Mimi Krutein, Darrian Bugg, Chelsea Fortin, and Charlotte James for providing me with senior guidance and wisdom along the way.

Additionally, I would like to acknowledge the extra mentors I picked up along the way: Jessica Roberto, Will Canestaro, Kim Emmons, Teddy Johnson, Emer Dooley, Charlotte Hubbert, and Shiri Levy who have helped me shape my career trajectory. Without their guidance I would not have the confidence or know how to be able take on a career in scientific business development.

I would like to acknowledge my family for always pushing me to take on new challenges and to put in the work no matter what. And finally, my husband for supporting me when I take on more than I can handle, for reminding me that our goals are tangible, and for enforcing breaks so that I don’t burn out. Without you I would not be who I am today.

DEDICATION

This thesis is dedicated to all the young scientists facing imposter syndrome: you are smart enough I promise.

Chapter 1. INTRODUCTION

1.1 KIDNEY FUNCTION AND DEVELOPMENT

The kidney is one of the most complex organs in the body, containing more than 26 different cell types in the adult kidney (1–3). The kidneys function primarily as filtering units: properly balancing excess salt, fluids, metabolic waste products, and toxins, resulting in urinary filtrate. In addition to filtering, the kidneys also regulate blood pressure, blood pH, contribute to the production of red blood cells, and produce hormones and enzymes for daily life function (4). The kidney is comprised of approximately one million nephrons of which each individual nephron is comprised of a glomerulus, specially organized proximal and distal convoluted tubules interspersed with veins and arteries to exchange and resorb solutes, and a collecting duct system which feeds waste into the ureter to be excreted as urine (Fig. 1.1).

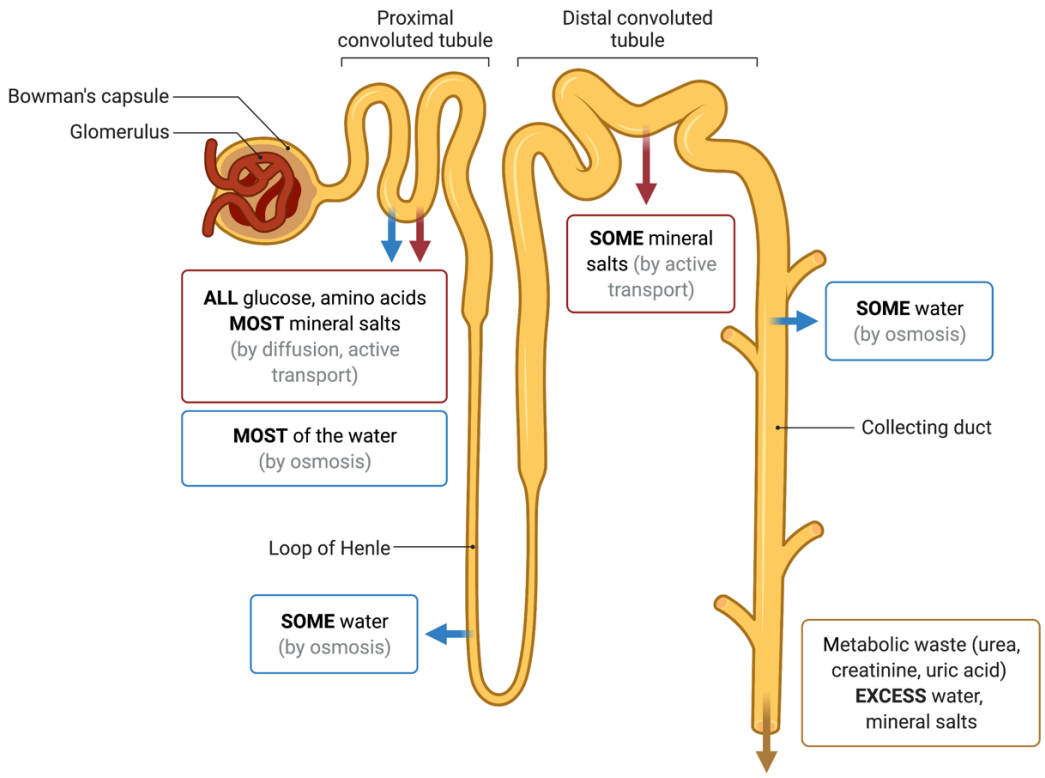

Figure 1.1 Structure and function of the human kidney nephron.
Adapted from Biorender. Physiological filtering functions of the human nephron divided by their individual compartments.

As blood flows into each nephron, the blood enters the tightly clustered glomerulus where smaller molecules, wastes, and fluid are passed into the tubule, while the larger molecules, including protein and blood cells who are larger than the 6-8 nm and 30-50 kDa glomerular filtration barrier cutoff stay within the blood vessel (5). Within the glomerulus, podocytes and glomerular endothelial cells sandwich the glomerular basement membrane (GBM) while mesangial cells provide structural support. The GBM together with the podocytes and endothelial cells comprise the glomerular filtration barrier (GFB) which is responsible for keeping cells and large biomolecules within the circulation while allowing water and small solutes to pass freely into the glomerular ultrafiltrate (6). After passing through the GFB, fluid enters the proximal convoluted

tubule (PCT) where 70% of the glomerular filtrate and its solutes are reabsorbed in the proximal tubules via both active and passive transport. Past the PCT, fluid enters the loop of Henle which has a descending and ascending limb which vary in their permeability and contribute primarily to electrolyte (ascending) and water (descending) reabsorption. Past the loop of Henle, filtrate enters the distal convoluted tubule (DCT) which filters similarly to the PCT to maintain pH and sodium-potassium levels in the blood. The DCT is the terminus of the nephron and connects to the collecting duct whereby electrolytes and pH are rebalanced, and water is reabsorbed to produce a concentrated urine product that gets excreted into the bladder via in the ureter.

During development, the kidney originates from the mesoderm and is derived from two progenitor cell populations: the metanephric mesenchyme (MM) which give rise to nephrons, and the ureteric bud (UB) which give rise to the collecting ducts and ureter. During development, the UB and MM produce and respond to an intricate network of stimulatory and inhibitory signals that concomitantly induce each segments growth. Metanephric development begins at week 5 of human gestation and embryonic day 10.5 in mice, where the majority of kidney development signalling has been investigated, in which Paired Box 2 (Pax2), EYA Transcriptional Coactivator and Phosphatase 1 (Eya1), Odd-Skipped Related 1 (Osr1), and Wilms Tumor 1 (Wt1) expression drive metanephric induction (7). Glial cell line derived neurotrophic factor (GDNF) secretion from the MM drives ureteric budding which is tightly regulated by Bone Morphogenetic Protein 4 (Bmp4) expressing cells in the Wolffian duct directly adjacent to the ureteric bud to prevent unnecessary branching (8). Ret Proto-Oncogene (c-Ret) and Glial Cell Line Derived Neurotrophic Factor Receptor α1 (Gfrα1) receptors on the ureteric bud tips respond to GDNF signaling from the MM to trigger MM invasion resulting in ureteric branches that develop condensed MM cells on their

tips to form the cap mesenchyme (7). Nephrogenesis begins when the cap mesenchyme forms, containing Sine Oculis-Related Homeobox 2 (Six2) expressing cells that maintain the cap mesenchyme developmental state (9). Wingless Type Family Member 9b (Wnt9b) is secreted from the UB epithelium which induces a mesenchymal to epithelial transition (MET) of the Six2+ cap mesenchyme progenitor cells into pre-tubular aggregates (10). These aggregates are subsequently triggered to differentiate into renal vesicle cells via exposure to wingless-type MMTV Integration Site Family Member 4 (Wnt4) and Fibroblast Growth Factor 8 (Fgf8) (10, 11). Epithelial renal vesicles polarize and elongate to form comma- and S-shaped bodies which then fuse with the Pax2 expressing UB tip epithelium to form the nephron (12) (Fig. 1.2). After fusion, segmentation, and maturation into specialized nephron compartments, nephrogenesis in humans is complete by week 36 of gestation, and post-natal day 2 in mice (13).

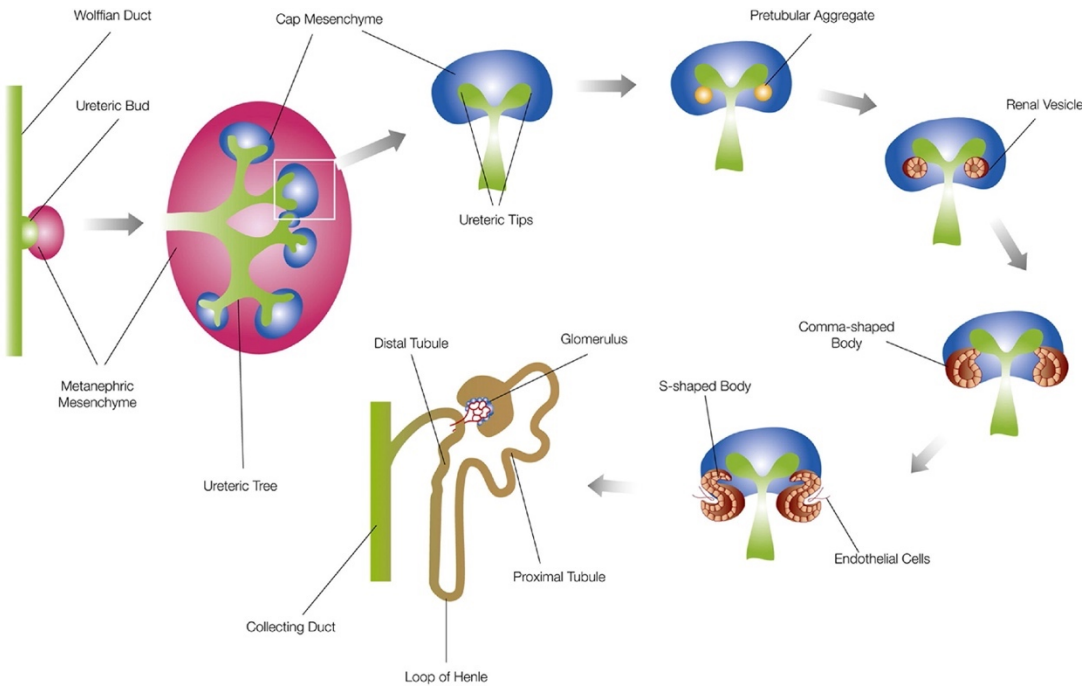

Figure 1.2 Diagram of prenatal morphologic states during kidney development Adapted from Walker et al (7). Ureteric bud and metanephric mesenchyme progenitor cells emerge from the Wolffian duct, branching morphogenesis of the ureteric tips give rise to cap mesenchyme structures containing pretubular aggregates. These aggregates further differentiate

into renal vesicles which give rise to all epithelial components of the nephron through comma- and S-shaped body formation, nephron maturation, and final fusion with the original ureteric stalk which gives rise to the collecting duct.

Due to the origins of the MM from the cap mesenchyme, a short-term developmental component of the kidney, the regenerative capabilities of the kidney are limited; new nephrons in the mammalian kidney cannot develop spontaneously and reconstructing the complex anatomy of the kidney would be extremely challenging (14). Studies examining the kidney's responses to damage via partial nephrectomy and obstruction of the ureter demonstrate that the kidney can reconstruct and repair tubules in response to short-term damage, but cannot form glomerular filtration units or entire new nephrons (15, 16). Long-term genetic lineage tracing and clonal analysis of the adult mammalian kidney demonstrate that there are some WNT-responsive cells that produce fate-restricted self-renewal of the kidney, but these cells are primarily limited to tubular components of the nephron (17). Given this limited capacity of to regenerate, chronic injury to the kidney results in irreversible damage that leads to fibrosis, scarring, and end-stage renal failure which can only be treated with renal replacement therapy via dialysis or renal transplant (18). Considering chronic kidney disease affects 14.4% of the U.S. adult population surveyed in 2015-2018 in the National Health and Nutrition Examination Survey and mortality is at an all-time low for patients with end stage renal disease, there is a dramatic need for improved treatments and solutions for patients with kidney disease (19).

1.2 Kidney Organoids

The kidneys are a highly complex organ containing many specialized cell types. Single cell cultures, while useful, do a poor job recapitulating the complexities of human organs, and *in vivo*

models are convoluted by species differences when assessing human diseases. To improve our ability to model complex tissues in vitro, stem cell derived organoids have emerged as an appealing model system for many different human tissues. Organoids were made possible from years of intensive study of human embryonic development and stem cell research. In 1998, the first embryonic stem cell (ESC) line was derived from a human blastocyst and was found to be proliferative and able to differentiate into the three germ layers required for human development (20). In 2006, induced pluripotent stem cells (iPSCs) were reprogrammed from human fibroblasts via the transduction of Organic Cation Transporter 3/4 (OCT3/4), Sex Determining Region Y-box 2 (SOX2), Kruppel Like Factor 4 (KLF4), and MYC Proto-Oncogene (c-MYC), generating an indispensable resource for regenerative PSCs that can be derived from unique patient populations to study diseases in a patient-specific way (21, 22). Both, ESCs and iPSCs share an unlimited proliferative ability and the pluripotent potential to differentiate into any human developmental structure barring extraembryonic cells, thus opening the potential for human-derived organ generation in vitro.

Many early efforts were made to guide PSC differentiation resulting in the generation of endodermal, mesodermal, and ectodermal cells (21, 23, 24). However, many of these efforts were performed in monolayer cell cultures which do not contain the highly specialized tissue architecture required for human gastrulation. To generate more three-dimensional (3D) tissue structures, biologists employed 3D differentiation strategies paired with chemical agonists and antagonists of developmental pathways which led to the creation of more organ-like complex 3D tissue structures referred to as organoids (25–28). While differentiation protocols differ depending upon the organ of interest, organoid formation involves three important steps: signaling pathway

activation or inhibition, media formulation changes to facilitate maturation and terminal differentiation, and a culture system that allows organoid growth in a 3D environment: cell aggregation or embedding into a matrix are typically employed (29).

As mentioned above, the human kidney derives from the mesoderm and stems from two progenitor populations: the MM and UB. To generate MM derived organoids, multiple differentiation protocols have emerged aimed to recapitulate nephron formation, all utilizing inhibition of Glycogen Synthase Kinase-3β (GSK3β) via CHIR99021 (CHIR) and wingless-related integrate site (WNT) signaling to induce an epithelial to mesenchymal transition (EMT) of the original stem cells followed by a mesenchymal to epithelial transition (MET) required for nephron formation (28, 30, 31). Depending on how the original stem cell cultures were cultivated dictates how the later differentiation protocols proceed. If the stem cells are cultured as matrix embedded spheroids, B27-supplemented media containing vitamins, hormones, and molecules for cell proliferation without requiring serum is given to post CHIR-stimulated cells to induce spontaneous MET and nephrogenesis (Fig. 1.3) (28). If cultured as a monolayer, subsequent activin and FGF9 stimulants are given with the option of transferring to 3D floating culture (30). Or conversely, monolayer stem cells can be stimulated with CHIR, then exposed to FGF9/BMP7/Retinoic acid and then cultured in Albumin Folyvinylalchohol Essential Lipids (APEL) media (31). All three differentiation strategies produce kidney organoids that share common nephron-like features resembling the glomeruli, segmented tubules, and interstitial cells. However, these nephron-like structures are developmentally immature, mapping closest to developing kidneys in RNAseq analyses (31–33).

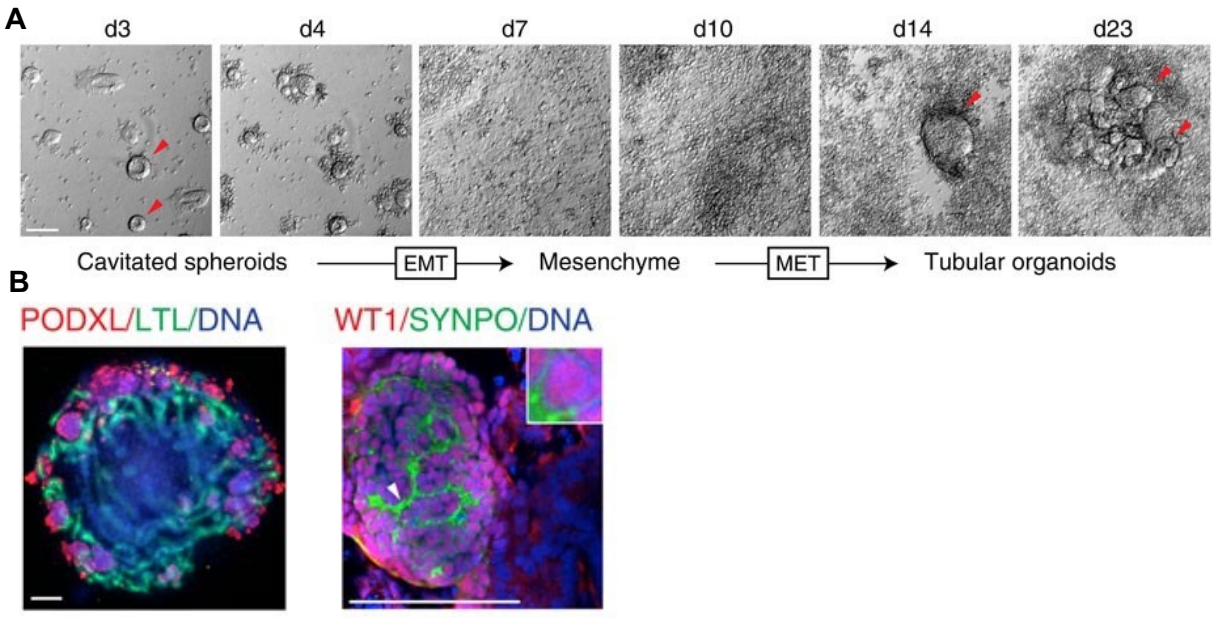

Figure 1.3 Stem cell derived kidney organoids form nephron structures. Adapted from Freedman et al (28) A. Schematic of kidney organoid differentiation protocol resulting in tubular structures visible by brightfield microscopy. B. Immunofluorescent images of kidney organoids expressing podocalyxin (PODXL) representing podocytes found in the glomerulus, lotus tetragonolobus lectin (LTL) representing the proximal tubules, WT1, and synaptopodin (SYNPO) further representing podocytes found in the glomerulus, and together, demonstrating specialized nephron cell expression.

MM nephron organoids do not contain UB cell types due to fundamental differences in progenitor cell differentiation signaling and cellular organization. First attempts at making UB organoids began by inducing PSCs into intermediate mesoderm, Wolffian duct, and finally to UB cells through stepwise stimulant treatment and Matrigel embedding, generating UB-like structures expressing RET, GATA3 and PAX2 (34). However, these structures failed to demonstrate robust branching represented in mammalian UB tissues. To increase branching, follow up work optimizing the differentiation to mimic nephric duct formation demonstrated that manual separation and reconstitution of organoid tips resulted in branching morphogenesis that could

branch up to 20 times and expressed RET, GATA3, and very-low density lipoprotein (VLDL) receptor expression unique to UB tip regions (35).

Recent work using a different UB organoid differentiation protocol were used to develop collecting duct (CD) organoids using a dual-reporter stem cell line fluorescently expressing *PAX2* and *WNT11*. Dual reporter stem cells were cultured for 7 days in UB induction medium, fluorescence-activated cell sorting (FACS) sorted for *PAX2* expression at day 7 and placed into 3D culture conditions until detectable levels of *WNT11* were expressed and branching morphology was observed (36). UB organoids expressed UB-specific genes *SOX9* and Cadherin 1 (*CDH1*) to confirm cell-type specificity. This protocol was then optimized to be used with non-reporter iPSCs for ubiquitous use. Using this protocol, UB organoids were subsequently differentiated into CD organoids via exposure to optimized CD differentiation medium resulting in a reduction of *WNT11* expression, an increase in Aquaporin 3 (*AQP3*) and Forkhead Box I1 (*FOXI1*) expression, indicating CD-specific type expression, albeit an immature one (36). Interestingly, a nephron progenitor cell 3D cavity and cultured UB organoid tip were co-cultured together resulting in extensive branching, generation of nephron-like cells, and luminal interconnection between the nephron and CD expressing structures, suggesting an ability for holistic *in vitro* kidney modeling (36).

Very recently, a report of organotypic kidney organoids derived solely from ESCs was published suggesting the importance of stromal cells in contributing to organoid structural complexity and maturity (37). In their protocol, mouse ESCs were differentiated into three progenitor populations representing the MM, UB, and stromal progenitors (SP). A mixture of the MM and SP populations

were mixed and plated into low-bind U-bottom plates and then a micro-dissected UB epithelial bud was added to the cell mixture to induce spheroid aggregation. After 7 days of culturing, the resulting organoids exhibited UB branching with MM cells organized at the UB tips, glomeruli, proximal, and distal tubule cells inside the organoid body, and stromal organization replicative of the corticomedullary kidney pattern. While these organizational patterns were more mature than alternative organoid protocols, scRNA-seq analysis still revealed cellular signatures that mimic the embryonic kidney (37). While these advancements in kidney organoid culture have the promise to better recapitulate the cellular and structural complexities of the kidney, maturing these structures remains a significant hurtle in our ability to model the adult kidney.

1.3 Translational Applications of Organoids

Since the first invention of Leucine Rich Repeat Containing G protein-coupled Receptor 5 (Lgr5) positive stem cell derived intestinal organoids in 2009, organoids have proved to be critical research tools for modeling human development and human diseases (38). Organoids provide more cellular and structural complexity that 2D cell models and a human origin that animal models fail to recapitulate. Due to the significant advancements and applications of developmental biology, stem cell biology, and cellular engineering, stem cell derived organoids can be used for disease modeling, host-pathogen interactions, therapeutic development, personalized medicine, and regenerative medicine (Fig. 1.4) (39).

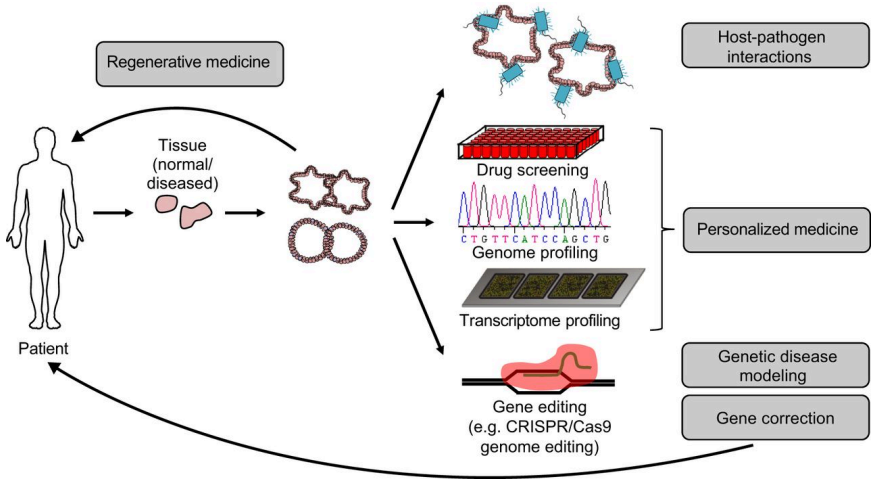

Figure 1.4 Applications of stem cell derived kidney organoids.

Adapted from Drost et al (39). Representative schematic of translational organoid applications.

Since the invention of kidney organoids in 2015, major advancements have been made in kidney organoid research. iPSCs derived from patients with genetic kidney disease and CRISPR/Cas9 gene edited iPSCs have been used to study autosomal dominant and autosomal recessive polycystic kidney disease (PKD), cystinosis, nephronophthisis-related ciliopathy syndrome, mucin 1 kidney disease, and Apolipoprotein L1 (APOL1) risk allele mediated chronic kidney disease (28, 40–46). Utilizing these kidney organoid-based disease models, novel disease pathways have been investigated, therapeutics can be assessed for disease-specific efficacy and high throughput application, and gene therapy methods are being developed for genetic rescue.

While many of these organoid applications are aimed to develop disease specific therapeutics, animal models are still required to validate safety and efficacy of therapeutic interventions prior to human clinical trials due to the immaturity and reduced physiological complexity of current organoid model systems. To improve this limitation of the kidney organoid model system, work has been devoted to developing improved vascularization methods to induce more mature kidney structures and mimic the interspersed vascular network of the kidney (33, 47). Additionally,

kidney-on-a-chip systems are being developed to mimic the structural, mechanical, and physiological properties of the kidney to overcome the spontaneous heterogeneity of organoid cultures (48, 49).

Due to the limited regenerative capabilities of the human kidney, kidney organoids and their progenitor cells promise an appealing untapped cell therapy resource to reduce the reliance upon human organ donors for treating kidney failure. One approach to generating transplantable human kidney tissue aimed to generate a mesenchymal stem cell derived human kidney in an animal with the goal of growing of autologous transplantable tissue (50). Others have focused on direct cell transplantation from either differentiated kidney organoids or nephron progenitor cells derived from PSCs that were transplanted under mouse renal capsules which has increased vascularization of human-derived implants (51–53). While all these methods showed varying degrees of successful implantation, integration into mouse kidneys, and differentiation, they were all fraught with unwanted non-kidney cellular growth and immature cellular organization and are low in throughput (54). While methods of kidney progenitor and kidney organoid transplantation are still early in development, the first gene-edited porcine kidney xenograft was transplanted into a brain-dead human and demonstrated stable reperfusion, vascular integrity, and production of urine, suggesting that the potential for xenotransplantation may happen in the near-future (55).

The kidneys are targets of a variety of different pathogens with which organoids can be used to investigate host-pathogen interactions and responses to infection. Using lipopolysaccharide (LPS), Sepsis-associated acute kidney injury (SA-AKI) was modeled in kidney organoids, revealing changes in oxidative stress, enhanced apoptosis, and LPS-induced apoptosis of podocytes and

proximal tubular cells (56). Interestingly, human immunodeficiency virus (HIV) has been shown to infect and replicate within renal cells and cause HIV-associated nephropathy (HIVAN), however, no kidney organoid models have been employed to study this phenomenon to date (57). In the current pandemic, Severe acute respiratory syndrome coronavirus 2 (SARS-CoV-2) has been shown to infect proximal tubules of kidney organoids and organoids have been used to evaluate efficacy of developing therapeutics (58–61).

Together, kidney organoids provide a flexible and biologically complex platform to investigate challenging scientific questions that 2D and mono-cellular culture fail systems are unable to answer. This dissertation will explore kidney organoid applicability to multiple translational research questions spanning from viral-host interactions to drug development with the ultimate goal of improving the field's understanding of kidney biology as a whole.

Chapter 2. CROSS-VALIDATION OF SARS-COV-2 RESPONSES IN KIDNEY ORGANOIDS AND CLINICAL POPULATIONS

2.1 INTRODUCTION

SARS-CoV-2, first detected at the end of 2019 in the Hubei province of China, has spread worldwide causing the coronavirus disease, COVID-19 (62). Despite substantial progress and therapeutic innovation, COVID-19 continues to spread and impact the globe. SARS-CoV-2

belongs to the viral family *Coronaviridae* in which three new coronaviruses have emerged from animal reservoirs in the past two decades causing serious illness and death: SARS-CoV, Middle East respiratory syndrome coronavirus (MERS-CoV), and now SARS-CoV-2 (63). In addition to respiratory distress, patients with COVID-19 exhibit systemic symptoms that involve the kidneys, similarly to previous SARS-CoV and MERS-CoV outbreaks (64–66). Chronic kidney disease and its causes such as hypertension and diabetes are noted risk factors for developing severe COVID-19 disease, and additionally COVID-19 patients frequently develop acute kidney injury (AKI) (64, 67). Angiotensin-converting enzyme 2 (ACE2) is the primary entry receptor for SARS-CoV-2 in many experimental models and is strongly expressed in the proximal tubular epithelial cells of the kidney, implicating the kidney as a direct target for SARS-CoV-2 infection (68–72). Multiple autopsy reports have suggested SARS-CoV-2 infection of the kidney, and several groups have isolated SARS-CoV-2 from infected patient urine, however, it remains unclear whether direct infection of the kidney is responsible for AKI and severity of COVID-19 disease, versus systemic effects resulting from pulmonary distress (73–78).

Human cellular and organoid model systems have played a valuable role in our understanding of SARS-CoV-2 infection mechanisms, interactions with key target organs, and the efficacy of COVID-19 therapeutics as they provide more complex physiological compositions and behaviors than standard 2D culture (58, 79–84). Human models are particularly valuable because mice are not generally susceptible to SARS-CoV-2 since the virus cannot bind to the mouse Ace2 receptor (85). Kidney organoids are segmented structures that resemble primitive nephrons, which can be differentiated *in vitro* from human pluripotent stem cells, including induced pluripotent stem (iPS) cells and embryonic stem (ES) cells (28, 30, 31, 86). These organoid cultures contain diverse cell

types in patterned, well-differentiated structural arrangements, an advantage over traditional primary cultures which consist primarily of dedifferentiated proximal tubular cells. Because human pluripotent stem cells are immortal, they are readily amenable to genome editing to produce isogenic pairs of mutant and control cell lines, enabling reconstitution of hereditary disease phenotypes such as polycystic kidney disease cystogenesis in derived organoids (28). Such cell lines cannot be readily established from primary cultures which typically senesce rapidly and have a much more limited proliferative potential (84). SARS-CoV-2 can infect kidney organoid cultures, a property that has been leveraged to test candidate therapeutics (58, 82). Because organoids contain multiple cell types, additional experiments are needed to determine which of these cell types are specifically infected by using novel fluorescence-reporter SARS-CoV-2 variants (32, 33, 87, 88). The ability to co-localize SARS-CoV-2 infection with markers of apoptosis would provide critical insight into whether infection can produce direct cytotoxic effects simulating AKI, which were not detected in a recent study of somatic-derived kidney spheroids (59). It is also important to further apply this system to compare to clinical cohorts, viral variants of concern, and screen candidate therapeutics for safety and efficacy related to kidney disease.

Therefore, application of genome edited organoids to SARS-CoV-2 presents valuable opportunities to determine mechanisms of viral infection and assess the impact of pre-existing disease states (28, 79, 89–91). In this study, we cross-validate SARS-CoV-2's impact on kidney organoids and clinical data to investigate tropism, mechanism, and therapeutics. These findings provide clear evidence of SARS-CoV-2's kidney tropism, acute cytopathic effects, systemic and kidney-specific proteomic responses, and efficacy of COVID-19 therapeutics.

2.2 Materials and Methods

Cell Generation. Experiments were performed using wild-type WTC11 iPS and H9 ES cell lines, and a single *PKD2*$^{-/-}$ and two *ACE2*$^{-/-}$ clones (WTC11 background), generated and characterized as described previously (28, 79). Altogether these represent two distinct genetic backgrounds, genders, and cell types: (i) male WTC11 iPS cells (Coriell Institute Biobank, GM25256) and (ii) female H9 ES cells (WiCell, Madison Wisconsin, WA09).

Kidney organoid differentiation. Work with iPS and ES cells was conducted under the approval and auspices of the University of Washington Embryonic Stem Cell Research Oversight Committee. Specific cell lines used in this study are described below and are sourced from commercially available iPS and ES cell lines obtained with informed consent. Stem cell stocks were maintained in mTeSR1 media with daily media changes and passaging using Accutase (STEMCELL Technologies). 1,000-6,000 cells per well were placed in each 24-well plate pre-coated with 300 µL of DMEM-F12 containing 0.2 mg/mL Matrigel and sandwiched the following day with 0.2 mg/mL Matrigel in mTeSR1 (STEMCELL Technologies) to produce scattered, isolated spheroid colonies. 48 hrs after sandwiching, spheroids were treated with 12µM CHIR99021 (Tocris Bioscience) for 36h, then changed to RB (Advanced RPMI + 1X Glutamax + 1X B27 Supplement, all from Thermo Fisher Scientific) and replaced every 3 days thereafter. Organoids were differentiated for 21 days from the time of plating, at which time tubular structures had formed. Gene edited *PKD2*$^{-/-}$ organoids were picked from the adherent plate at day 21, placed in suspension culture with RB media replaced every 3 days until day 30 when cyst growth was prominent (91).

SARS-CoV-2 generation. All experiments using live virus were performed in the Biosafety Level 3 (BSL-3) facility at the University of Washington in compliance with the BSL-3 laboratory safety protocols (CDC BMBL 5th ed.) and the recent CDC guidelines for handling SARS-CoV-2. Before removing samples from BSL-3 containment, samples were inactivated by Trizol or 4% paraformaldehyde, and the absence of viable SARS-CoV-2 was confirmed for each sample by plaque assays. SARS-Related Coronavirus 2, Isolate USA-WA1/2020 (SARS-CoV-2) and icSARS-CoV-2mNG (SARS-CoV-2-mNG) were obtained from BEI Resources (NR-52281) and the University of Texas (87). Isolate 501Y.V2.HV001 (B.1.351) containing E484K/N501Y/D614G mutations along with furin cleavage site point mutation was obtained from Alex Sigal, AHRI (African Health Research Institute) and amplified in Vero-hACE2-TMPRSS2 cells upon reception. Virus stocks generated were tittered on VeroE6-TMPRSS2 cells. SARS-CoV-2 isolates hCoV-19/England/204820464/2020 (NR-54000), hCoV-19/Japan/TY7-503/2021(NR-54982), hCoV-19/USA/CA-SU-15_S02/2021 (NR-55486), and hCoV-19/USA/PHC658/2021 (NR-55611) were obtained through BEI Resources, NIAID, NIH and propagated in Vero cells (USAMRIID). Briefly, Vero cells were maintained in DMEM (Gibco) supplemented with 10% heat-inactivated FBS, 100 U/mL penicillin, and 100 U/mL streptomycin at 37 °C in a 5% CO2 humidified incubator. To generate virus stock, cells were washed once with DPBS and infected with SARS-CoV-2 in serum-free DMEM. After 1 h of virus adsorption, the inoculum was replaced with DMEM supplemented with 2% heat-inactivated FBS, and cells were incubated at 37 °C in a 5% CO2 incubator until ~70% of cells manifested cytopathic effects. The virus was harvested by collecting the culture supernatant followed by centrifugation at 3,000 g for 15 min at 4 °C to remove the cell debris. Virus titer was then measured by plaque assay on Vero cells (as described below), and stocks were stored at -80°C.

SARS-CoV-2 tittering. Viral preparations and culture supernatant from SARS-CoV-2-infected kidney organoids were tittered using a plaque assay. Briefly, 350,000 Vero cells were seeded in 12-well plates and incubated for 1 h at 37 °C with 10-fold dilutions of virus-containing media. A 1:1 solution 1.8% cellulose suspension in water (Sigma) and 2X DMEM supplemented with 4% heat-inactivated FBS, L- glutamine, 1X antibiotic-antimycotic (Gibco), and 220 mg/mL sodium pyruvate was layered on top of the cells, followed by incubation at 37 °C for 2 days. After fixing with 10% formaldehyde, the cellulose layer was removed and cells were stained with 0.5% crystal violet solution in 20% ethanol. Plaques were counted, and the virus titer in the original sample was assessed as plaque- formation unit per mL (PFU/mL).

Fusion Forming Assay. Viral culture supernatants from Delta variant supernatants were counted using a fusion forming assay rather than plaque assay due to their small size. The protocol is the same as the tittering protocol up to the cellulose layer removal step. After cellulose layer removal, fixed cells were washed with FFA wash buffer: 1X PBS with 0.05% Triton X-100 (Sigma). SARS-CoV-2 Nucleocapsid (Sino Biological 40143-R019-100, 1:8000) was added in FFA staining buffer: 1X PBS with 1 mg/ml Saponin (Sigma), and incubated overnight at 4 °C. The following day, cells were washed 3X with FFA wash buffer, and then incubated with goat anti-rabbit IgG HRP antibody (Bio-Rad 1706515, 1:5000) in FFA staining buffer for two-three hours at 4 °C. Cells were washed 3X with FFA wash buffer. TrueBlue Substrate (SeraCare) was added to cells, incubated for 10 minutes or until blue spots are visible with minimal background. Cells were then washed with water to quench the reaction and blue spots were counted and calculated based upon the volume of supernatant added as fusion forming units per mL (FFU/mL).

Viral infection with and without therapeutic treatments. SARS-CoV-2 was diluted to the desired multiplicity of infection (MOI) in serum-free DMEM and incubated on kidney organoids for 1 h at 37 °C (non-infected MOCK controls were incubated with DMEM only). Organoids were then washed with DPBS and cultured in RB media. Remdesivir (Selleck Chemicals) treatment involved adding 2 μM remdesivir to RB media post 1 h viral incubation. LCB1 spike binder was mixed in a 1:1 ratio with diluted virus and incubated for 1 h at 37 °C prior to adding to organoids.

Gene expression analysis and viral RNA detection. Infected organoids were washed once with DPBS and incubated with 500 μl per well of Trizol reagent (Invitrogen) for 30 min at room temperature. RNA was purified using the Direct-zol RNA Miniprep (Zymo Research). cDNA was synthesized using SuperScript IV Reverse Transcriptase per the manufacturer's instructions (ThermoFisher Scientific). Quantitative real-time reverse transcription (qRT-PCR) was performed with PowerUp SYBR Green Master Mix and the following forward and reverse primers: SARS-CoV-2-E, F: GAACCGACGACGACTACTAGC, R: ATTGCAGCAGTACGCACACA, ACE2, F: CCATCAGGATGTCCCGGAG, R: TGGAGGCATAAGGATTTTCTCCA, TMPRSS2, F: TCGAAGAACAATATCTGGTGGCT, R: GATTAGCCGTCTGCCCTCATTT, ISG15, F: GAGAGGCAGCGAACTCATCT, R: CTTCAGCTCTGACACCGACA, NXT1, F: GTTGTCATCTGTGGATCAGTGAA, R: CTACAGAGCTAGGGCTGAATGAA, USO1, F: GAAAGAACAGTTGCTCAGGGTTC, R: TGTTTGTATTTTGCTTCCCCGTC, GALNT1, F: GGCTTGCATTTCTTTTCCTAAAT, R: TTGCCAACAGACTGCTCTACATA, PPP2R3A, F: CAGGAGGATTTCATCCCTCTACT, R: TCGAAGTAATTTTTCCACTCCAA, IDH3G, F: CACAAGGCCAACATCATGAAACT, R: TCCACAATCATGTTCTCGAAGGT, RAB18, F:

GAACTTGCAGCAACAATAGGTGT, R: AACACCCTGTGCACCTCTATAAT, GCSH, F: GGAAAGTGTGAAAGCTGCTAGTG, R: TCTTGATCAGCCAACCATCTTCA, beta-actin, F: GCGAGAAGATGACCCAGATCAT, R: GGATCTTCATGAGGTAGTCAGTC.

Immunostaining. Immunostaining followed by confocal microscopy was used to localize various proteins and transporters in the cysts and organoids. Prior to staining, organoids were fixed in 4% PFA for 30 mins at room temperature. After fixing, samples were washed in PBS, blocked in 5% donkey serum (Millipore)/0.3% Triton-X-100/PBS, incubated overnight in 1% bovine serum albumin/0.3% Triton-X-100/10μM $CaCl_2$/PBS with primary antibodies, washed, incubated with Alexa-Fluor secondary antibodies (Invitrogen), washed and imaged. Primary antibodies or labels include Biotinylated LTL (Vector Labs B-1325, 1:500), E-Cadherin (Abcam ab11512, 1:500), hPODXL (R&D Systems AF1658, 1:500), ACE2 (Antibody 1: R&D Systems AF933, 1:40, Antibody 2: Novus, #sn0754, 1:100), Cleaved caspase-3 (Cell Signaling Technology, 9661S, 1:100), Claudin-1 (Abcam 15098, 1:300), and SARS-CoV-2 Nucleocapsid (Sino Biological 40143-R019-100, 1:50). Live and dead staining used Calcein AM (Invitrogen) and Propidium Iodide (Thermo Fisher) per manufacturer's instructions. Fluorescence images were captured using a Nikon A1R inverted confocal microscope with objectives ranging from 10X to 60X. Note: we were unable to co-localize the infected with distal tubules (E-cadherin^{+}), due to overlap in spectra between the secondary antibody and SARS-CoV-2-mNG.

Immunohistochemistry. Kidneys from a male 8-week-old C57BL/6J mouse were collected, paraffin embedded, sectioned, deparaffinized, quenched with 3 volumes of hydrogen peroxide in

methanol, heat induced epitope retrieval in 1 mM EDTA, and blocked for 1 hour in 1.5% normal goat serum in PBS. Sections were then stained with ACE2 primary antibody (Novus, #sn0754, 1:100), washed, and stained with secondary antibody (Goat anti-rabbit biotin, ab64256) prior to imaging using an Olympus BX41 microscope at 40X.

Patient Cohort and Clinical Data Collection. The **C**OVID-19 **H**ost **R**esponse and Clinical **O**utco**me**s (CHROME) study began enrolling critically ill hospitalized patients suspected of SARS-CoV-2 infection in April 2020. This analysis included the first 120 patients enrolled in CHROME with an indwelling bladder catheter for collection of urine. Details of study enrollment have been previously published (92). In brief, subjects were eligible if they were admitted to an ICU for COVID-19 as defined by having symptoms suggestive of SARS-CoV-2 infection (fever, respiratory symptoms including cough/shortness of breath, or sore throat) and one of the following: 1) any respiratory support with supplemental oxygen or an oxygen saturation of < 94% on ambient air; or 2) any chest radiographic abnormality. A case of COVID-19 was defined by a positive reverse-transcriptase–polymerase-chain-reaction (RT-PCR) for SARS-CoV-2 from a nasopharyngeal swab. The University of Washington IRB approved all studies (STUDY9763).

Sample collection, proteomic platform and quality control. Urine was collected within 24 hours of ICU admission. Peripheral blood was collected into EDTA anti-coagulant tubes within 24 h of ICU admission. Plasma was isolated by centrifugation (10 min, 3000 rpm, room temperature). All samples underwent one freeze-thaw cycle prior to analysis. Proteomic profiling in urine was completed using the SomaScan® Platform that contains 5,284 SOMAmer single-stranded DNA aptamers that bind to protein analytes with high specificity. The assays were performed as

previously described (93–95). For each sample, the platform reported a relative fluorescent unit (RFU) for each aptamer-protein pair that provides a scale-free measure of protein abundance. The SomaScan Assay is run using 96-well plates, including hybridization normalization control sequences to control for variability in the Agilent readout process. For readout, SOMAmer reagents are hybridized to complementary sequences on a DNA microarray chip and quantified by fluorescence. Fluorescence intensity in the SomaScan assay for each reagent is related to the relative availability of the three-dimensional shape-charge epitope on each protein (the binding site of the SOMAmer reagent) in the original sample. This reflects each protein's abundance (concentration), the shape of the protein and circulating competitors (physiologic or a therapeutic antibody). Plate calibration is performed by calculating the ratio of the Calibrator Reference RFU value to the plate-specific Calibrator replicate median RFU value for each SOMAmer. The resulting ratio distribution is decomposed into a Plate Scale factor defined by the median of the distribution and a vector of SOMAmer-specific Calibration Scale Factors. Median intra- and interassay coefficients of variation are approximately 5% (96).

LCB1 Protein expression. LCB1 design was made as described previously (69). For expression and purification, briefly, modified pET-29b(+) E. coli plasmid encoding LCB1 was used to transform into chemically competent E. coli Lemo21 cells (NEB). Successfully transformed E. coli were selected using Studier autoinduction media supplemented with antibiotics. The cells were harvested by spinning at 4,000xg for 10 min and then resuspended in a lysis buffer with DNAse and protease inhibitors. The cell lysate was sonicated for 4 minutes total (2 minutes on time, 10 sec on-10 sec off) with an amplitude of 80%. Soluble fraction was clarified by centrifugation at 20,000g for 30 min and purified by IMAC (Qiagen) followed by size exclusion chromatography

(Superdex 75 10/300 GL, GE Healthcare). All protein samples were analyzed with SDS-PAGE with the purity higher than 95%. LCB1 spike binders were validated to neutralize SARS-CoV-2 in Vero cells prior to use in organoids (data not shown).

Semi-automated image analysis to quantify SARS-CoV-2-mNG percent infection.

A custom FIJI macro (Sup. file 1) was developed to quantify percent area infected by SARS-CoV-2-mNG within the entire organoid body as well as within PODXL and LTL positive regions. This workflow was designed to provide an unbiased approach to quantifying infection, whereas nuclei-based segmentation of individual cells proved too noisy for accurate quantification due to the three-dimensional nature of the structures. A representative image analysis workflow is presented in (S2A-D). For simplicity, quantification was performed on maximum-intensity projections of confocal Z-stacks taken through the full thickness of the organoid body. Organoids were manually outlined, and the outside signal was cleared to restrict analysis to the organoid body. For each replicate, thresholding parameters were empirically chosen to accurately define PODXL- and LTL-positive regions and applied uniformly to all mock and infected organoid images within a paired set. Binary thresholded images were used to define areas exclusively positive for either PODXL or LTL. Histograms of pixel intensity were generated for each organoid within its entire outline and sub-regions. Histograms were normalized to convert raw pixel counts to percent of area, such that each organoid contributes equally to statistical analysis. To define a threshold for pixel intensity considered infected, normalized pixel intensity histograms of the entire organoid outline for all mock organoids within a particular set were pooled together and the average and standard deviation (sd) for the pooled data was quantified. Pixels that were greater than 3 standard deviations above average pixel intensity for the pooled mock data were defined as infected. Of

note, by this criterion for a perfect normal distribution, mock organoids would be expected to have 0.15% of pixels defined as infected. The pixel intensity threshold determined from the entire organoid outline was then uniformly applied to both the PODXL- and LTL- exclusive regions for all organoid images within a set to determine the percent infection of each region for all organoids.

SARS-CoV-2-lentiviral transduction. Kidney organoids and Vero cells were incubated with MOI 10 SARS-CoV-2-lentiviral (Amsbio) particles in Opti-MEM reduced serum media (Thermo Fisher Scientific), incubated for one hour, washed with 1X PBS, and incubated for 48 hours in RB media prior to 4% paraformaldehyde fixation.

Organoid Cell Type Expression Analysis. An RDS file of publicly available D18-21 hESC-kidney organoid single cell RNA-seq data (GEO GSE115986) using previously described clusters was generated using RStudio and Seurat V3 and used to generate a cellxgene (single cell visualization platform, Chan-Zuckerberg initiative) instance (88). Dot blots representing cell cluster-specific gene expression were generated using the Visualization in Plugin function.

Statistical Analysis. *Organoid data.* Quantification was performed on data obtained from experiments performed on controls and treatment conditions side by side on at least three different occasions or cell lines (biological replicates). Error bars are mean ± standard error (SEM). Statistical analyses were performed using GraphPad Prism Software. Statistical analyses were only performed for experiments with more than two replicates. Statistics are plotted on the respective figures and the tests used are described in the figure legends.

Clinical Data. Admission acute kidney injury was defined by comparing the change (delta) and fold change in concentration from the admission serum creatinine to the lowest serum creatinine measured in the following 28 days of hospitalization. If the drop in serum creatinine is >0.3 mg/dL or >1.5 fold change the individual was defined as having admission acute kidney injury.

Protein Data normalization. The RFU for each aptamer-protein measurement in each sample was scaled by dividing it by the mean of the aptamer-protein RFUs reported in that sample to correct for background variation in RFU. The $\log_2$ transformation of mean normalized RFU values was used in regression.

Protein Fold change. We quantified the differences in protein abundance by fold change calculated as the ratio of normalized RFU values between comparison groups which was then $\log_2$-transformed.

Protein Regression models. We performed linear and logistic regression to identify differentially abundant log2 protein outcomes between COVID-positive and COVID-negative patients using the R glm() function. Significant associations were determined after Bonferroni correction (0.05 / 4984 = $1x10^{-5}$) as well as the false discovery rate (FDR< 0.1 for logistic and <0.05 for linear) threshold using the Benjamini-Hochberg method. All models were adjusted for age, sex and BMI. Adjusted log2 protein fold changes are the COVID-19+/- beta from the regression model.

Pathway Analysis. The Gene Ontology pathway database is available at the Bader Lab website (http://download.baderlab.org/EM_Genesets/December_11_2020/Human/entrezgene/Human_G

OBP_AllPathways_no_GO_iea_December_11_2020_entrezgene.gmt) (98, 99). Genes IDs matching 4141 Somalogic protein gene names were identified using the EntrezGene ID in the seq_gene.md (hg19, GRCh37.3) and the lists of protein-aptamers corresponding to each pathway were constructed. Pathways with less than three or more than 500 of the identified protein-aptamer gene names were excluded from analysis, making for 6410 pathways to be analyzed. The Generalized Berk-Jones test (GBJ) was used with the mean normalized RFU values of each set of protein-aptamers corresponding to a Gene Ontology pathway. The GBJ has been shown to be an optimal pathway-based test statistic for aggregated sets of genes, DNA variants and expression values (100–102). A null model adjusting for sex, age and BMI was used in each pathway test.

Statistical analyses relating to the analysis of the clinical and proteomic data were conducted in R version 3.6.3.

Study Approval. Animal work was performed in compliance with the strict ethical requirements and regulations of the University of Washington IACUC under a pre-approved animal protocol. Human samples were collected as part of the CHROME cohort (University of Washington Institutional Review Board #9763 and #6878). No individual personal data is included in the study. The IRB provided waiver of consent to participate in this study.

Graphical Schematics. All graphical schematics were originally created with BioRender.com, aside from Figure 7, which was adapted from “Remdesivir: Potential Repurposed Drug Candidate for COVID-19”, by BioRender.com (2021). Retrieved from https://app.biorender.com/biorender-templates.

2.3 RESULTS

2.3.1 *SARS-CoV-2 infects organoid proximal tubules with pathogenic effects*

To assess the susceptibility of kidney organoid cell types to SARS-CoV-2 infection, we utilized an adherent differentiation protocol that produces nephron-like epithelial structures surrounded by a monolayer of stromal and endothelial cell types (28, 88). We exposed these human kidney organoid cultures to a MOI of 10 of SARS-CoV-2/WA1 (SARS-CoV-2) and measured infection 72 hours later (Fig. 2.1 A). Using SARS-CoV-2 genetically engineered to express mNeonGreen (SARS-CoV-2-mNG), we observed that the fluorescent signal localized in epithelial kidney organoid structures, whereas the surrounding monolayer of stromal and endothelial cells was not infected (Fig. 2.1 B) (87). Viral RNA of SARS-CoV-2 was readily detected in infected cultures, indicating that virus had entered cells (Fig. 2.1 C). 72 hours post-infection, supernatants from organoids exposed to SARS-CoV-2 or SARS-CoV-2-mNG efficiently infected Vero cells and produced viral plaques, demonstrating functional virion production in kidney organoids (Fig. 2.1 D and Fig. 2.2 A). Immunofluorescence analysis of nephron markers in organoids exposed to SARS-CoV-2-mNG revealed specific infection of *Lotus tetragonolobus* lectin positive (LTL^+) proximal tubules (Fig. 2.1 E). The strong binding of LTL to infected cells suggested that these were likely to be proximal rather than distal tubules (33). Podocytes were not generally infected, but individual podocytes ($PODXL^+$) infected with SARS-CoV-2-mNG were occasionally observed by confocal microscopy (Fig. 2.2 B). Similarly, cells resembling the parietal epithelial cells of Bowman's capsule ($CLDN1^+$) were not generally infected (Fig. 2.2 C) (33, 89). Using semi-automated image analysis quantification, we found that 12.4% of the total organoid area and

24.5% of the total LTL^{+} area was infected, respectively, whereas infection of podocytes (PODXL^{+}) was not significant (Fig. 2.1F and Fig 2.3 A-D).

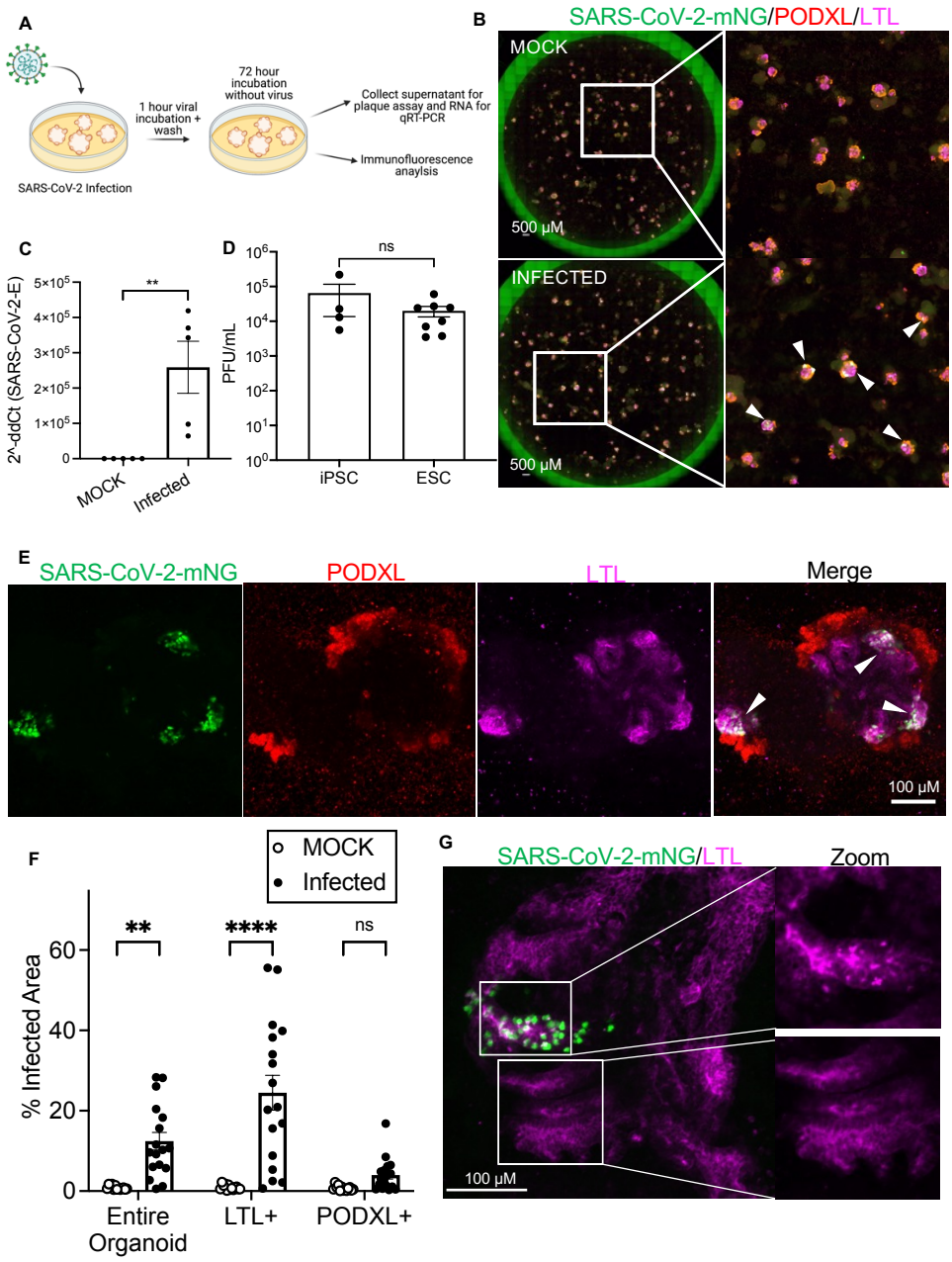

Figure 2.1 SARS-CoV-2 efficiently infects human kidney organoids with tropism for proximal tubules.

A. Schematic of kidney organoid infection protocol. B. Whole well wide-field immunofluorescence images of iPS cell-derived organoids infected with SARS-CoV2-mNG. Arrows point to infected cells. C. qRT-PCR of SARS-CoV-2 envelope RNA in organoids

infected with SARS-CoV-2 WA1 or mock-infected (MOCK). Dots represent a well of organoids. Mean ± SEM, n ≥ 1 well of organoids per infection from four independent experiments. Mann-Whitney test, **p< 0.01. D. Plaque assays of SARS-CoV-2 infected human kidney organoids derived from iPS cells or ES cells. Dots represent a well of organoids. Mean ± SEM, n ≥ 1 well of organoids per infection from three independent experiments respectively. Mann-Whitney test, ns p>0.05. E. Representative confocal immunofluorescence images of organoids infected with SARS-CoV2-mNG. F. Quantification of infected organoid cellular tropism. Dots represent a single organoid. Mean ± SEM, n ≥ 4 organoids per infection from three independent experiments. 2-way ANOVA, multiple comparisons MOCK vs infected for each respective region. **p<0.01, ****p<0.0001, ns p>0.05. G. Representative confocal immunofluorescence images of organoid infected with SARS-CoV2-GFP, with zoomed images of white boxed areas showing infected (top) versus uninfected (bottom) proximal tubules. Arrowheads indicate areas of disrupted LTL pattern.

We found that the use of SARS-CoV-2-mNG was vital for establishing the tropism of infection in kidney organoids. In contrast to SARS-CoV-2-mNG, a commercially available GFP-expressing lentivirus pseudotyped for SARS-CoV-2 failed to productively infect kidney organoids or Vero cells (Fig. 2.4 A). This likely reflects inferior levels of infection by SARS-pseudotyped lentiviruses, compared to native virus (103). In addition, a commercially available antibody raised against SARS-CoV-2 nucleocapsid did not produce specific staining in organoids infected with SARS-CoV-2, but rather showed high background staining levels in stromal cells, necessitating our use of SARS-CoV-2-mNG to evaluate viral tropism (Figure 2.4 B).

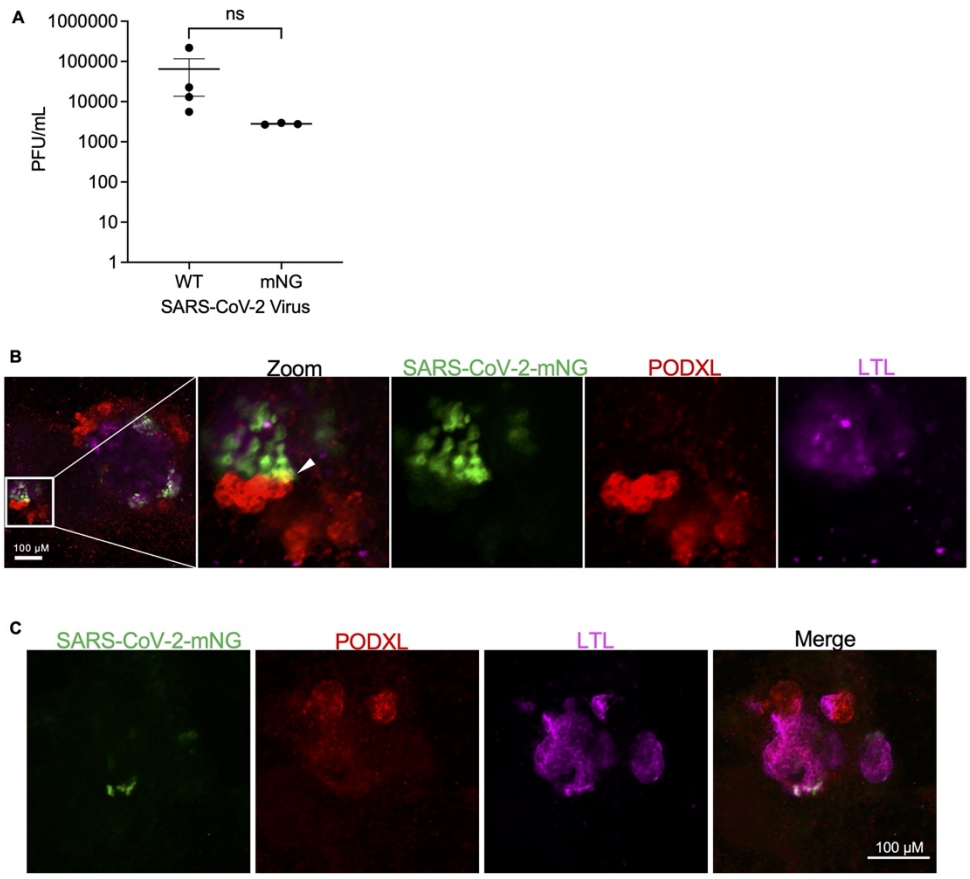

Figure 2.2. SARS-CoV-2 has minimal podocyte infection.

A. Plaque assays of SARS-CoV-2 and SARS-CoV-2-mNG infected WTC11 kidney organoids. Dots represent a well of organoids. Mean ± SEM, n ≥ 1 well of organoids per infection from three independent experiments. Mann-Whitney test, ns $p > 0.05$. B. Immunofluorescent images of a SARS-CoV-2 infected organoid. C. Immunofluorescent images of a SARS-CoV-2 infected organoid.

Close inspection of infected versus non-infected proximal tubules revealed swollen, rounded cells with a disruption of the smooth LTL patterning at the apical plasma membrane showing increased compartmentalization into bright foci (Fig. 2.1 G). Immunofluorescence analysis of cleaved caspase-3 was inconclusive because it showed high staining of the background and was difficult to discern in the densely packed, three-dimensional organoids themselves (Fig. 2.4 C). Lactate

dehydrogenase (LDH) release was not detectably increased in infected organoid supernatants, consistent with the observation that SARS-CoV-2 treatment was not overtly toxic to these cultures as a whole (Fig. 2.4 D). These findings reveal specific proximal tubular tropism of SARS-CoV-2 capable of producing replicating virus and disrupting tubular morphology.

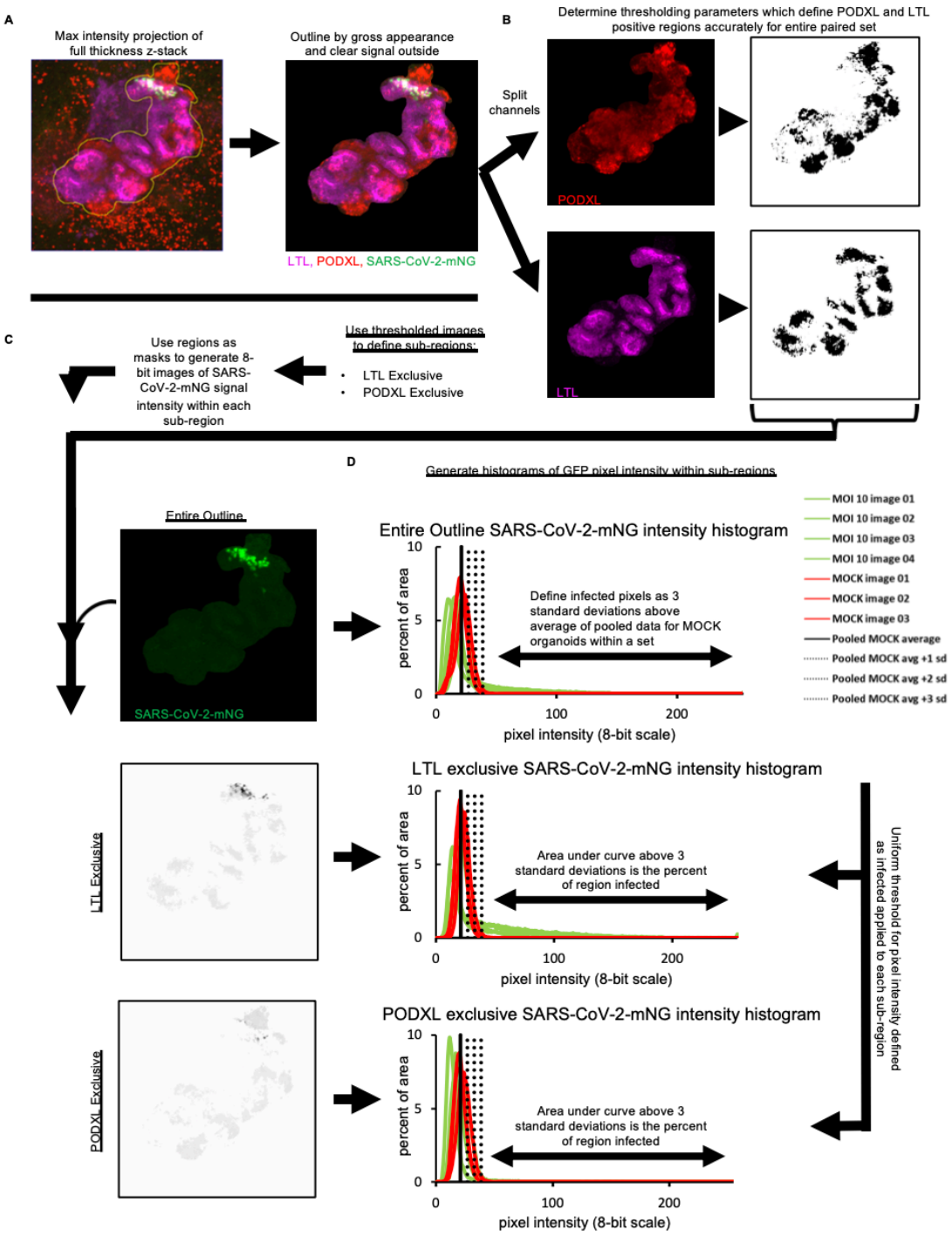

Figure 2.3 Semi-automated image analysis workflow.

Representative image analysis workflow for a SARS-CoV-2-mNG infected WTC11 organoid. A. Confocal Z-stacks converted to maximum intensity projections; organoid is then manually outlined with outside signal cleared to restrict analysis to signal within the organoid

body. B. Representative multi-channel composite images are split into individual channels for podocalyxin and LTL. User determines threshold parameters for each channel which accurately define podocalyxin- and LTL-positive regions. Uniform thresholding parameters for each channel are applied to all mock and infected organoid images within a paired set. C. Binary thresholded images are used to define areas that are exclusively positive for either podocalyxin or LTL. Regions with vertically adjacent distinct cell types artifactually appear co-stained in projection and are excluded from analysis. Podocalyxin- and LTL- exclusive binary images are used as masks to generate images of SARS-CoV-2-mNG pixel intensity within each defined sub-region. D. Histograms of pixel intensity are generated for each organoid within a Mock (not shown) and infected paired set. Histograms normalized based on size of organoid or region to convert raw pixel counts to percent of area, such that each organoid contributes equally to statistical analysis. Normalized histograms of pixel intensity of the organoid outline for all Mock organoids within a particular set are pooled and the average and standard deviation for the pooled data is quantified. Pixels greater than 3 standard deviations above average pixel intensity for the pooled Mock data are defined as infected. By definition for a perfect normal distribution, Mock organoids are expected to have 0.15 % of pixels defined as infected on average. The pixel intensity threshold for infection determined from the organoid outline is uniformly applied to both the podocalyxin- and LTL- exclusive regions for Mock and infected organoid images within a set to determine the percent infection of each area for all organoids.

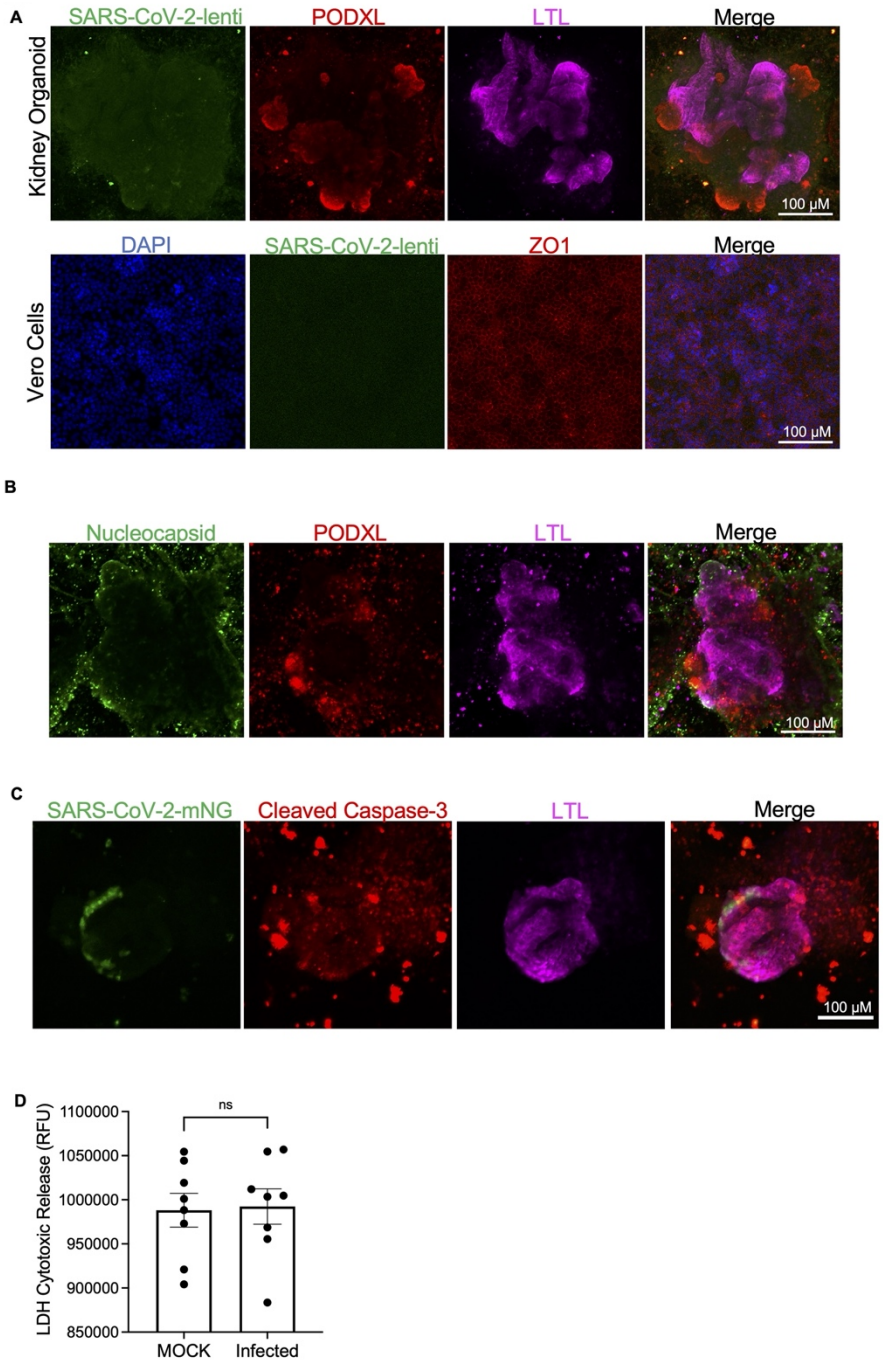

Figure 2.4 SARS-CoV-2 kidney organoid assay development.

A. Top panel: Kidney organoids infected with SARS-CoV-2 pseudotyped lentivirus. Bottom panel: Vero cells infected with SARS-CoV-2 pseudotyped lentivirus. B. Immunofluorescence images of SARS-CoV-2 infected organoids. C. Immunofluorescence images of SARS-CoV-2 infected organoids. D. LDH detection assay of infected kidney organoid supernatants 72 hours

post SARS-CoV-2 infection. Dots represent a technical replicate. Mean ± SEM, n = 4 technical replicates per condition from two independent experiments. Unpaired t-test, ns $p > 0.05$.

2.3.2 *SARS-CoV-2 infects PKD cystic epithelium causing cytotoxicity*

Polycystic kidney disease (PKD) is the most common genetic cause of chronic kidney disease and a possible risk factor for developing severe COVID-19, but these patients are rare which has impeded large cohort studies (104). In polycystic kidney disease, expansive cysts form from tubular epithelial cells, but whether PKD cysts are susceptible to SARS-CoV-2 infection is unknown. We assessed this with *PKD2*$^{-/-}$ organoids in suspension culture, which form cysts from proximal and distal tubules (91) (Fig. 2.5 A). Cystic organoids were infected with SARS-CoV-2 and SARS-CoV-2-mNG and assessed for viral infection and replication via plaque assay and immunofluorescence staining (Fig. 2.5 B and 2.6 A). A subpopulation of cyst-lining epithelial cells with LTL binding affinity (suggesting a proximal tubular origin) was infected selectively by SARS-CoV-2-mNG and caused cell swelling (Figures 2.5 B and 2.6 B). The percentage of infected area per cystic organoid was comparable to that of non-cystic organoids (Figure 2.5 C).

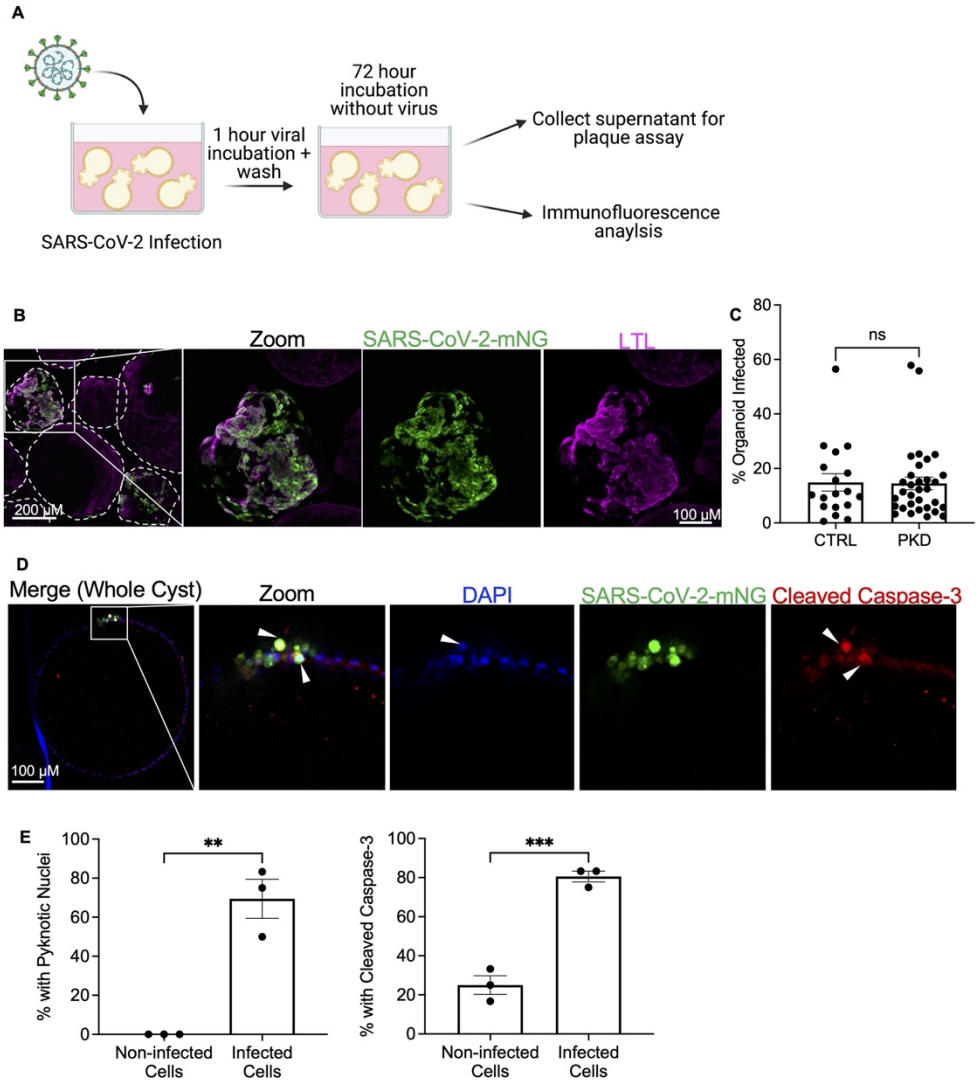

Figure 2.5. SARS-CoV-2 infects PKD organoid cystic epithelium.

A. Schematic of cystic PKD organoid infection protocol. B. Representative confocal immunofluorescence images showing cystic PKD organoids infected with SARS-CoV2-mNG. Outlines denote independent organoids. C. Quantification of infected organoid area (% total) of PKD and control (isogenic non-PKD) SARS-CoV-2-mNG infected cultures. Dots represent a single organoid. Mean ± SEM, n ≥ 4 organoids per infection from three independent experiments each. Unpaired t-test, ns $p>0.05$. D. Representative immunofluorescence images of cystic PKD organoids infected with SARS-CoV2-mNG, with zoom of cleaved caspase-3 staining and pyknotic nuclei. E. Quantification of pyknotic nuclei and elevated cleaved caspase-3 levels of infected and non-infected cells of infected organoids. Dots represent a biological replicate. Mean

± SEM, n ≥ 5 organoids per biological replicate from three independent experiments each. Unpaired t-test, **p<0.01, ***p<0.001.

Infection-induced apoptosis of cystic PKD epithelium was observed in infected organoids as indicated by significantly increased expression of cleaved caspase-3 and pyknotic nuclei in infected cells, compared to non-infected cells in the same organoid (Figure 2.5 D-E). These indicators of cytotoxicity were more readily discerned in the thinner layer of cyst-lining epithelial cells than in denser organoid tubular structures without a PKD phenotype (Figure 2.6 B). Together, these data indicate that PKD cysts derived from proximal tubules are susceptible to SARS-CoV-2 infection in organoids, and that infection induces apoptosis in cystic epithelium.

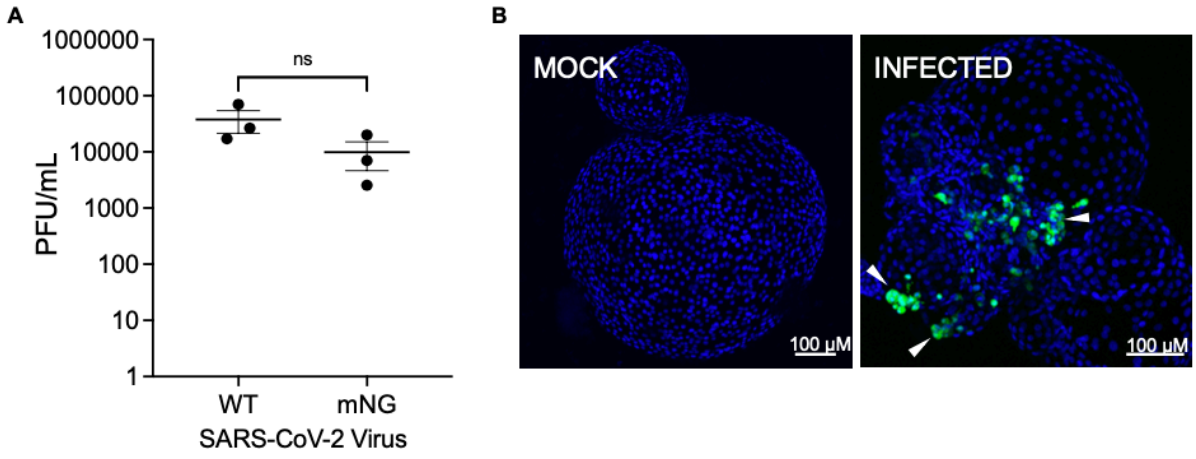

Figure 2.6 SARS-CoV-2 infection of PKD organoids.

A. Plaque assays of SARS-CoV2 WT and SARS-CoV-2-mNG infected PKD human kidney organoids. Dots represent a well of organoids. Mean ± SEM, n = 1 well of organoids per infection from three independent experiments. Mann-Whitney test, ns p > 0.05. B. Immunofluorescent SARS-CoV2-mNG infected cystic PKD organoids.

2.3.3 *COVID-19⁺ patient urine expresses signatures found in organoids*

To assess physiological relevance of the organoid model, we analyzed urinary proteins that characterize COVID-19 infection in prospectively enrolled critically ill patients with signs and symptoms suggestive of SARS-CoV-2 infection, who were placed under respiratory isolation by the treating physician (92) (Figure 2.7 A). Positivity for COVID-19 was subsequently confirmed by RT-PCR (COVID-19^{+}), while patients who tested negative provided a symptom-matched, critically ill control group (COVID-19^{-}). In patients with an indwelling catheter, we collected urine within 24 hours of intensive care unit admission from 61 COVID-19^{+} and 59 COVID-19^{-} patients. COVID-19^{+} and COVID-19^{-} patients were of similar mean age (56 ± 17 years and 54 ± 16 years, respectively), while COVID-19^{+} patients were more likely to be male (75% vs. 54%) and of Hispanic ethnicity (38% vs 7%) (Table 1). Despite COVID-19^{-} patients having higher rates of chronic kidney disease, coronary artery disease and congestive heart failure, rates of AKI at the time of study enrollment were similar (58% in COVID-19^{+} and 59% in COVID-19^{-}). However, by the time of hospital discharge, receipt of acute renal replacement therapy was two-fold higher in COVID-19^{+} compared to COVID-19^{-} patients (15% vs 7%).

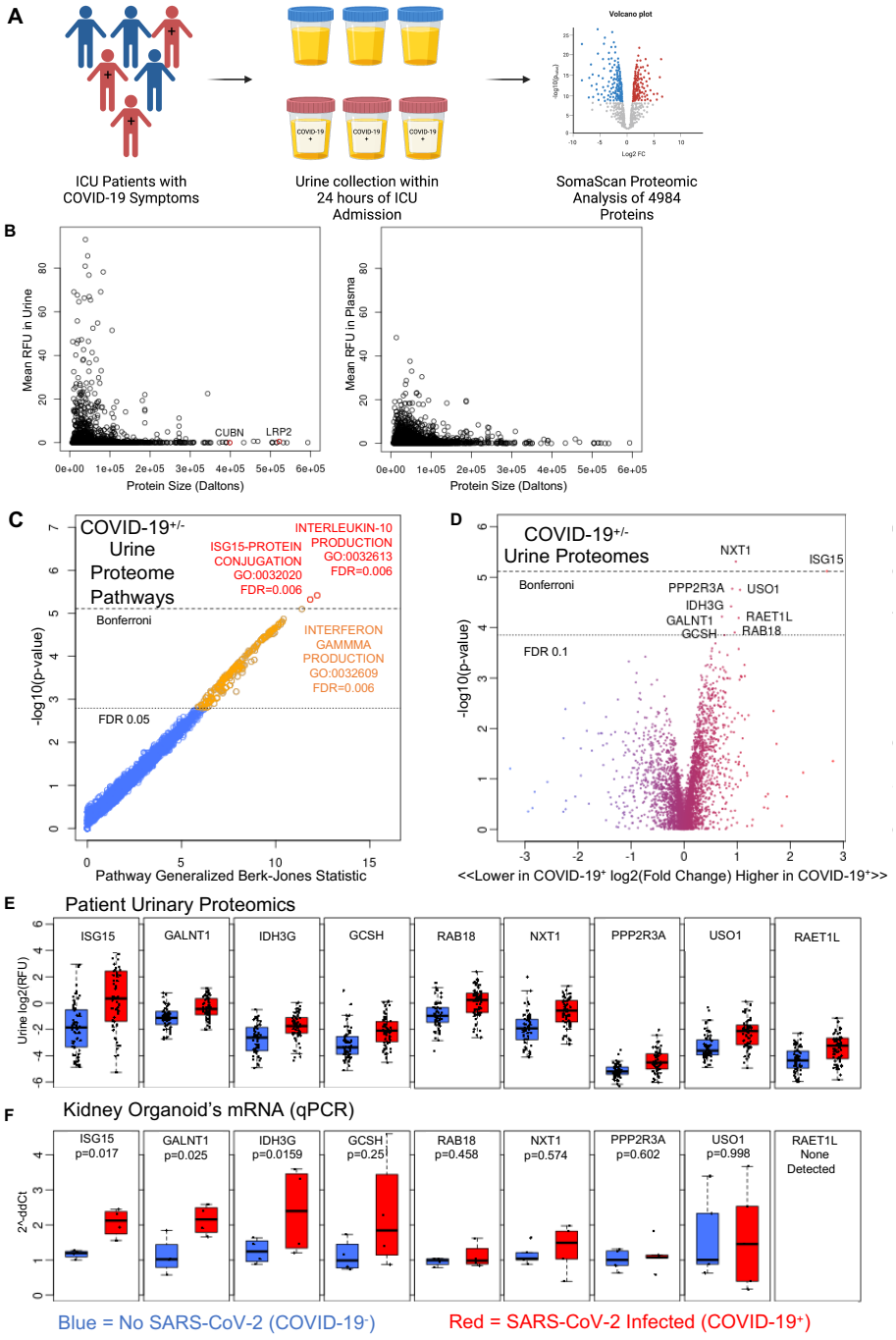

Figure 2.7. COVID-19^{+} patient urine expresses signatures found in organoids.

A. Schematic of patient cohort sample selection and analysis. B. Scatterplots of protein size vs relative abundance units (RFU) detected in patient urine and patient blood. C. Gene ontology pathway analysis of urine proteome reads. Red circles represent pathways that hit Bonferroni significance, orange circles represent pathways that hit an FDR <0.05, and blue are non-significant pathways. D. Volcano plot of increased and decreased proteins in COVID-19^{+} patient

urine compared to COVID-19$^-$ patient urine. Dotted lines represent FDR 0.1 and Bonferroni significance cutoffs. E. Upregulated proteomic hits between COVID-19$^+$ and COVID-19$^-$ patients. F. qRT-PCR of upregulated proteomic hits in organoids infected with SARS-CoV-2 WA1 or mock-infected (MOCK). Dots represent a well of organoids. Mean ± SEM, n ≥ 1 well of organoids per infection from four independent experiments. Unpaired t-test, *p< 0.05.

Urinary proteomes indicated a negative relationship between protein size and relative abundance (Spearman's rank correlation, rho = -0.05), whereas patient plasma exhibited no significant relationship of this kind, likely reflecting the size selectivity of the glomerular filtration barrier (Figure 2.7 B and Figure 2.8 A). Proteins too large to be efficiently filtered were nevertheless detected in these urine samples, including cubilin (CUBN) and megalin (LRP2), receptors that are strongly expressed in the brush border of kidney proximal tubular cells. Thus, urinary proteomes contained both filtered proteins originating from the plasma, as well as non-filtered proteins originating from the kidneys and urinary tract.

Table 1: Demographics and clinical outcomes of patient cohort

	COVID-19 Negative (N=59)	**COVID-19 Positive (N=61)**
Age, Mean (SD)	53.7 (16.3)	55.7 (17.1)
Male	32 (54.2%)	46 (75.4%)
Race		
White	34 (57.6%)	39 (63.9%)
Asian	5 (8.5%)	7 (11.5%)
Black	12 (20.3%)	5 (8.2%)
Native American	3 (5.1%)	4 (6.6%)
Unknown	5 (8.5%)	6 (9.8%)
Ethnicity		
Hispanic or Latino	4 (6.8%)	23 (37.7%)
NOT Hispanic or Latino	51 (86.4%)	35 (57.4%)
Unknown	4 (6.8%)	3 (4.9%)
Asthma	12 (20.3%)	6 (9.8%)
Diabetes	18 (30.5%)	20 (32.8%)
Chronic Kidney Disease	10 (16.9%)	6 (9.8%)
Coronary Artery Disease	13 (22.0%)	7 (11.7%)

Congestive Heart Failure	19 (32.2%)	10 (16.4%)
NIH Ordinal Scale on Admission		
Hospitalized	12 (20.3%)	11 (18.0%)
Hospitalized, requiring non-invasive positive pressure ventilation, high flow nasal cannula or non-rebreather	6 (10.2%)	4 (6.6%)
Hospitalized, requiring invasive mechanical ventilation or extracorporeal membrane oxygenation	41 (69.5%)	46 (75.4%)
AKI at the time of Study Enrollment	35 (59.3%)	35 (58.3%)
Inpatient Dialysis	4 (6.8%)	9 (14.8%)
In-hospital Mortality	20 (33.9%)	22 (36.1%)

We compared 4,984 urinary proteins between these patients with and without COVID-19. Using this urine proteomic data, we performed a Gene Ontology pathway analysis which identified 207 pathways as significantly differentially abundant with a false discovery rate (FDR) < 0.05. Two pathways, interleukin-10 (IL-10) production ($p = 3.83 \times 10^{-6}$, FDR = 0.006) and interferon-stimulated gene 15 (ISG15) protein conjugation ($p = 4.79 \times 10^{-6}$, FDR = 0.006), met the Bonferroni correction threshold of $p < 7.80 \times 10^{-6}$. The third most significant pathway was interferon gamma production ($p = 8.00 \times 10^{-6}$, FDR = 0.006) (Figure 2.7 C).

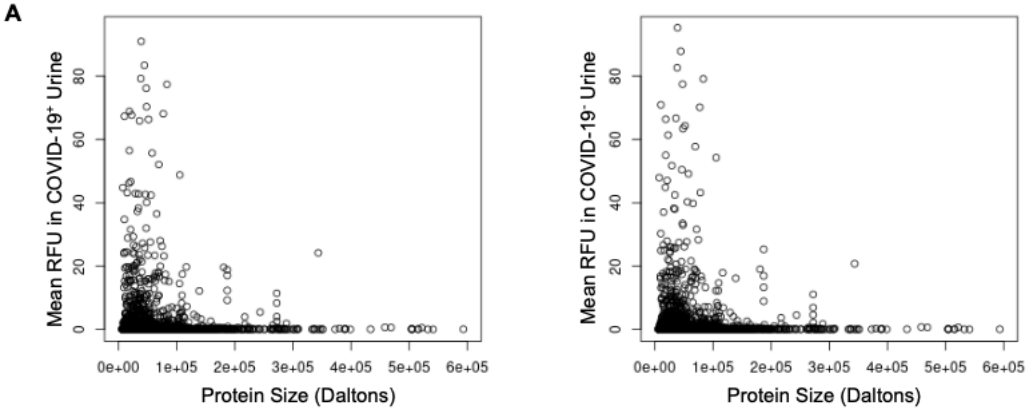

Figure 2.8. Scatterplots of protein size in patient urine.

A. Scatterplots of protein size vs relative abundance (RFU) of both COVID+ and COVID- patient urine.

Nine individual proteins were significantly higher in COVID-19^{+} patients adjusting for age, gender and body mass index with an FDR < 0.1 (Figure 2.7 D): ISG15, polypeptide N-acetylgalactosaminyltransferase 1 (GALNT1), isocitrate dehydrogenase (NAD(+)) 3 non-catalytic subunit gamma (IDH3G), glycine cleavage system protein H (GCSH), Ras-related protein 18 (RAB18), nuclear transport factor 2 like export factor 1 (NXT1), protein phosphatase 2 regulatory subunit B"Alpha (PPP2R3A), USO1 vesicle transport factor (USO1), and retinoic acid early transcript 1L (RAET1L) (Figure 2.7 E). No individual proteins were found to be downregulated in COVID patient urine at this FDR cutoff. A refined linear regression analysis of the proteomic hits (FDR < 0.05) further identified 23 upregulated proteins, of which the top nine are the same as described above and revealed 2 down-regulated proteins in COVID-19^{+} patient urine, hypoxanthine phosphoribosyltransferase 1 (HPRT1) and CD5 molecule-like (CD5L) (Figure 2.9 A).

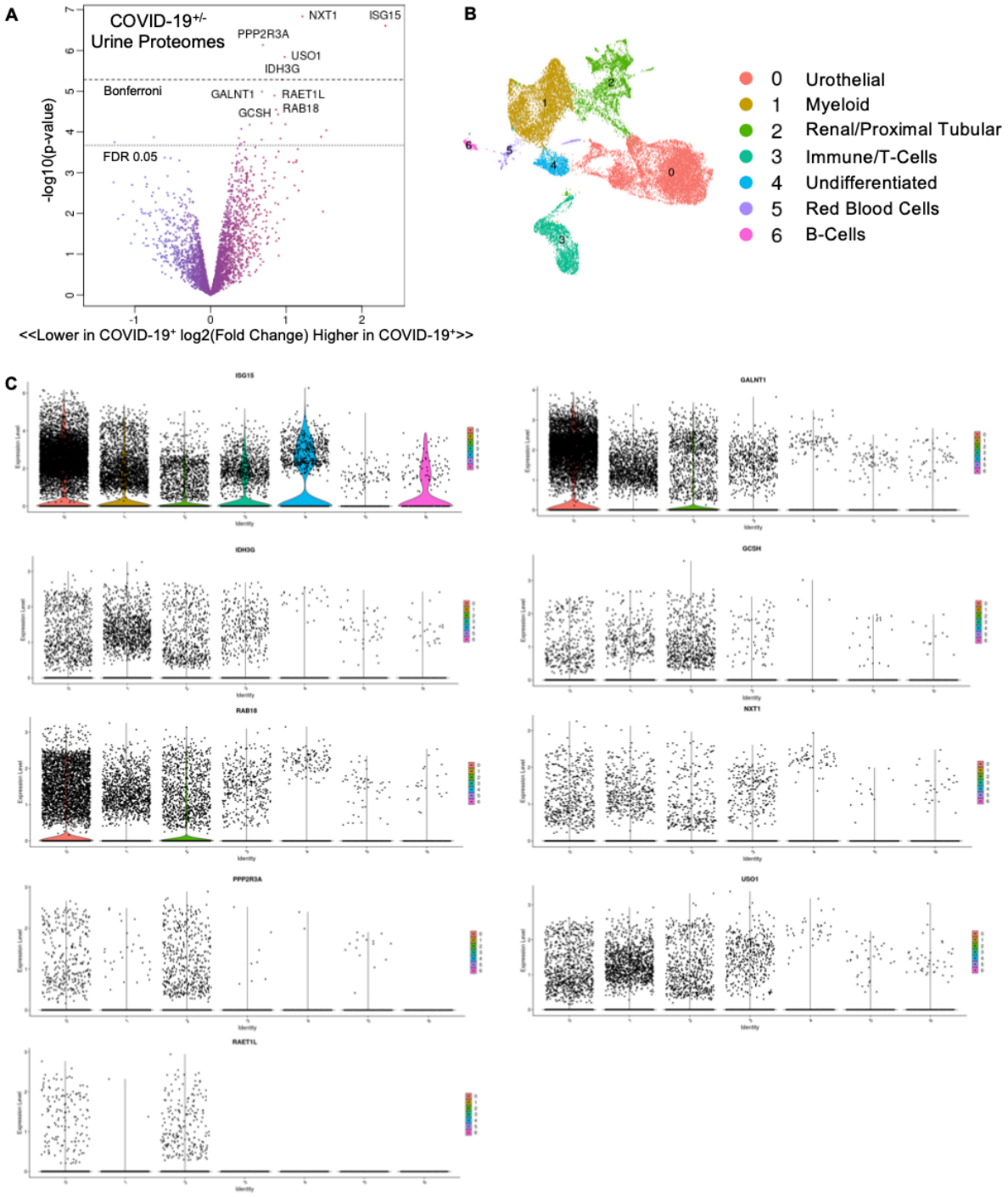

Figure 2.9. scRNAseq expression of upregulated proteins in patient urine.

A. Volcano plot from linear regression analysis of increased and decreased proteins in COVID-19^{+} patient urine compared to COVID-19^{-} patient urine. Dotted lines represent FDR 0.05 and Bonferroni significance cutoffs. B. Reference tSNE plot depicting scRNA-seq data

from 13 COVID+ patient urine samples (60). C. Violin plots of urinary cell clusters depicting relative expression of nine proteomic hits from COVID+ patient urine samples (60)

Transcripts of eight of these nine proteins were increased in kidney organoids infected with SARS-CoV-2 compared to their MOCK infected controls, including ISG15 and GALNT1 which were significantly upregulated (Figure 2.7 F). We assessed the cellular origins of the nine upregulated proteomic hits in a COVID-19^{+} urine single-cell RNA seq database, which revealed expression levels of all the hits in urothelial and proximal tubular cells, and a variety expressed in immune and myeloid cells (Figure 2.9 B-C) (60). Collectively, these expression signatures suggested that SARS-CoV-2 infection can induce an interferon response in kidney epithelial cell types similar in both patients and organoids (105–108).

2.3.4 *SARS-CoV-2 variants show similar rates of infection in kidney organoids*

SARS-CoV-2 is a positive-sense, single-stranded RNA virus that utilizes an RNA dependent RNA polymerase carrying a high mutation rate, up to one million times higher than its hosts' DNA polymerase (109). Higher mutation rates correlate with enhanced virulence of emerging viral strains and are suggested to produce SARS-CoV-2 viral variants with enhanced infectivity, such as the Delta variant (110–112). Formal studies directly comparing infection rates between variants of SARS-CoV-2 are required to draw this conclusion. Moreover, it is unknown if SARS-CoV-2 variants might exhibit differential tropism for the respiratory tract, which is the primary route of infection, versus extra-pulmonary organs, such as the kidney.

To assess whether SARS-CoV-2 variants exhibit altered viral fitness in kidney organoids, we infected kidney organoids with five viral variants: USA-WA1 (WA1), B.1.351-HV001 (Beta), B.1.1.7 (Alpha), P.1 (Gamma), B.1.617.1 (Kappa), and B.1.617.2 (Delta) (Table 2). Notably, the Delta variant we used for infections has a deletion in ORF7a that may influence virulence, although this strain is nevertheless associated with Delta outbreaks in human populations (113, 114). qRT-PCR analysis of RNA extracted from infected organoids demonstrated variable levels of detectable SARS-CoV-2 transcript, which were not significantly different among variants (Figure 2.10 A). Interestingly, supernatants from infected kidney organoids reveal significantly decreased levels of replicating virus from the Alpha, Gamma, Kappa, and Delta variants, compared to one of the originally isolated WA1 strains (Figure 2.10 B-C). Additionally, LDH release from infected kidney organoids was not significantly different between viral strains, nor heightened compared to mock infected controls (Figure 2.11 A).

Table 2: Viral variant descriptions

Origin	Lineage	GISAID Clade	WHO Label
USA-WA1	A	S	NA
United Kingdom	B.1.1.7	GR	Alpha
South African	B.1.351-HV001	GH	Beta
Brazil	P.1	GR	Gamma
India	B.1.617.1	G	Kappa
India	B.1.617.2	G	Delta

To assess whether rates of admission AKI, dialysis, or death change over time in our patient cohort, we plotted the prevalence at each patient's admission, of admission AKI, inpatient dialysis and in-hospital death over time using that patient and the next nine COVID-19^{+} patients admitted to the ICU (Figure 2.10 D). Death, dialysis, and AKI all had relatively low variance over time: AKI hovering around 40% prevalence, dialysis around 20%, and death around 50% between March,

2020 to February, 2021. While comprehensive variant sequencing data was unavailable in our COVID-19^{+} patient cohort, in Washington State, the WA1 variant was the predominant viral strain in March 2020, and the Alpha, Beta, and Gamma variants were detected in the US in January 2021 and Kappa and Delta detected March-May of 2021, while rates of AKI and dialysis remained steady in our patient cohort (115–118).

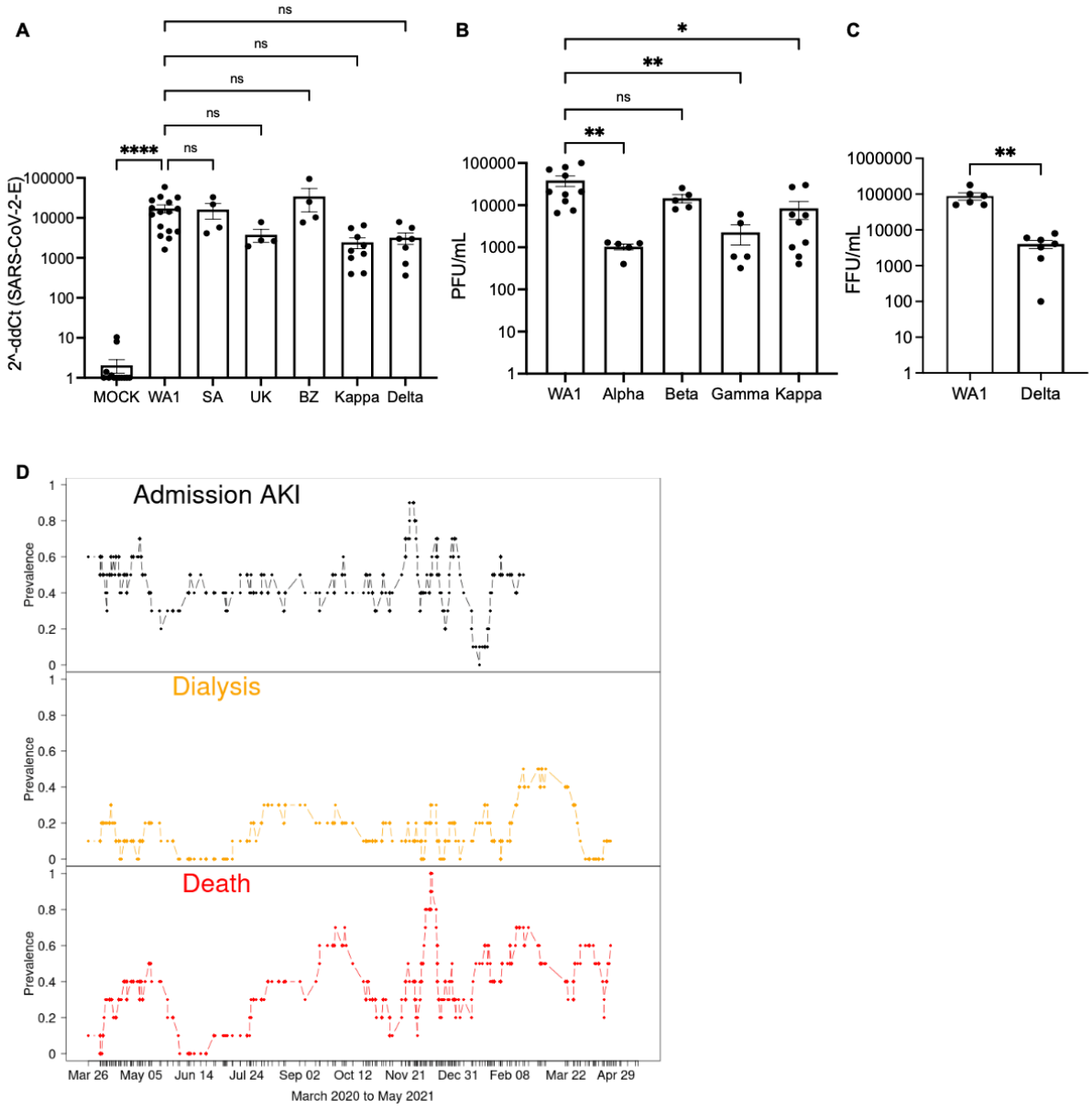

Figure 2.10. SARS-CoV-2 variants show similar rates of infection in kidney organoids.

A. qRT-PCR of SARS-CoV-2 envelope RNA in infected kidney organoid cultures. Dots represent a well of organoids. Mean ± SEM, n ≥ 1 well of organoids per infection from three independent experiments. One-way ANOVA, Kruskal-Wallis post-hoc test, **p< 0.01, ns p > 0.05. B. Plaque assays of SARS-CoV-2 infected kidney organoids. Dots represent a well of organoids. Mean ± SEM, n ≥ 1 well of organoids per infection from three independent experiments. One-way ANOVA, Kruskal-Wallis post-hoc test, *p< 0.05, ns p > 0.05. C. Focus forming assay of SARS-CoV-2 infected kidney organoids. Dots represent a well of organoids. Mean ± SEM, n ≥ 1 biological replicates per condition from three independent experiments. Mann-Whitney test, **p< 0.01. D. Prevalence of admission AKI, dialysis, and death in COVID+ patients over time.

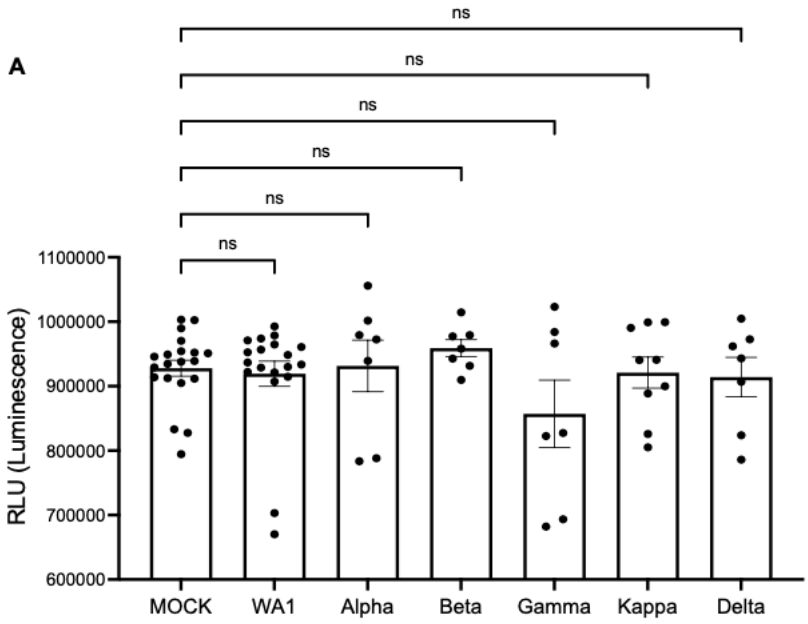

Figure 2.11. Cytotoxicity of SARS-CoV-2 viral variants.

LDH assay of kidney organoid supernatant. Dots represent technical replicate. Mean ± SEM, n = 1-3 technical replicates per condition from three independent experiments per variant. One-way ANOVA, Kruskal-Wallis post-hoc test, ns > 0.05.

2.3.5 *ACE2 is an essential viral entry pathway for SARS-CoV-2 infection*

Susceptibility of kidney organoids to SARS-CoV-2 infection is thought to depend upon expression of ACE2, but genetic proof of this is lacking. To assess this, we utilized genetically modified *ACE2*$^{-/-}$ stem cell lines, compared to *ACE2*$^{+/+}$ controls (Figure 2.12 A) (79). *ACE2*$^{-/-}$ kidney organoids differentiated normally (Figure 2.13 A). When exposed to SARS-CoV-2-mNG, however, *ACE2*$^{-/-}$ organoids did not express detectable mNG-fluorescence, in contrast *to ACE2*$^{+/+}$ controls (Figure 2.12 B-C). Supernatants from *ACE2*$^{-/-}$ organoid cultures showed 85% fewer viral particles than supernatants from *ACE2*$^{+/+}$ controls and were not significantly different in viral production from MOCK infected controls (Figure 2.12 D).

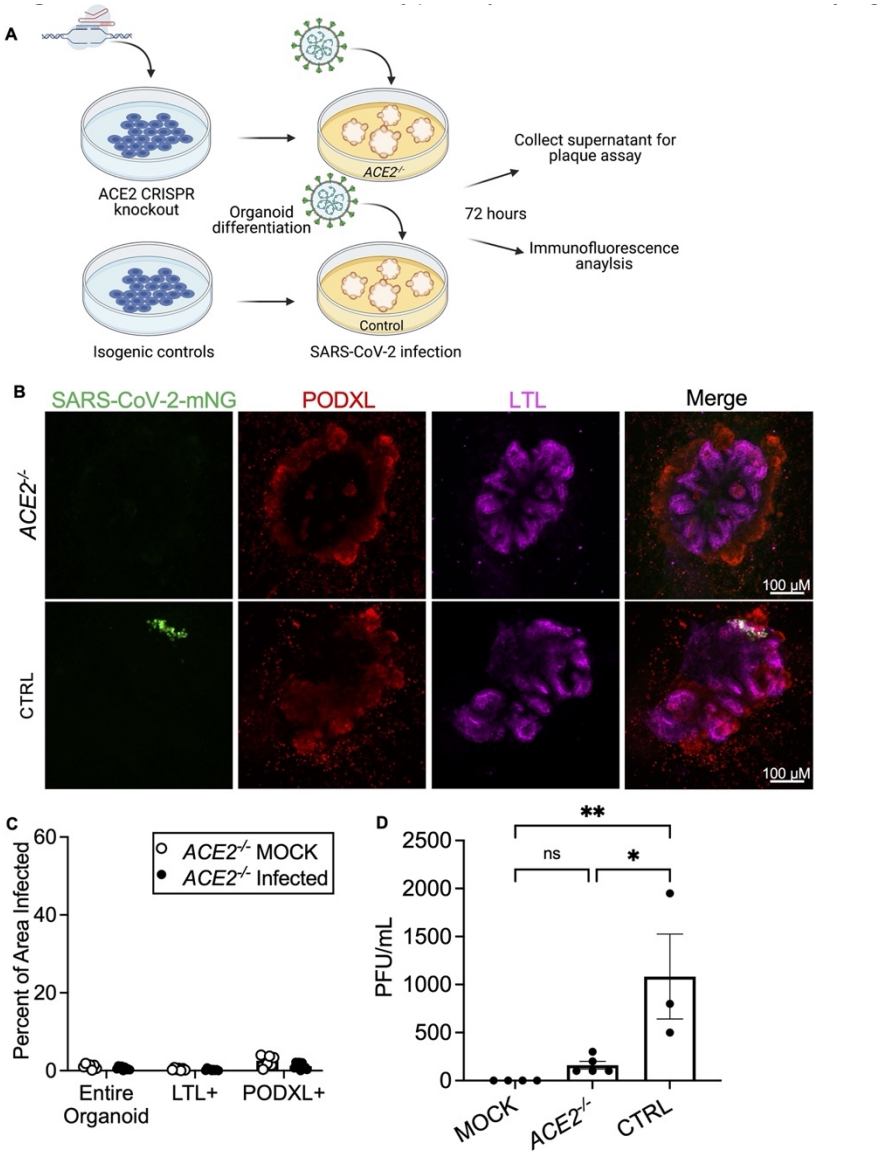

Figure 2.12. ACE2 is an essential viral entry pathway for SARS-CoV-2 infection of kidney organoids.

A. Schematic of ACE2 knockout and infection protocol. B. Representative confocal immunofluorescence images of *ACE2*$^{-/-}$ SARS-CoV2-mNG infected organoids, compared to isogenic controls. C. Quantification of GFP+ area in *ACE2*$^{-/-}$ organoids infected with SARS-CoV2-mNG, compared to mock-treated control. Dots represent a single organoid. N ≥ 4 organoids per experiment from two experiments. D. Plaque assay of *ACE2*$^{-/-}$ and control organoids infected with SARS-CoV-2 or mock-treated. Non-log scale is shown for this figure to emphasize low levels of infection in *ACE2*$^{-/-}$ organoids. Dots represent a well of organoids. Mean

± SEM, n ≥ 1 well of organoids per infection from three independent experiments, utilizing two distinct mutant cell lines. One-way ANOVA with Tukey's post-hoc tests. *$p < 0.05$, **$p < 0.01$, ns $p > 0.05$.

A commercially available antibody raised against ACE2 (Antibody 1, aa18-740) exhibited high levels of background in healthy or infected kidney organoids due to the density of these cultures but achieved lower background and higher specificity in cystic PKD organoids which possess a single layer of epithelial cells (Figure 2.13 B-C). Antibody 1 appeared more specific in organoids than another commercially available antibody (Antibody 2, aa190-230) (Figure 2.13 D). The relatively poor performance of these antibodies in kidney organoids was not due to general non-specificity, as Antibody 1 localized specifically to proximal tubular cells in cryosections of human developing kidney tissue, and Antibody 2 localized to the proximal tubules of an adult mouse (Figure 2.14 A-B). Therefore, we hypothesized that ACE2 was expressed in organoids but could not be readily detected due to the absence of well-differentiated brush border in these structures, which we have shown previously (28, 33, 54).

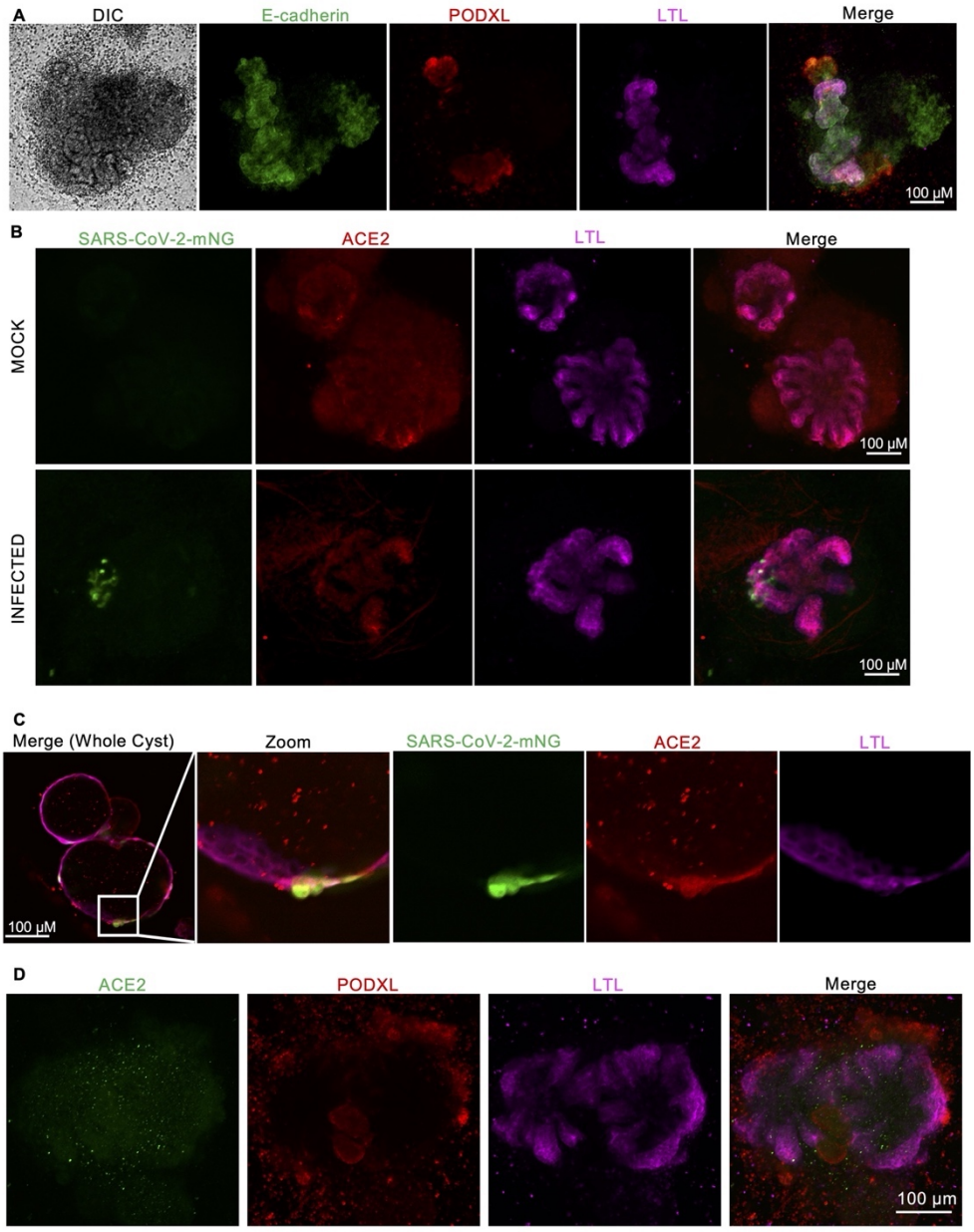

Figure 2.13. ACE2 expression in kidney organoids.

A. Immunofluorescent images of ACE2-/- kidney organoid. B. Immunofluorescent images of MOCK and INFECTED WTC11 kidney organoid (Antibody 1). C. Representative immunofluorescence images of ACE2 in cystic PKD organoids infected with SARS-CoV2-mNG (Antibody 1). D. Immunofluorescences image of uninfected WTC11 kidney organoid (Antibody 2).

Indeed, transcripts encoding both ACE2 and the transmembrane serine protease 2 (TMPRSS2*)*, a co-receptor involved in priming coronavirus for cell entry, were expressed in organoid cultures (60). Interestingly, ACE2 expression trended downward in response to SARS-CoV-2 infection, although not statistically significant (Figure 2.14 C). We previously performed an unbiased single cell RNA sequencing (scRNA-seq) analysis of these kidney organoid cultures, which indicated a total of 11 distinct cell clusters (88). Amongst the 6 of these clusters believed to represent kidney cell types, ACE2 was detected specifically in proximal tubules or early proximal tubules, albeit at relatively low expression levels. These same clusters also expressed several other proposed SARS-CoV-2 entry factors, including *TMPRSS2, FURIN, BSG* (basigin)*, ENPEP* (glutamyl aminopeptidase)*, ANPEP* (alanyl aminopeptidase), *CTSL* (cathepsin L)*,* and *DPP4* (dipeptidyl-peptidase 4), the latter being particularly abundant in proximal tubules. Many of these other entry factors were expressed in additional cell clusters, such as podocytes or stromal cells, often at greater abundance than in proximal tubules (Figure 2.14 D). Overall, these results indicated that SARS-CoV-2 infection of kidney organoids is predominantly mediated by ACE2, and that ACE2 expression may be affected by SARS-CoV-2 infection (119).

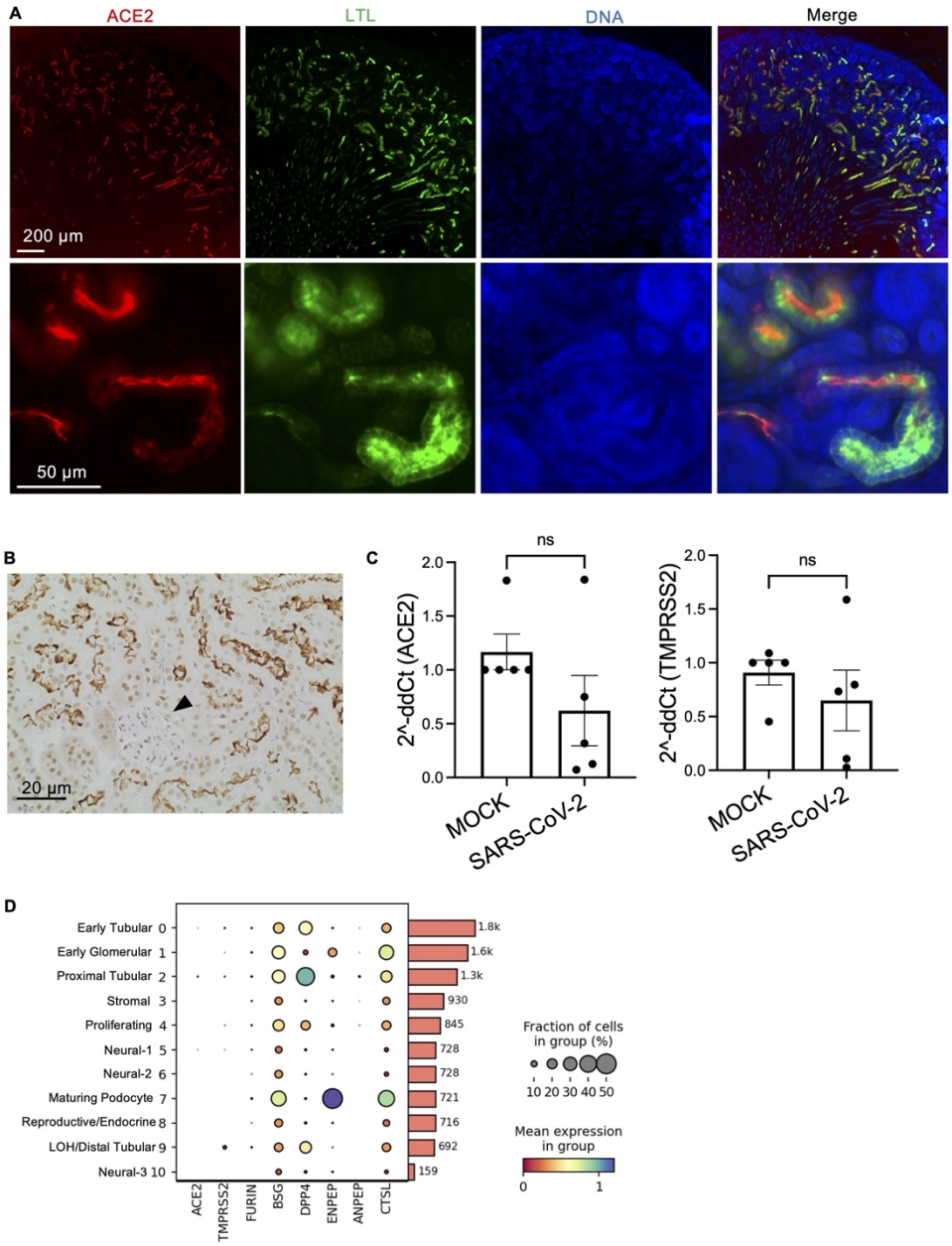

Figure 2.14. Viral entry receptor expression in mice and kidney organoids.

A. Low- and high-magnification immunofluorescence images of cryosectioned kidney tissue (110 days). Images are representative of kidneys from five different sources (Antibody 1). B. Immunohistochemistry of ACE2 in paraffin section of an adult C57BL6 mouse kidney. Black arrowhead indicates a representative glomerulus (Antibody 2). C. qRT-PCR analysis of ACE2 and TMPRSS2 expression in WTC11 mock and SARS-CoV-2 infected organoids. Dots represent

a well of organoids. Mean ± SEM, n ≥ 1 well of organoids per infection from three independent experiments. Unpaired t-test, ns $p > 0.05$. D. Dot blots showing cell type cluster specific expression of SARS-CoV-2 viral entry factors.

2.3.6 *Therapeutics reduce SARS-CoV-2 infection and replication in kidney organoids*

The emergence of SARS-CoV-2 has sparked the rapid development of novel therapeutics aimed to block viral infection and replication (120). The nucleotide analogue prodrug remdesivir was granted emergency use authorization (EUA) for the treatment of COVID-19 in May 2020 for its ability to inhibit viral RNA-dependent RNA polymerase (121). While studies have shown that remdesivir treatment in AKI and CKD patients is tolerated well, the active metabolite of remdesivir is eliminated by the kidneys and has been reported to increase chances of developing AKI in remdesivir-treated patients (122–124). To investigate the efficacy of remdesivir, we infected kidney organoids with SARS-CoV-2 (WA1) or SARS-CoV-2-mNG, and then treated the infected organoids with a 2 μM dose of remdesivir immediately after infection (Figure 2.15 A). This dose was previously determined to be non-toxic to control organoids in titrations of the compound, whereas doses > 8 μM exhibited noticeable toxicity (Figure 2.16 A). Comparable levels of toxicity via Calcein AM/Propidium Iodide staining were noted between control and cystic *PKD2*$^{-/-}$ organoids after 72 hours of treatment (Figure 2.16 B). Supernatants from treated and untreated organoids were collected, revealing 71.4% ± 18% reduced replicated virus in the remdesivir treated organoids (Figures 2.15 B and 2.16 C). Immunofluorescence analysis of remdesivir-treated and untreated organoids indicated comparable levels of SARS-CoV-2-mNG infection and intact podocytes and proximal tubules, suggesting that remdesivir treatment did not have an overtly nephrotoxic effect after 72 hours of treatment (Figure 2.16 D). These data suggest that remdesivir significantly reduces viral replication of infected kidney organoids and supports short-term safety

of remdesivir treatment in kidney cells at the efficacious dose, while cautioning that overdose of the drug may be counterproductive for the kidneys.

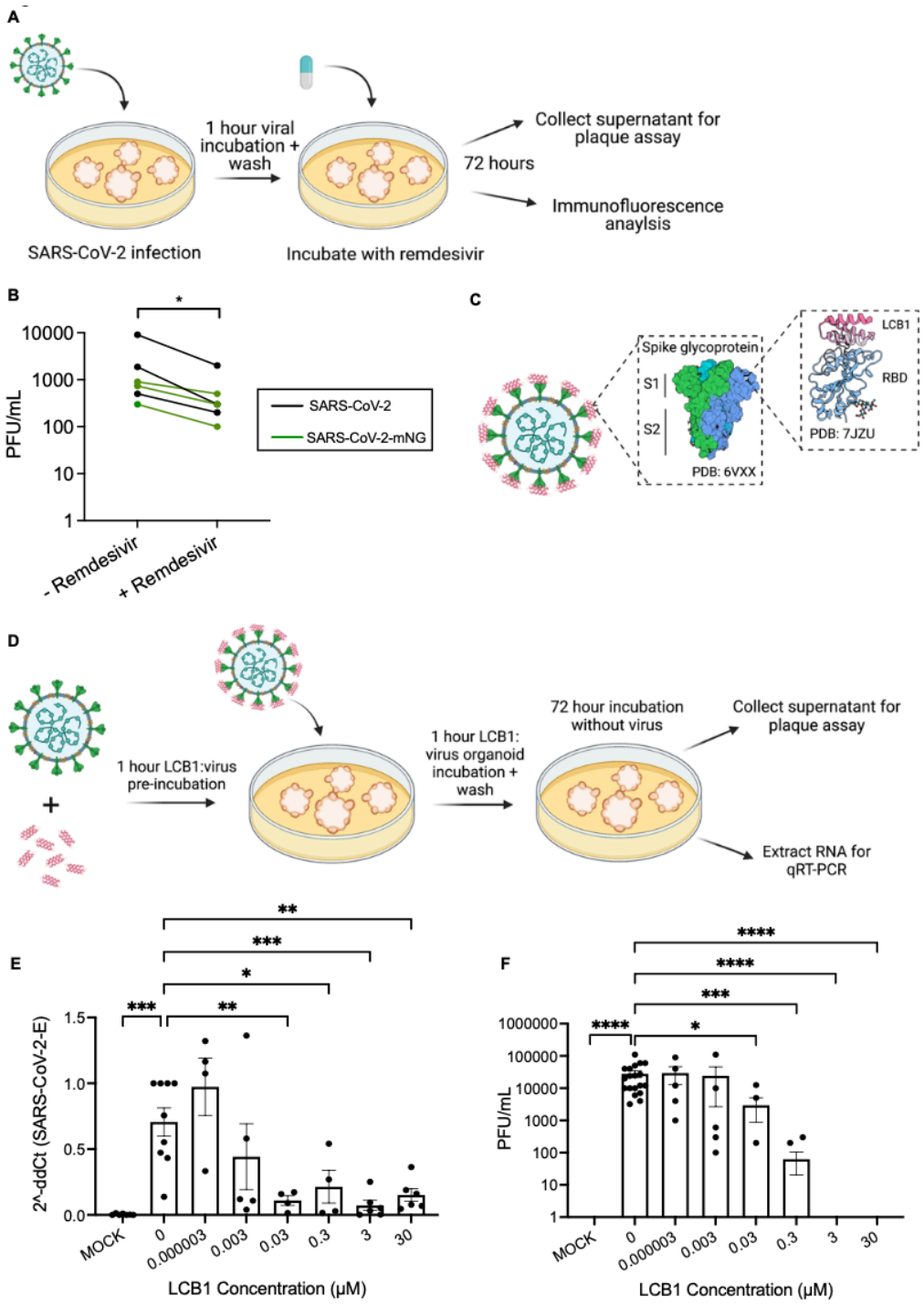

Figure 2.15. Therapeutic interventions reduce SARS-CoV-2 infection and replication in human kidney organoids.

A. Schematic of protocol for SARS-CoV-2 kidney organoid infection with remdesivir treatment. B. Plaque assays of SARS-CoV2 and SARS-CoV-2-mNG infected kidney organoids treated with or without remdesivir. Mean ± SEM of three independent experiments. Wilcoxon matched-pairs signed rank test, *p < 0.05. C. Schematic of LCB1 binding to spike glycoprotein receptor binding domain (RBD). D. Schematic of LCB1 viral pre-treatment and infection of kidney organoids. E. qRT-PCR expression levels of SARS-CoV-2 envelope RNA in infected kidney organoid cultures, with increasing levels of LCB1 protein pre-incubated with virus. Dots represent a well of organoids. Mean ± SEM, n ≥ 1 well of organoids per infection from four independent experiments, 2 iPS and 2 ES, normalized to beta-actin. One-way ANOVA, Kruskal-Wallis post-hoc test, *p < 0.05, **p< 0.01, ****p< 0.0001, ns p > 0.05. F. Plaque assays of SARS-CoV2 infected kidney organoids with increasing levels of LCB1 protein pre-incubated with virus. Dots represent a well of organoids. Mean ± SEM, n ≥ 1 well of organoids per infection from four independent experiments: 2 iPS and 2 ES. One-way ANOVA, Kruskal-Wallis post-hoc test, *p < 0.05, **p< 0.01, ****p< 0.0001, ns > 0.05.

While remdesivir appears to show efficacy *in vitro,* it is not efficacious *in vivo* in lowering mortality or reducing infection in COVID-19 patients, necessitating the development of alternatives (125, 126). The *de novo* designed protein, LCB1, was specifically designed to bind the receptor binding domain of SARS-CoV-2's spike protein at picomolar concentrations and has been estimated to have six-fold greater potency than monoclonal antibodies but has not yet tested efficacy in renal tissues (Figure 2.15 C) (97, 127). To assess whether LCB1 can block SARS-CoV-2 infection and replication in a kidney-relevant system we preincubated 0 μM-30 μM of LCB1 with an MOI of 10 of SARS-CoV-2 for 1 hour, and then added the LCB1:virus mixture to kidney organoids (Figure 2.15 D). qRT-PCR analysis of RNA extracted from infected organoids demonstrated an LCB1 dose-dependent decrease of detectable SARS-CoV-2 transcript, with significantly different levels at 0.03 μM and higher (Figure 2.15 E). Supernatants collected from infected organoids were assessed via plaque assay, revealing a dose-dependent decrease in viral

particles, starting at ≥ 0.03 µM, with complete abrogation at the 3 µM and higher doses (Figure 2.15 F). Thus, LCB1 can efficiently block SARS-CoV-2 infection at levels sufficient to prevent viral replication in human kidney organoids.

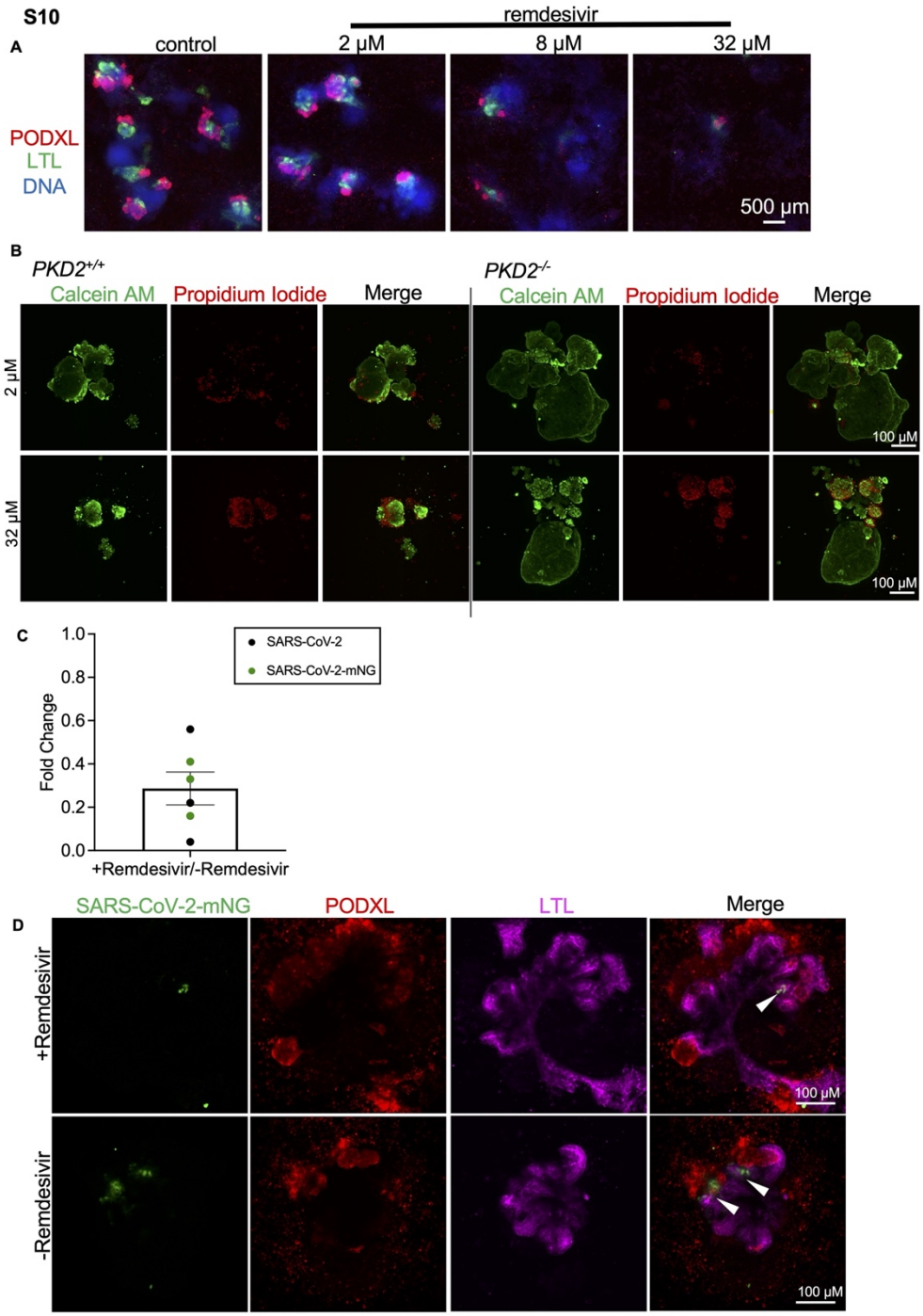

Figure 2.16. Cytotoxicity of Remdesivir in kidney organoids.

A. Representative confocal immunofluorescence and phase images of remdesivir treated kidney organoids. B. Representative confocal immunofluorescence images of live/dead stained *PKD2*$^{-/-}$and *PKD2*$^{+/+}$ remdesivir treated organoids. C. Fold change of SARS-CoV-2 replication of remdesivir treatment organoids compared to DMSO treated controls. Dots represent paired wells of organoids. D. Representative confocal immunofluorescence images of WTC11 SARS-CoV-2 infected organoids with and without 2 μM remdesivir treatment.

2.4 DISCUSSION

Renal involvement in SARS-CoV-2 infection and COVID-19 severity is widely acknowledged, but challenges remain in assessing direct and indirect effects of SARS-CoV-2 infection on the kidneys. Utilizing a fluorescent SARS-CoV-2 reporter virus with infectious properties comparable to native SARS-CoV-2, we directly demonstrate that the proximal tubules are selectively infected in these cultures (87). Our experiments utilizing *ACE2*$^{-/-}$ kidney organoids rigorously demonstrate the requirement for ACE2 mediated viral entry in kidney organoids, despite lacking a well-differentiated brush border. A limitation of the current system is that organoids may reflect a more fetal or dedifferentiated state, compared to adult kidneys in vivo, and lack collecting ducts (28, 32, 33, 128). This must be considered when extrapolating findings from organoids to the clinical context.

Similarly, PKD cysts, which feature a more attenuated epithelium, contain cells expressing ACE2 and LTL that are susceptible to SARS-CoV-2 infection, which likely derive from proximal tubules (91). The extent of infection observed in cystic organoids is similar to control (non-cystic) organoids, suggesting that PKD neither enhances nor protects against SARS-CoV-2, consistent with a clinical report in which ADPKD patients did not have significantly increased major COVID-19 outcomes (129). Evidence of cytotoxicity was more readily discerned in PKD cysts

than in non-cystic tubules, although this may be attributable to the increased ease of imaging cystic organoids. Alternatively, it is possible that increased cell division in the cysts may contribute to a greater susceptibility to injury, as is observed in purified human kidney cells during proliferative expansion in monolayer cultures (59). PKD patients are rare, and none were found amongst our clinical cohort. Further studies are warranted regarding the potential of SARS-CoV-2 to infect and injure PKD cysts in patients compared to non-cystic kidney tissue.

An important question is whether SARS-CoV-2 infection can lead to cytotoxicity in kidney epithelial cells, similar to pulmonary epithelium (130–132). Confocal analysis of infected organoid proximal tubules reveals cell swelling and disrupted LTL marker expression. Cleaved caspase-3 expression and pyknotic nuclei in infected PKD organoids further substantiates infection-induced cytotoxicity. Swelling of the cells might also be suggestive of hypertrophy, which is observed in kidney proximal tubular cells after AKI (133). The higher rates of cell division in our organoid cultures, particularly those with PKD, may contribute to the enhanced sensitivity of these cells to infection-induced injury, compared to spheroids derived from human fetal kidney tissue, which do not show an AKI phenotype (59). Thus, these phenotypes likely reflect an innate, AKI-like program triggered by infection in these human proximal tubular cells.

Our prospective cohort of COVID-19^{+} and COVID-19^{-} patients revealed proteomic upregulation of nine proteins in COVID-19^{+} patient urine, a signature that was also reflected in kidney organoids and kidney cells in patient urines (60). Upregulation of these genes produces significant differences in IFN and IL-10 gene ontology pathways. This supports the hypothesis that AKI in COVID-19 patients may arise as a direct result of kidney infection or a combination of both

systemic and kidney specific response to infection. *In vivo,* such a scenario would necessitate levels of viremia sufficient to spread infection to kidney cells expressing ACE2. Rates of viremia are quite variable, but recent work suggests that viremia may be higher in critically ill COVID-19 patients (134–136). Once infected, such cells might undergo apoptosis to clear the infection from the kidneys, which would make it difficult to detect after the fact. One limitation of urinary proteomics is that low molecular weight proteins can be filtered into the urine from the blood, thus detection of a kidney-specific gene expression signature is challenging and requires cross-validation in organoids and other models.

Interestingly, COVID-19 patients with risk allele genotypes for apolipoprotein L1 (APOL1) have been shown to exhibit a collapsing glomerulopathy phenotype (137, 138). Podocytes were rarely infected in our organoids, likely due to the relatively low levels of ACE2 in these cells (33, 139). In previous work, we have shown that organoids at baseline do not express APOL1, but expression can be induced by treating the cultures with interferon gamma (45). In this regard, it is interesting that a prominent signature of COVID-19 in our AKI patient cohort relates to interferon gamma signaling, which is a known inducer of APOL1 (45, 140–142). Thus, our study suggests that the collapsing glomerulopathy phenotype in COVID-19^{+} risk allele patients may be a consequence of APOL1 induction in podocytes following interferon gamma exposure, rather than direct infection by the virus. Additional studies are needed to determine the precise impact of APOL1 mutations in SARS-CoV-2 induced collapsing glomerulopathy and the role of interferon gamma in this process.

Remdesivir (Veklury) was granted emergency use authorization by the U.S. Food and Drug Administration in May of 2020 for treatment of COVID-19, but more recently, the efficacy of remdesivir for COVID-19 has been challenged (125, 126). The safety and efficacy of remdesivir has not been fully assessed in patients with kidney disease. In animal studies, the kidney was identified as the primary target organ of remdesivir toxicity, and higher levels of remdesivir's metabolite GS-441524 were found in patients with renal dysfunction, suggesting an added risk with remdesivir treatment in those with CKD (143, 144). At a dose of 2 μM, remdesivir was able to significantly reduce viral replication in infected kidney organoids without acutely damaging the epithelial cells, suggesting that a dose providing a balance of safety and efficacy may be achievable. Higher doses were, however, observed to show toxicity in both healthy and control organoids. The C_{max} after injection of a 150 mg dose of remdesivir is 2280 ng/mL, or 3.78 μM concentration in blood, very close to our effective, non-toxic dose used in kidney organoids (143). Our findings suggest that remdesivir should be administered with renal dosing to avoid toxicity to patients with kidney disease. The novel protein, LCB1, designed to prevent SARS-CoV-2's receptor binding domain interaction with ACE2, presents a promising new strategy for treating COVID-19 (97). LCB1 doses of 0.03 μM and higher were able to significantly reduce SARS-CoV-2 transcript levels in organoids infected with an MOI of 10, and the number of viral particles in kidney organoid supernatants. These data suggests that LCB1 can efficiently bind to SARS-CoV-2 and prevent viral replication, even in organoids with detectable infections. One limitation of this strategy is that LCB1 was designed specifically against the receptor binding domain of the SARS-CoV-2/WA1 variant isolated in 2020. As variants emerge, these spike binder proteins may therefore lose potency if their critical binding domains are mutated in the virus, which will necessitate new designs (145).

Indeed, our data suggest that emerging viral variants may also have distinct capacity for infecting the kidney and may lose that capacity with evolving mutagenesis. While all the variants tested – Alpha, Beta, Gamma, Kappa, Delta – have reported heightened rates of transmission, controlled experiments are required to measure viral fitness in specific organ systems (146–148). Our data suggest that infection rates of these viral variants are statistically comparable, but replication rates in the Alpha, Gamma, Kappa, and Delta strains are significantly decreased, reflecting a potential loss of kidney-specific viral replication fitness in those strains. Notably, the Delta strain used in our experiments has a deletion in ORF7a which may contribute to its lack of virulence due to its inability to activate the IFN pathway, although deletions in ORF7a have not been linked with significant functional consequences (87, 149, 150). The SARS-CoV-2-mNG variant we use has the mNG cassette inserted into ORF7A which demonstrates slightly decreased viral replication, but not significantly so (87). Nevertheless, deletions in Delta's ORF7a have been linked with outbreaks in Australia and Uruguay, suggesting this strain retains substantial viral fitness (113, 114). The overall organoid infection and replication findings are consistent with clinical observations of decreasing incidence rates of AKI during the pandemic (151). These data could suggest that viral variants may have differential virulence in extra-pulmonary organs and, in turn, explain differences in clinical rates of AKI and dialysis during the pandemic. It will be vital to collect both viral sequencing data and clinical data in large cohorts to conclude whether viral variants are linked with changes in rates of AKI.

Collectively, our results reveal that SARS-CoV-2 can directly infect and damage kidney tubular epithelial cells in organoids derived from pluripotent stem cells (152). In this regard, kidney

organoid epithelium may model features of lung epithelium in acute respiratory distress syndrome relevant to COVID-19. Data from a controlled human cohort of COVID-19 patients support the physiological relevance of the findings in organoids. The remarkable tropism observed in these organoids, their ability to reveal physiologically relevant injury, and their accessibility to genome editing, together with the availability of urine samples from patients for proteomic analysis, combine to establish a powerful system for studying COVID-19 renal pathophysiology and developing therapeutics (58, 82, 145).

Chapter 3. COMPARTMENTAL AND TEMPORAL ANALYSIS OF MYOSIN DYNAMICS IN POLYCYSTIC KIDNEY DISEASE REVEAL DRUGGABLE PATHWAYS

3.1 INTRODUCTION

3.1.1 *The polycystin proteins and PKD*

Autosomal dominant polycystic kidney disease (PKD) is a common genetic disorder affecting approximately 1 in 400-1000 individuals worldwide (153). PKD causes progressive fluid-filled cysts to develop in renal tubules resulting in a slow decline in kidney function that leads to end-stage renal failure, accounting for 10% of all end-stage renal failure patients (154). PKD is caused by loss of function mutations in either *PKD1* or *PKD2*, which encode the proteins polycystin-1 (PC1) and polycystin-2 (PC2), respectively. Approximately 85% PKD cases are attributable to mutations in *PKD1* and the other 15% of cases to mutations in *PKD2*.

While the genetic underpinnings of PKD have been clearly identified and many mechanistic links have been explored, the definitive molecular PKD pathways that the polycystins govern are still

unclear. PC1 is a large membranous protein with a large N terminal tail that faces the interior of the renal tubular epithelial cell, followed by 11 membrane-spanning domains and a shorter cytoplasmic C terminus (155). While PC1 is found in the cilium of renal tubules, it also localizes to plasma membrane adhesion complexes, and can be shed into urinary exosome-like vesicles, suggesting PC1's role in cell-cell and cell-matrix adhesion, as well as cell-cell signaling (156, 157). PC2 is a membranous protein with 6 membrane spanning domains, an intracellular N and C terminal tail, and sequence homology to the transient receptor potential family of cation channels, lending its overarching function to calcium signaling (158). PC2 localizes to the cilium and endoplasmic reticulum with PC1, but also resides individually in intracellular compartments where it is thought to regulate intracellular calcium stores (159). Due to its large N terminal tail that interacts with renal fluid on the primary cilium, PC1 has also been suggested to act as a mechanosensor that responds to renal fluid flow, interacts with PC2 via their C-terminal tails, and transduces intracellular signals via PC2 to regulate cell replication via multiple intracellular signaling pathways including Wnt, mTOR, G proteins, ß-catenin, and many others (Fig. 3.1) (153, 160).

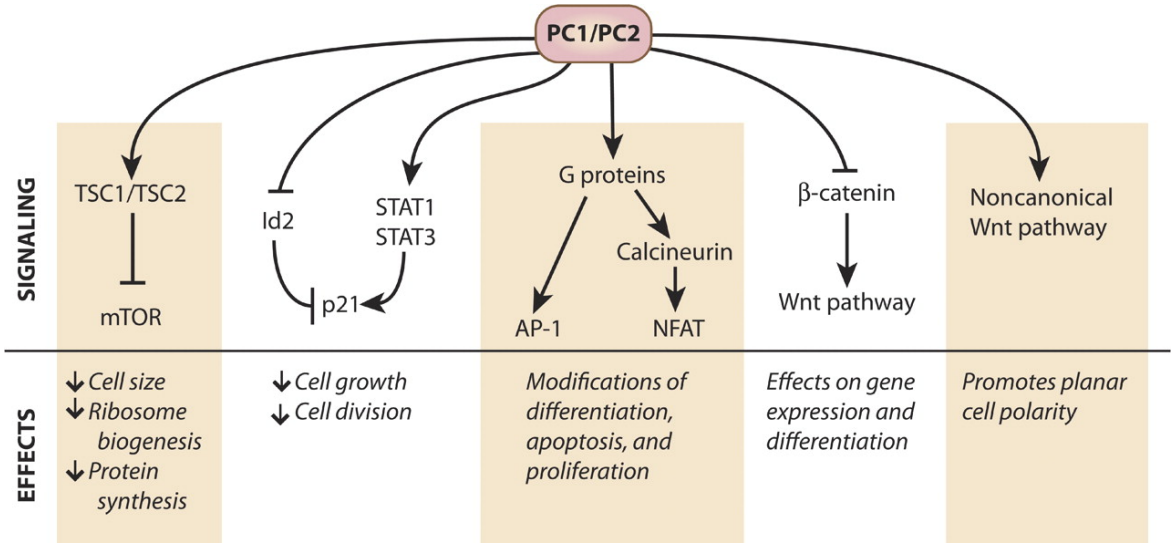

Figure 3.1 Molecular pathways regulated by PC1/PC2.

Adapted from Chapin and Caplan (153). Summary of polycystin pathway regulation and their broad inhibitory effects on cell replication and growth.

The ciliary localization of the polycystins is required for tubular integrity to be retained. Combined inactivation of *Pkd1* or *Pkd2* with co-inactivation of ciliary genes *Kif3a* and *Ift20* demonstrate this requirement for ciliary localization of the polycystins on intact cilia to induce a cystic phenotype in an inducible knockout mouse model of PKD (161). Additionally, the first genetic rescue of *Pkd2* in a conditional inactivation and reactivation mouse model demonstrate that restoring PC2 results in cystic reversion (162). This work suggests that a therapeutic that can rescue polycystin function has the potential to revert PKD pathogenesis which has yet to be done by targeting any of the pathways described above. While our understanding of the polycystins function and their relationship to PKD has improved dramatically, the lack of phenotypically relevant model systems has made it challenging to link molecular function directly to cystic regulation.

3.1.2 *PKD model systems*

Due to its clear genetic background and physiological phenotype, PKD is well suited for disease modeling in stem cell derived kidney organoids due to the ease of gene editing introduced by CRISPR/Cas9 induced knockouts (28, 163). The first stem cell derived PKD organoid were generated in 2015, whereby homozygous deletion of *PKD1* and *PKD2* led to development of hollow, fluid filled cysts *in vitro* compared to isogenic controls (Fig. 3.2) (28).

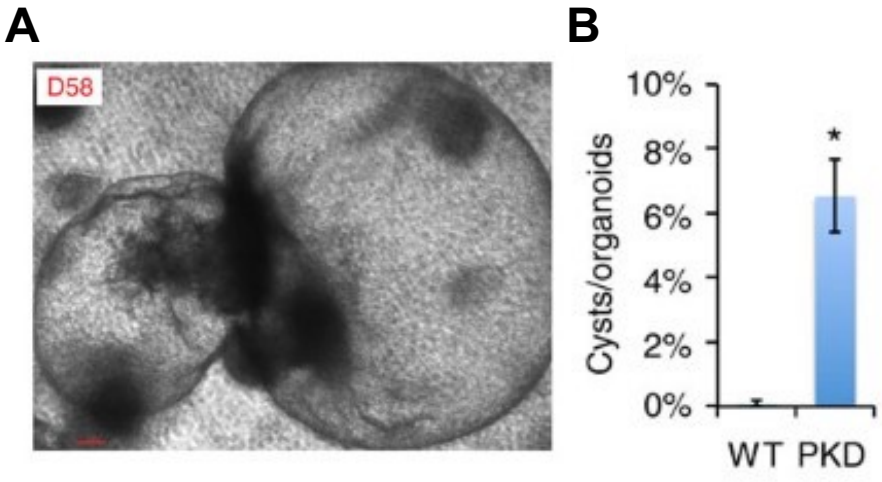

Figure 3.2 CRISPR-edited PKD organoid generate cysts *in vitro*.
Adapted from Freedman et al. (28). A. Brightfield image of cystic PKD kidney organoid. B. Quantification of the percent of PKD vs isogenic control organoids who developed cysts.

PKD organoid cysts stain positive for LTL and E-cadherin (ECAD), most closely resembling prenatal PKD and early stage PKD patients, whereas mature PKD cysts arise from collecting ducts and exhibit prominent fibrotic signatures that are scantly expressed in PKD organoids (91). Additionally, PKD organoids develop cysts at higher rates in suspension culture, supporting a role of cell adhesion and cell-matrix interactions as inhibitors of cyst growth.

Attempts at using patient derived iPSCs to make ADPKD organoids were made, however, variability in differentiation from donor-to-donor confounded PKD-specific results. While homozygous gene edited PKD organoids phenocopy tubular cyst formation, heterozygous gene edited PKD organoids have not been determined to produce spontaneous cysts (44). Prior to gene edited PKD kidney organoids, Madin-Darby canine kidney (MDCK) cells were used for their ability to retain differentiated kidney properties better than cultured primary kidney cells. MDCK cells form vesicles via fluid transport that have cyst-like structure and are thought to better mimic

fluid transport in cysts of PKD patients (164). However, MDCK ‘cysts’ do not phenocopy PKD cysts, as controls can spontaneously develop cyst-like structures as well. To overcome this limitation, monolayer primary cells derived from PKD patients when cultured in collagen matrices were able to proliferate and form spherical fluid-filled monolayered cysts *in vitro*, however, cells from control patients also formed cysts (165). Although these models cannot phenocopy PKD in a PKD-dependent manner, they were used to reveal a critical role of cyclic adenosine monophosphate (cAMP) in cyst enlargement through its role as a secondary messenger in fluid secretion and cellular proliferation was hypothesized. Additionally, these *in vitro* models led to the discovery of a diverse array of molecular networks that the polycystins were implicated in driving PKD pathogenesis (166–170). In addition to MDCK and primary cell 2D cell culture systems, primary kidney cells from different mouse models including mice, rats, and pigs have been employed each with their own benefits and drawbacks compared to kidney organoids (Fig. 3.1). For example, renal porcine LLC-PK1 cells are used to study PKD for their ability to be cultured long-term and prominent cilium that many 2D cell culture models fail to recapitulate (171).

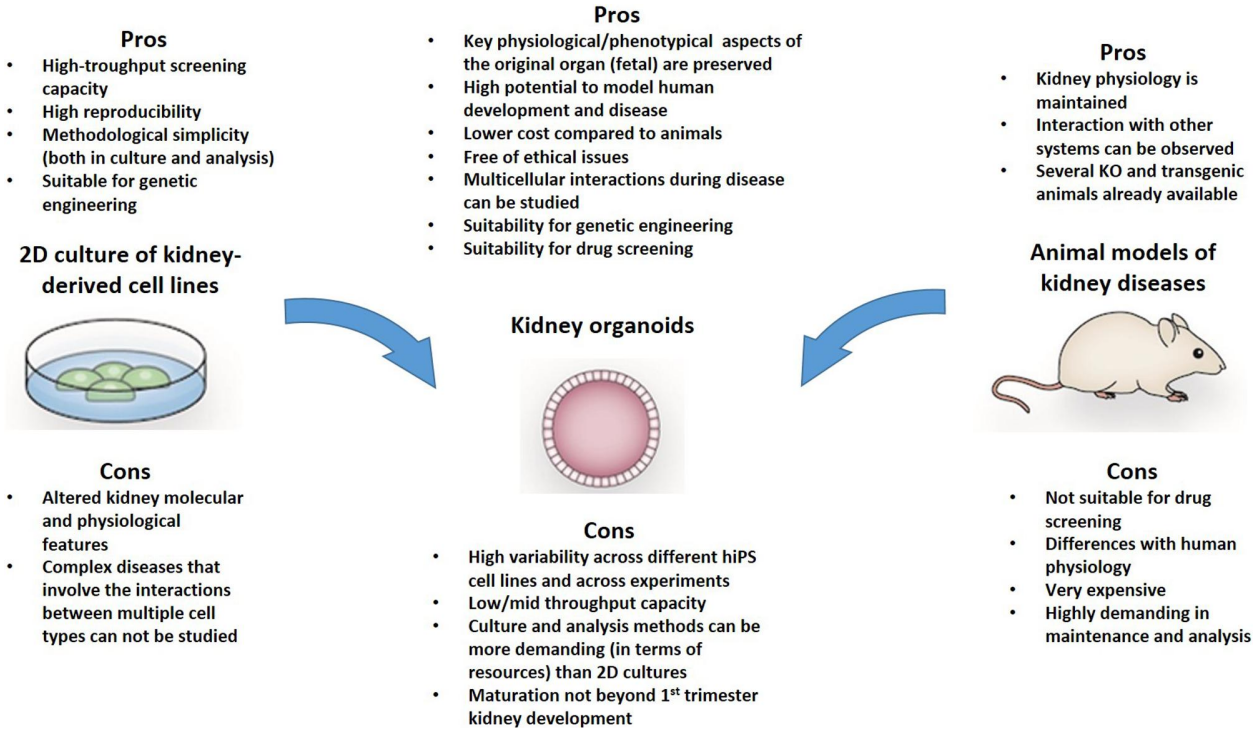

Figure 3.3 Pros and cons of different kidney model systems.

Adapted from Romero-Guevara et al. (172). Descriptive commentary of both the advantages and disadvantages of commonly used kidney model systems ranging from 2D cell culture to *in vivo* models.

In vivo PKD models aim to capture the complexity of the kidney and PKD pathogenesis but face a genetic limitation: heterozygous genetic disruptions of the mouse ortholog *Pkd1* and *Pkd2* do not cause overt cystogenesis in mice and may only develop late-onset cysts, but homozygous disruption is embryonic lethal with bilateral kidney cyst formation starting at E15.5 (173–175). To circumvent this genetic difference between human and murine genetic polycystins, conditional knockout mice have been the primary model of choice for studying PKD. Notably, conditional inactivation of *Pkd1* prior to day 14 results in massive kidney cyst formation within the span of a few days, whereas inactivation after 14 days results in late-onset cyst growth that can take months to develop (176). While this induced trend mimics the heterogeneity in disease severity and onset observed in humans, it remains debated whether these models share similar pathogenesis and cyst

progression seen in human PKD. To address this disparity, a homozygous mutated *Pkd1* model was developed harboring incompletely penetrant R3277C or R2765C mutations in both *Pkd1* alleles mirroring mutations found in a set of human siblings who present with mild progressive cystic disease (177). These specific mutations found in human patients suggest that polycystin dosage correlates with severity of PKD (178). When these mutations are induced in mice, $Pkd1^{RC/null}$ mice develop rapidly progressive disease whereas $Pkd1^{RC/RC}$ mice develop gradual disease into adulthood, most closely mimicking human PKD disease progression. While the $Pkd1^{RC/RC}$ model is the most biomimetic of human PKD disease, the slow developing nature of the cysts still incentivizes the use of conditional knockout *in vivo* models for PKD investigation and drug development.

3.1.3 *Current and developing treatment strategies for PKD*

Treatment strategies for late-stage PKD patients have been primarily limited to dialysis or kidney transplant: both life-altering solutions, fraught with complications. In 2018, the Food and Drug Administration (FDA) drug approved tolvaptan as the first pharmacological treatment of PKD. Founded on studies that showed that vasopressin agonists increased renal cAMP levels and cystogenesis in animal models of PKD, tolvaptan antagonizes V_2 receptors expressed in kidney collecting ducts to reduce cAMP levels and slow cyst growth (179–181). However, in humans, tolvaptan is only moderately effective and causes significant side effects, necessitating the need for improved therapeutics (182).

Many other drugs targeting cell proliferation and cAMP levels have been investigated and failed in clinical trials. mTOR inhibitors known to reduce cell proliferation demonstrated high efficacy

at treating PKD cysts in rodent models (183, 184). However, clinical trials in late-stage PKD patients using the mTOR inhibitor everolimus showed a slow increase in total kidney volume (TKV), but this change did not correlate with patients' glomerular filtration rate (GFR) (185). Early-stage PKD patients treated with the mTOR inhibitor sirolimus also did not have a reduction in TKV nor a difference in GFR, suggesting that mTOR inhibitors are not as potent in humans as they are in rodent models (186).

Somatostatin is a hormone known to inhibit cAMP production in both the kidney and the liver, another organ that develops cysts in PKD, and analogs have been shown to reduce cAMP levels and cyst growth in animal models (187, 188). Multiple clinical studies have been conducted using octreotide and lanreotide suggesting that these somatostatin analogs can reduce liver volume but are unclear about rescuing kidney volume due to variability from study to study and have no significant or consistent effects on rescuing GFR decline (189–191). Tesevatinib, a multi-kinase inhibitor known to decrease cAMP levels, activity of GFR, and reduce abnormal angiogenesis necessary for cystic growth, has shown efficacy in animal models of PKD and is currently being used in Phase II clinical trial in ADPKD patients (192). While the proliferative and metabolic hallmarks of PKD have been the primary drug targets to date, these drugs have largely failed to make a dent in PKD clinically because we do not yet clearly understand the pathway involved.

Recently, the cytoskeletal components of PKD have been evaluated as potential therapeutic targets, particularly targeting the contractile myosin motor proteins. Myosins are a family of motor proteins with an adenosine triphosphate (ATP)ase motor that drives cell motility, adhesion, and general force and movement of all cells by exerting pulling forces on the actin cytoskeleton (193).

The kidney primarily expresses two myosin proteins: non-muscle myosin 2A (NMIIA) primarily in the podocytes, and non-muscle myosin 2B (NMIIB) at low levels throughout the entirety of the kidney (194). NMIIs are composed of two heavy chains, two essential light chains, and two regulatory light chains that get conformationally and functionally regulated by phosphorylation of the regulatory light chains (195). NMIIs two globular head domains facilitate actin binding and the ATPase motor activities to facilitate actin translocation, while phosphorylation of the regulatory light chains induces NMII conformational changes to allow for proper actin association of the myosin protein. Developmental studies assessing NMIIA and NMIIB's role in kidney development reveal that MM-specific deletion of *Myh9* and *Myh10* cause tubular dilations of proximal tubules hypothesized to be from reduced apical tension (196). Additionally, UB-specific deletion of *Myh9* and *Myh10* caused developing epithelia to produce apical extrusions potentially explained by reduced apical constriction and reduced adhesion to neighboring cells (197).

Specific to PKD, PC1 is suggested to have a C terminal calmodulin (CaM) binding domain that when ablated, disrupts the hypothesized PC1/PC2 calcium signaling, hinting at myosin's function in PKD (194). In other work, Rho associated protein kinase (ROCK) inhibitors, fasudil and Y-27632, that inhibit phosphorylation of the myosin light chains, were found to decrease cystogenesis in a 3D-cultured *PKD1*$^{-/-}$ mIMCD3 cells and inducible *Pkd1*$^{-/-}$ mice (199, 200). While these collective results indicate differences between organoids, mIMCD3 cells, and mice and pose a challenge for a consensus in drug development, they do indicate that myosin is a key targetable pathway to modulate PKD pathogenesis and indicate that PC1/2 may have roles in regulating the cytoskeleton via myosin contractility. The following work will investigate the role of myosin in

PKD pathogenesis and how different myosin activators and inhibitors could target and affect the kidney cytoskeleton in relationship to PKD.

3.2 Materials and Methods

Cell Generation. Experiments were performed using wild-type WTC11 iPS and H9 ES cell lines, and a two *PKD2*$^{-/-}$ and two *PKD1*$^{-/-}$ clones (WTC11 and H9 background), generated and characterized as described previously (28). Altogether these represent two distinct genetic backgrounds, genders, and cell types: (i) male WTC11 iPS cells (Coriell Institute Biobank, GM25256) and (ii) female H9 ES cells (WiCell, Madison Wisconsin, WA09).

Kidney organoid differentiation. Work with iPS and ES cells was conducted under the approval and auspices of the University of Washington Embryonic Stem Cell Research Oversight Committee. Specific cell lines used in this study are described below and are sourced from commercially available iPS and ES cell lines obtained with informed consent. Stem cell stocks were maintained in mTeSR1 media with daily media changes and passaging using Accutase (STEMCELL Technologies). 1,000-6,000 cells per well were placed in each 24-well plate pre-coated with 300 µL of DMEM-F12 containing 0.2 mg/mL Matrigel and sandwiched the following day with 0.2 mg/mL Matrigel in mTeSR1 (STEMCELL Technologies) to produce scattered, isolated spheroid colonies. 48hrs after sandwiching, spheroids were treated with 12µM CHIR99021 (Tocris Bioscience) for 36hrs, then changed to RB (Advanced RPMI + 1X Glutamax + 1X B27 Supplement, all from Thermo Fisher Scientific) and replaced every 3 days thereafter. Organoids were differentiated for 21 days from the time of plating, at which time tubular structures had formed. Gene edited *PKD2*$^{-/-}$ organoids were picked from the adherent plate at day 21, placed

in suspension culture with RB media replaced every 3 days until day 30 when cyst growth was prominent (91).

Pre-cystic 6 well drug treatments. Day 18-21 differentiated organoids were picked and placed in suspension culture and distributed evenly into low-attachment 6 well plates (Corning). 2 mLs of RB media with specified drug amount is added to the organoids and treated Monday, Wednesday, Friday, for a total of 14 days. To treat after the first day, 1 mL of media is removed, and 1 mL of 2X drug concentration treated media is replaced. Organoids are imaged and quantified for cyst presence and 2D cyst area using Fiji image analysis software.

Post-cystic 96 well drug treatments. Day 30-40 cystic PKD organoids growing in suspension culture were placed into low-attachment 96 well U-bottom plates (Corning). 200 µL of RB media with specified drug amount is added to the organoids and treated Monday, Wednesday, Friday, for a total of 14 days. To treat after the first day, 100 µL of media is removed, and 100 µL of 2X drug concentration treated media is replaced. Organoids are imaged and quantified for total fold change in growth from day 0 to day 14.

Immunostaining. Immunostaining followed by confocal microscopy was used to localize various proteins and transporters in the cysts and organoids. Prior to staining, organoids and tissues were fixed in 4% PFA for 30 mins at room temperature. After fixing, samples were washed in PBS, blocked in 5% donkey serum (Millipore)/0.3% Triton-X-100/PBS, incubated overnight in 1% bovine serum albumin/0.3% Triton-X-100/10µM $CaCl_2$/PBS with primary antibodies, washed, incubated with Alexa-Fluor secondary antibodies (Invitrogen), washed and imaged. Primary

antibodies include Biotinylated LTL (Vector Labs B-1325, 1:500), pMLC2 Ser19 (Cell Signaling Technology, 3675S 1:250), DAPI (Cayman Chemical 14285, 1:1000), αSMA (Sigma-Aldrich, C6198, 1:500), NMIIB (Cell Signaling Technology, 8824S, 1:500), PDGFRß, (Abcam, Ab32570, 1:250). Live and dead staining used Calcein AM (Invitrogen) and Propidium Iodide (Thermo Fisher) per manufacturer's instructions. Fluorescence images were captured using a Nikon A1R inverted confocal microscope with objectives ranging from 10X to 60X.

CRISPR-Cas9 gene editing. Constructs encoding green fluorescent protein-tagged Cas9 (Addgene 44719) and a guide RNA (Addgene 64711) targeting PKD1 (5′-CGCACGTGTGCCCCGGTA-3′) were transiently transfected into AICS-0024 (NMIIB-GFP) iPSCs, and green fluorescent protein-expressing cells were isolated by flow cytometric sorting, clonally expanded, and screened for clones with biallelic loss-of-function indels. Chromatogram sequences were analyzed using Synthego ICE software.

Live contractile imaging. NMIIB-GFP-*PKD1*$^{-/-}$ and NMIIB-GFP-*PKD1*$^{+/+}$ organoids were differentiated until day 21, treated with 25 μM EMD or equivalent volume of DMSO. Immediately after treatment, images were taken through the entire organoid at Z step sizes of 10 μM every 3 minutes, for 30 minutes on Nikon Ti Inverted Wide-field microscope equipped with a 37 degree Celsius incubator and CO_2 chamber.

Live cystogenesis imaging. NMIIB-GFP-*PKD1*$^{-/-}$ were differentiated until day 21, picked and placed in suspension culture, and then reattached to a 96 well μclear black well plate (Greiner Bio-One) coated with an extracellular matrix of collagen IV, laminin, and fibronectin to facilitate

organoid attachment. Images were taken through the entire organoid at Z step sizes of 10 μM every 5 minutes, for 48 hours on a Zeiss motorized AxioObserver for Spinning Disk equipped with a 37 degree Celsius incubator and 5% CO_2 chamber.

Animal Experimentation. All animal experimentation was approved by the University of Washington's Institutional Animal Care and Use Committee. *Pkd1*$^{RC/RC}$ were used for all experiments and were a generous gift from Dr. Peter Harris. Mice were intra-peritoneally injected 3 times per week for two weeks. Kidneys were then harvested, fixed, cryo-sectioned, and immunofluorescently stained as described above. Histological tissue processing and PAS staining was performed by the Histology and Imaging Core at the University of Washington.

Statistical Analysis. Quantification was performed on data obtained from experiments performed on controls and treatment conditions side by side on at least three different occasions or cell lines (biological replicates). Error bars are mean ± standard error (SEM). Statistical analyses were performed using GraphPad Prism Software. Statistical analyses were only performed for experiments with more than two replicates. Statistics are plotted on the respective figures and the tests used are described in the figure legends.

3.3 RESULTS

3.3.1 *Myosin activation can reduce and slow cyst growth in PKD organoids*

Previous work has demonstrated that PKD organoids develop cysts more rapidly and at a larger scale when treated with the myosin inhibitor blebbistatin (33). To investigate whether myosin activators could do the opposite, and potentially prevent or revert cyst growth in PKD organoids,

Emanuel Merck Darmstadt 57033 (EMD), a well-studied myosin activating drug, was used to treat PKD organoids prior to developing cysts for 14 days and assessed for relative cyst presence and cyst size (Fig. 3.4) (201). 50 μM of EMD was able to significantly reduce the percent cystic and cyst area, while 25 μM trended to prevent and reduce cyst growth as well (Fig. 3.4 B, C). To assess whether PKD organoids that had already developed cysts also responded to EMD treatment, post-cystic PKD organoids were treated with EMD for 14 days and assessed for their total fold change in area due to cysts already being present (Fig. 3.5).

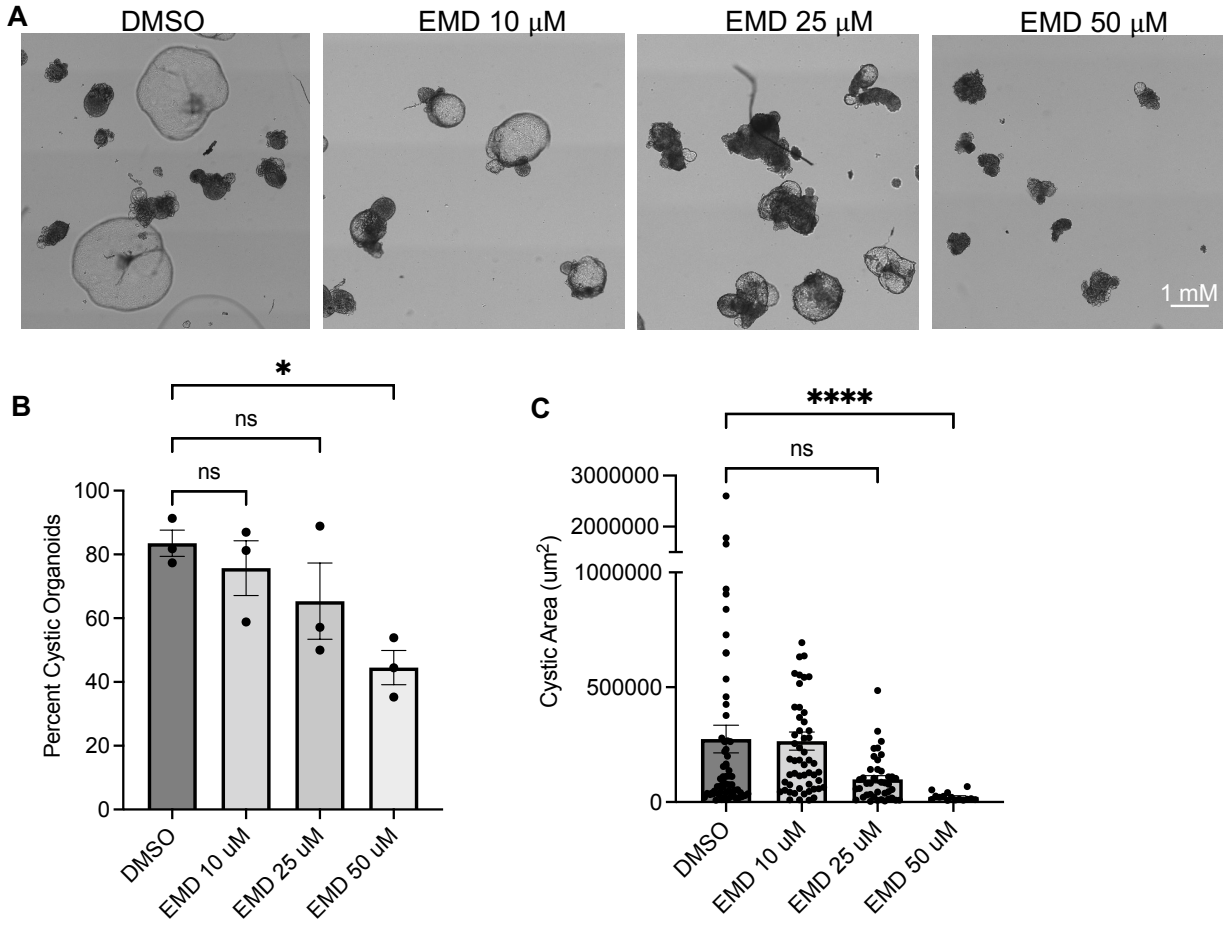

Figure 3.4 Pre-cystic treatment of PKD organoids with EMD reduces cross-sectional cyst area.

A. Representative brightfield images of PKD organoids treated for 14 days with EMD or DMSO.

B. Percent of cystic organoids after 14 days of drug treatment. Dots represent a well of organoids. Mean ± SEM, n ≥ 10 organoids per treatment from three independent experiments.

One-way ANOVA, Kruskal-Wallis post-hoc test, *p< 0.05, ns p > 0.05. C. Quantification of cyst cross-sectional area of PKD organoids after 14 days of treatment. Dots represent a single cystic area. Mean ± SEM, n ≥ 10 organoids per treatment from three independent experiments. One-way ANOVA, Kruskal-Wallis post-hoc test, ****p< 0.0001, ns p > 0.05.

Both 25 μM and 50 μM doses of EMD were unable to block cyst growth and were just above significance threshold to show a significant slowing of cyst growth, although EMD treated organoids had slower trends of cyst growth (Fig. 3.5 B). Live/dead analysis of EMD treated organoids revealed that even the highest doses of EMD are not significantly toxic to treated organoids (Fig. 3.5 C).

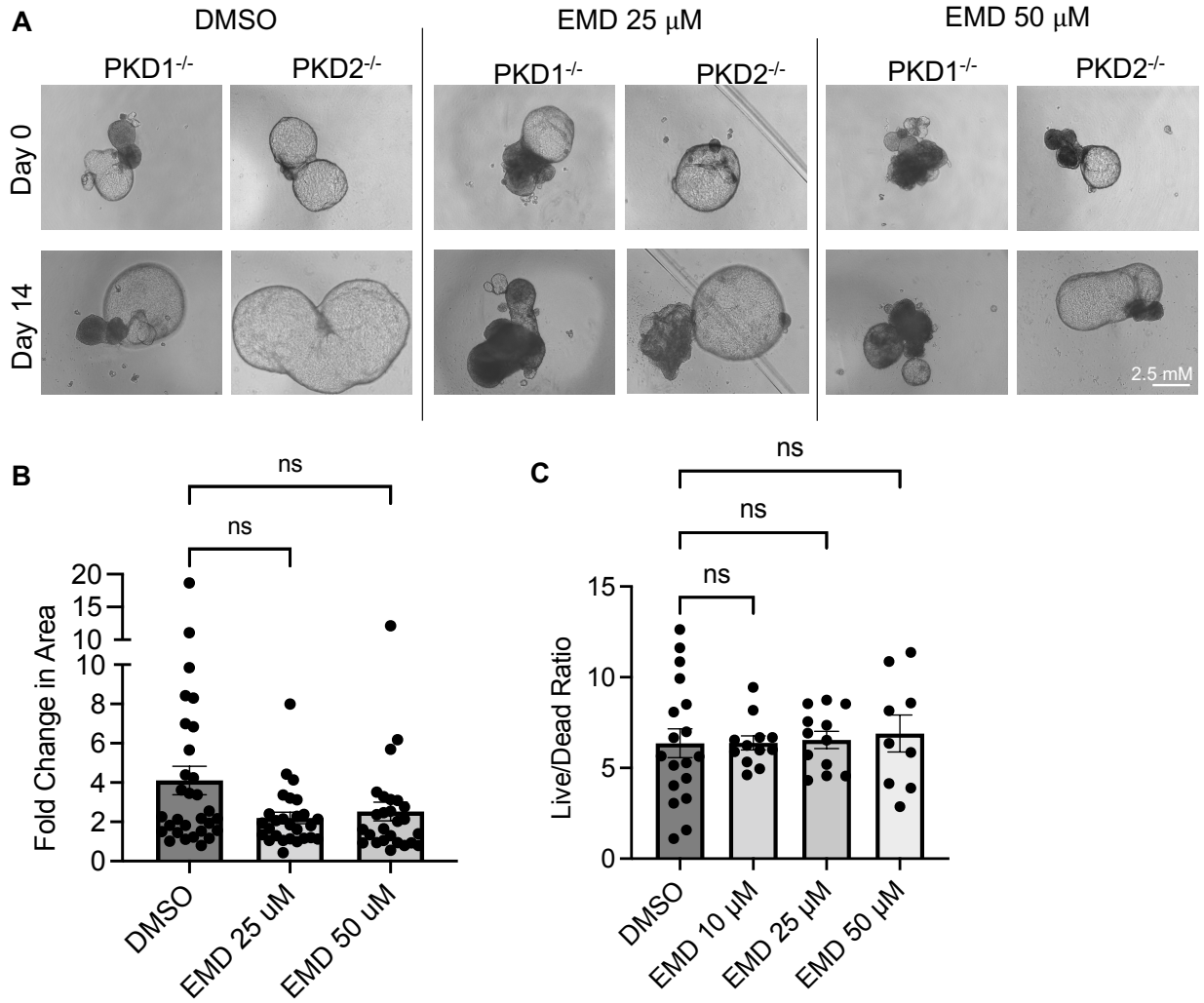

Figure 3.5. Post-cystic treatment of PKD organoids with EMD slows cyst growth. A. Representative brightfield images of PKD organoids treated for 14 days with EMD or DMSO. B. Quantification of fold change of total area of organoid after 14 days of drug treatment. Mean ± SEM, $n \geq 6$ organoids per treatment from three independent experiments. One-way ANOVA, Kruskal-Wallis post-hoc test, ns $p > 0.05$. C. Quantification of Calcein AM (Live) and propidium iodide (Dead) signal intensity of stained drug treated organoids. Mean ± SEM, $n \geq 6$ organoids per treatment from three independent experiments. One-way ANOVA, Kruskal-Wallis post-hoc test, ns $p > 0.05$.

Interestingly, when pre-cystic PKD organoids are treated with a combination of 10 μM EMD and 10 μM of blebbistatin, cyst areas are significantly reduced suggesting a potential drug interaction that can create a synergistic effect on cyst growth (Fig. 3.6 A, B, C). Additionally, only after 7 days of treatment do PKD organoids start to develop a difference in cystic areas, indicating that drug treatment responses need to be observed over longer periods of time of at least 1 week (Fig. 3.6 D).

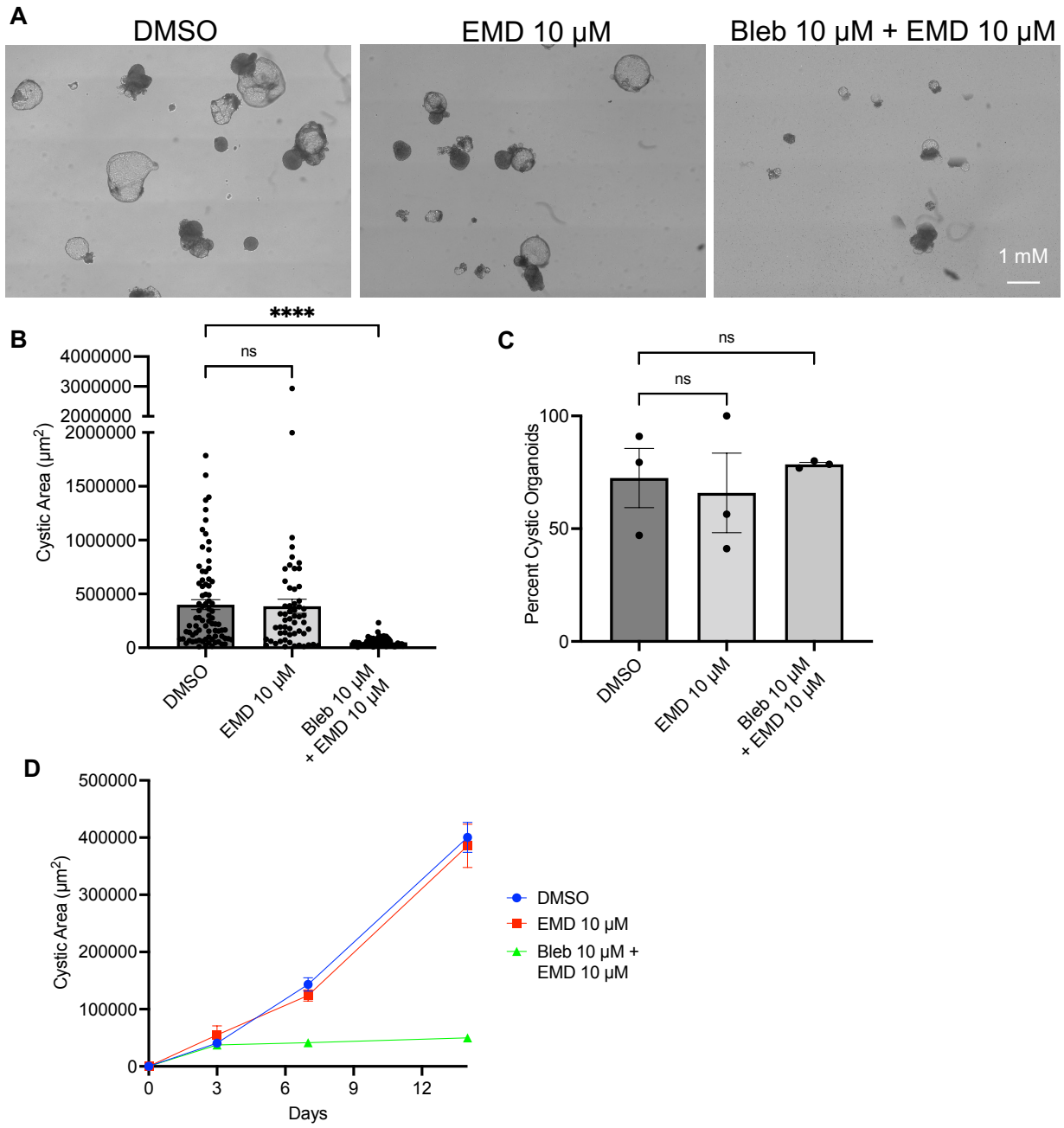

Figure 3.6. Blebbistatin in combination with EMD prevents cyst growth in PKD organoids. A. Brightfield images of PKD organoids treated with drugs for 14 days. B. Quantification of cystic area after 14 days of drug treatment in PKD organoids. Mean ± SEM, n ≥ 10 organoids per treatment from three independent experiments. One-way ANOVA, Kruskal-Wallis post-hoc test, ns $p > 0.05$, **** $p < 0.0001$. C. Percent of cystic organoids after 14 days of drug treatment. Dots represent a well of organoids. Mean ± SEM, n ≥ 10 organoids per treatment from three

independent experiments. One-way ANOVA, Kruskal-Wallis post-hoc test, ns $p > 0.05$. D. Quantification of cyst area over 14 days of drug treatment. Mean ± SEM, $n \geq 10$ organoids per treatment from three independent experiments.

3.3.2 *Myosin light chain inhibitors have no effect on PKD organoid cyst growth*

Myosin's contractility can be regulated at multiple sites in its protein architecture. EMD and blebbistatin target myosin's heavy chains, but multiple drugs known to inhibit myosin's light chains and have been shown to rescue cyst growth in 3D-cultured *PKD1*$^{-/-}$ mIMCD3 cells and inducible *Pkd1*$^{-/-}$ mice (199, 200). To assess whether myosin light chain inhibitors prevent PKD cystogenesis in our kidney organoids, we treated pre-cystic PKD organoids with increasing doses of the myosin light chain inhibitors ML7 and Y-27632 (ROCK) for 14 days as described above. Neither ML7 nor ROCK significantly prevented nor exacerbated cystogenesis over 14 days of drug treatment (Fig. 3.7).

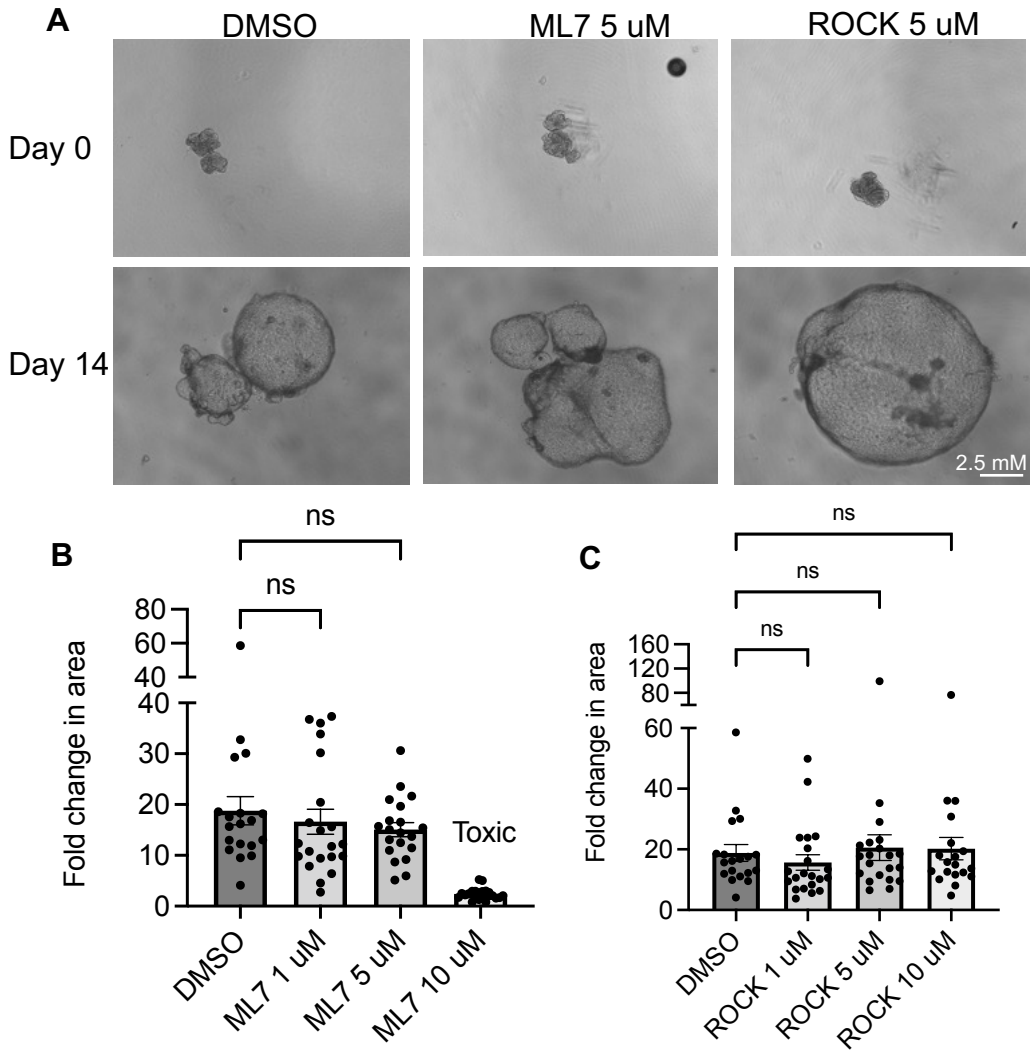

Figure 3.7. Myosin light chain inhibitors do not influence PKD organoid cystogenesis. A. Brightfield images of PKD organoids before and after two weeks of drug treatment. B. Quantification of ML7 drug treatment effect on organoid area before and after drug treatment. Mean ± SEM, n ≥ 6 organoids per treatment from two independent experiments. One-way ANOVA, Kruskal-Wallis post-hoc test, ns $p > 0.05$. C. Quantification of ROCK drug treatment effect on organoid area before and after drug treatment. Mean ± SEM, n ≥ 6 organoids per treatment from two independent experiments. One-way ANOVA, Kruskal-Wallis post-hoc test, ns $p > 0.05$.

To assess whether myosin light chain inhibitors affect cyst growth in kidney organoids that were already cystic, we treated 30-day old cystic PKD organoids with increasing doses of the myosin light chain inhibitors ML7 and ROCK for 14 days as described above. Neither ML7 nor ROCK significantly slowed, reverted, or exacerbated cyst growth over 14 days of drug treatment (Fig. 3.8). These findings suggest that the myosin heavy chains are the primary druggable targets for regulating PKD cystogenesis.

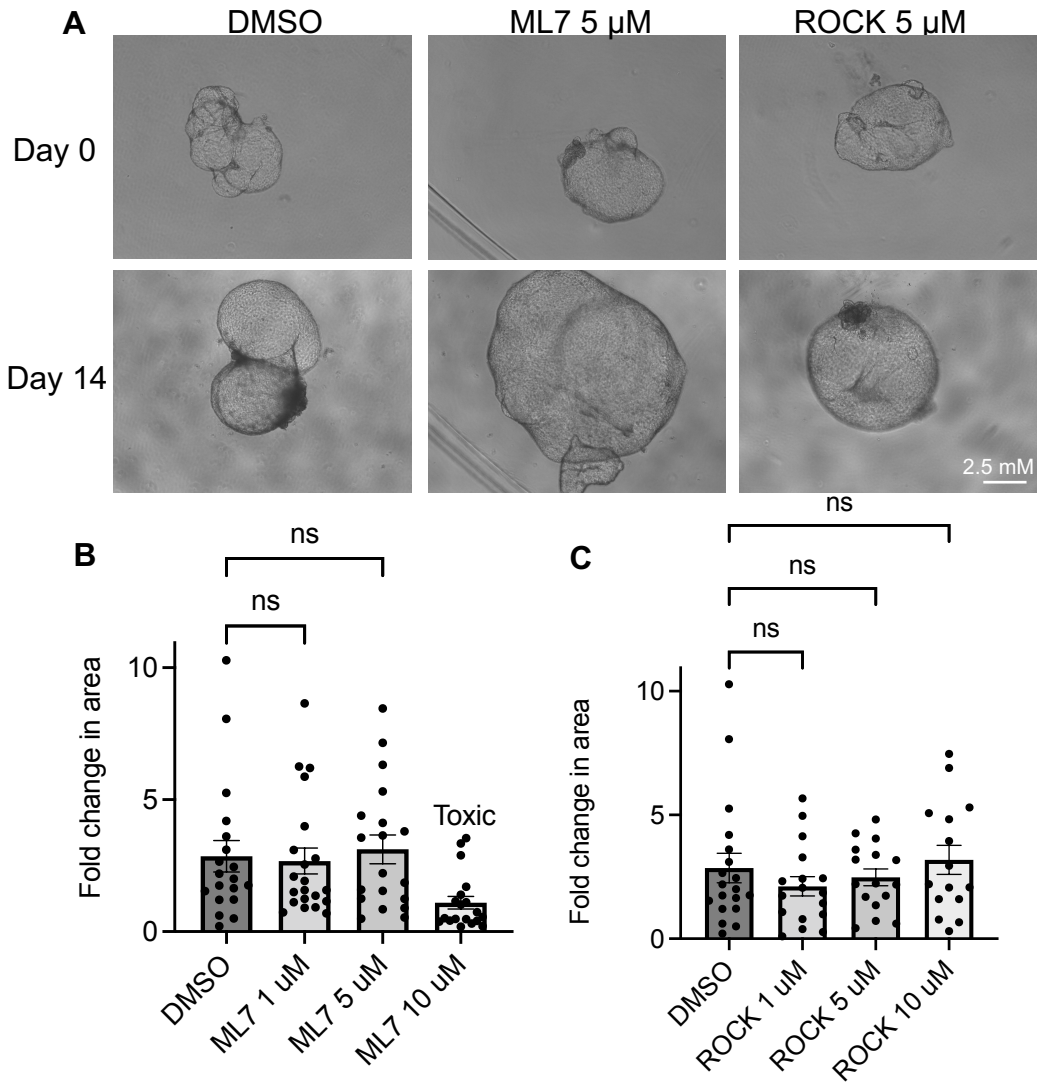

Figure 3.8. Myosin light chain inhibitors do not influence PKD organoid cyst expansion. A. Brightfield images of cystic PKD organoids before and after two weeks of drug treatment. B. Quantification of ML7 drug treatment effect on organoid area before and after drug treatment.

Mean ± SEM, n ≥ 6 organoids per treatment from two independent experiments. One-way ANOVA, Kruskal-Wallis post-hoc test, ns $p > 0.05$. C. Quantification of ROCK drug treatment effect on organoid area before and after drug treatment. Mean ± SEM, n ≥ 6 organoids per treatment from two independent experiments. One-way ANOVA, Kruskal-Wallis post-hoc test, ns $p > 0.05$.

3.3.3 *NMIIB dynamics in PKD organoids reveal a potential therapeutic mechanism of EMD treatment*

EMD has never been studied in the context of non-muscle myosins which are the predominant two-headed myosin expressed in the human kidney and in our kidney organoids. Non-muscle myosin II B encoded by *MYH10* is the most highly expressed in the kidney organoid tubules where PKD cysts arise (Fig. 3.9) (194).

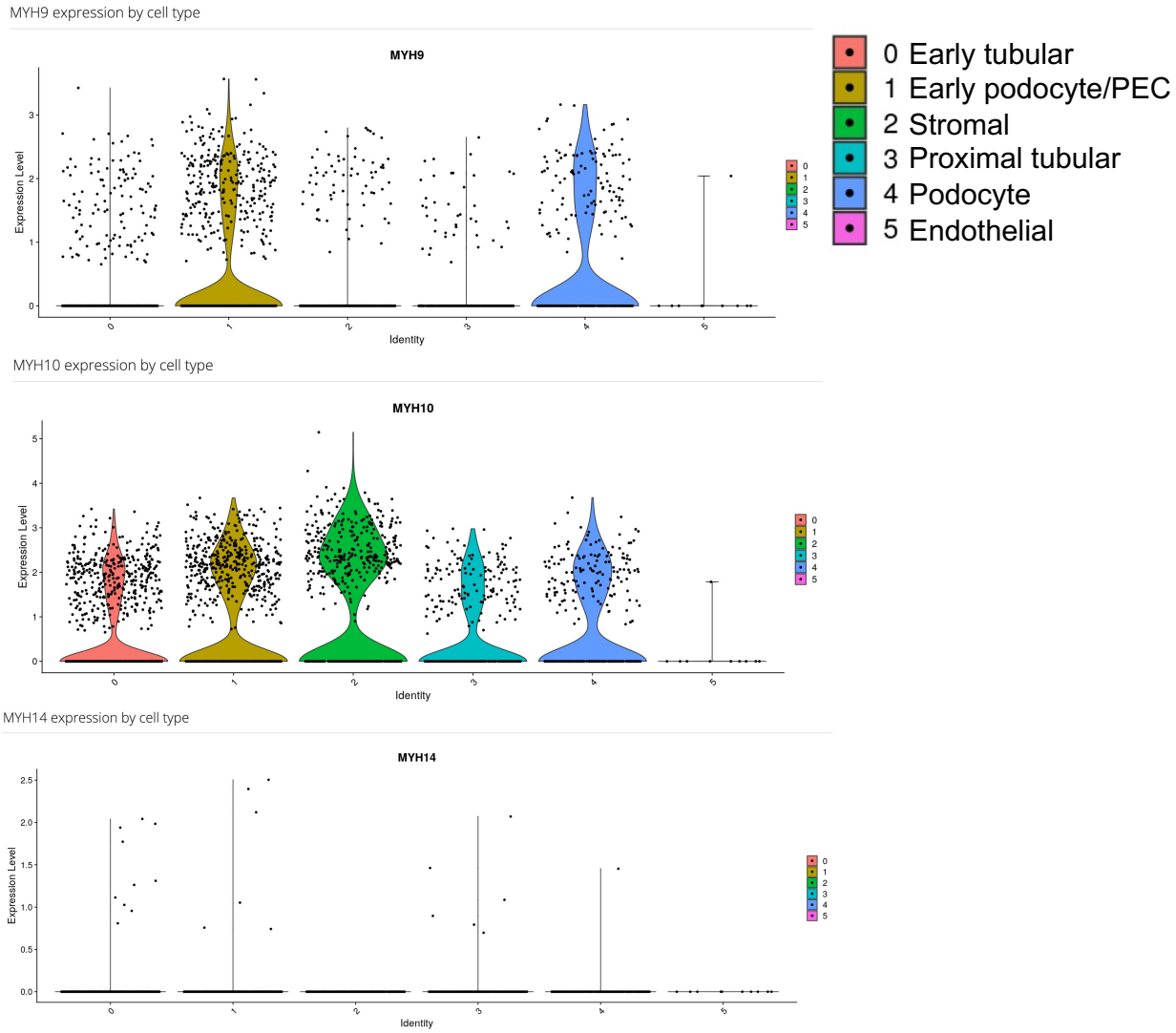

Figure 3.9. Bulk RNAseq expression of non-muscle myosin in kidney organoids. Bulk RNAseq expression levels of *MYH9*, *MYH10*, and *MYH14* in clustered kidney organoid cell types.

To assess how EMD is affecting myosin in PKD tubules, we utilized the Allen Cell Institute's NMIIB fluorescently tagged human iPSC cell line and induced knockout of *PKD1* using CRISPR/Cas9 (202). NMIIB-GFP-*PKD1*$^{-/-}$ and NMIIB-GFP-*PKD1*$^{+/+}$ isogenic pairs were then differentiated into kidney organoids and assessed for cyst production in NMIIB-GFP-*PKD1*$^{-/-}$ organoids and proximal tubular expression via LTL staining (Fig. 3.10).

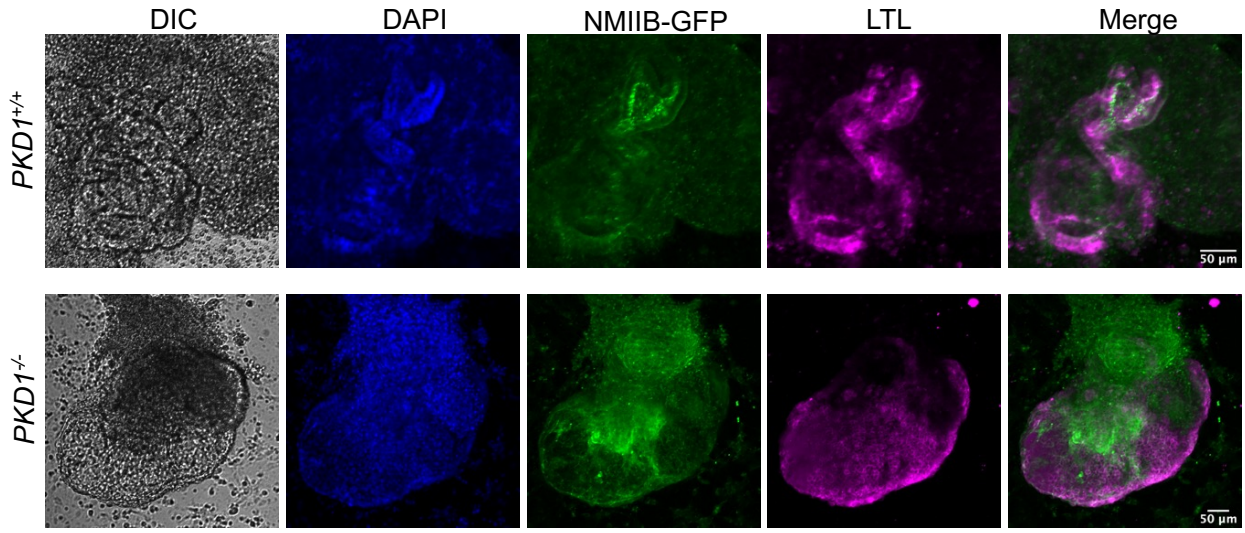

Figure 3.10. NMIIB-GFP-*PKD1*$^{-/-}$ organoids express tubular structures and produce cysts. Immunofluorescent max intensity projections of NMIIB-GFP-*PKD1*$^{-/-}$ and NMIIB-GFP-*PKD1*$^{+/+}$ isogenic pairs differentiated until day 30.

As expected, NMIIB-GFP-*PKD1*$^{-/-}$ organoids produced cysts after 30 days after kidney organoid differentiation while their NMIIB-GFP-*PKD1*$^{+/+}$ counterparts did not. NMIIB was expressed throughout the organoid body and cyst body, particularly in the apical membrane of the LTL+ proximal tubules.

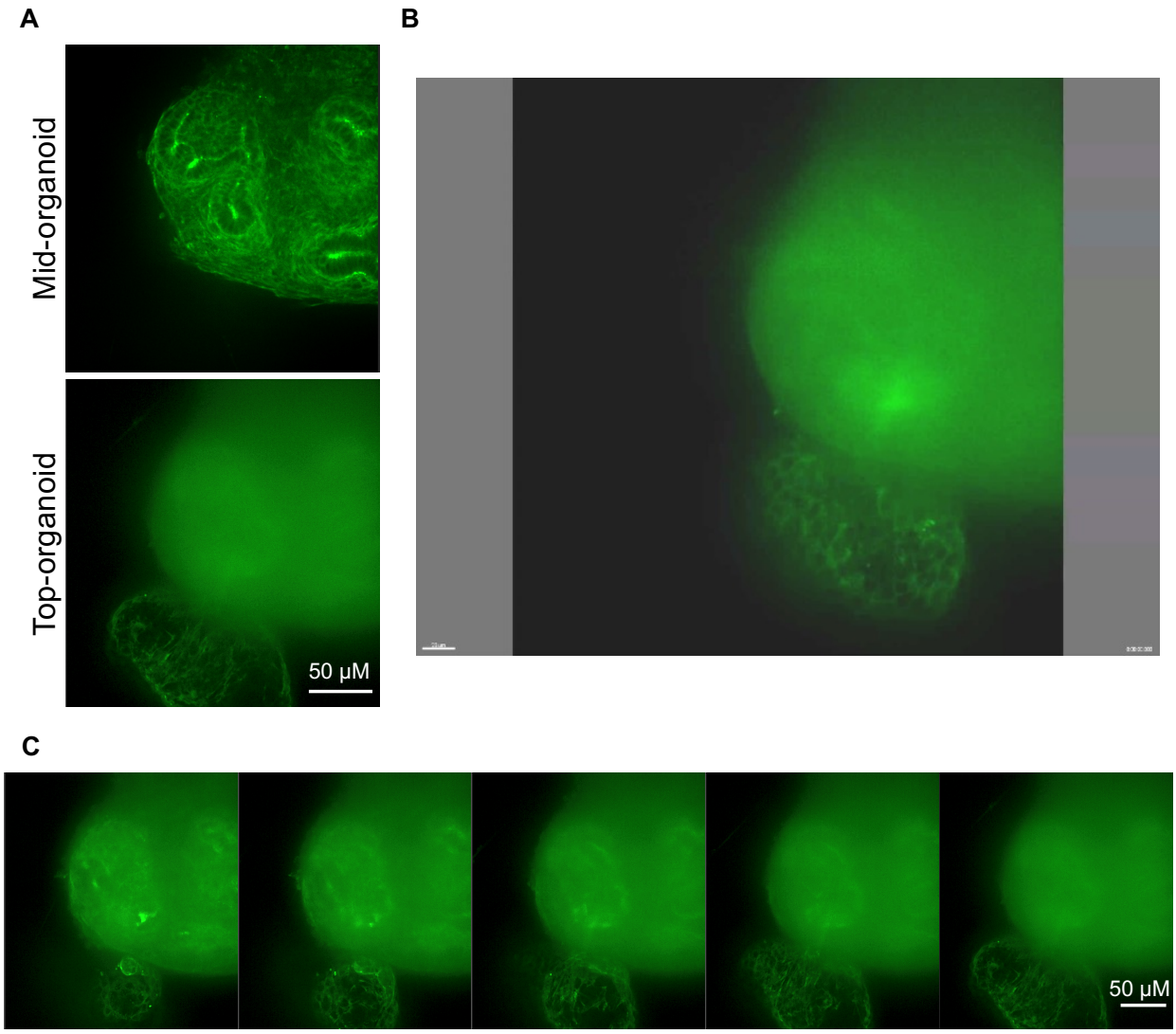

Figure 3.11 PKD cystogenesis triggers myosin stretching in expanding cyst

A. Immunofluorescent images of NMIIB-GFP-*PKD1*$^{-/-}$ organoids through the organoid body and cystic body. B. Live video of cystogenesis from a NMIIB-GFP-*PKD1*$^{-/-}$ organoid. C. Single frames taken every five minutes (left to right) of cystogenesis in NMIIB-GFP-*PKD1*$^{-/-}$ organoid.

To assess how myosin dynamics in the kidney change as cysts emerge, we took live imaging Z-stacks of pre-cystic NMIIB-GFP-*PKD1*$^{-/-}$ organoids every 5 minutes over a 48-hour time period. During this series of imaging, a single cyst initiating event occurred in which NMIIB was expressed throughout the organoid body, enriched on the apical membrane of tubules, but appeared stretched along the bursting cyst-lining epithelial cells (Fig. 3.11 A, B). Single frames of the cyst

initiating event reveal a potential tubule at the base of the cyst that escapes the organoid body and potentially triggers the cyst expansion that rapidly develops afterwards (Fig. 3.11 C).

EMD was able to prevent cyst growth and reduce cyst size in pre-cystic kidney organoids, therefore we assessed how EMD was affecting NMIIB in pre-cystic *PKD1*$^{-/-}$ organoids compared to their isogenic controls. To do this, day 21 pre-cystic NMIIB-GFP-*PKD1*$^{-/-}$ and NMIIB-GFP-*PKD1*$^{+/+}$ organoids were differentiated, treated with 25 μM EMD or DMSO and imaged live for 30 minutes, taking an image every 3 minutes. Analysis of these drug treatment videos revealed that the apical membrane of the kidney tubule had a striking contraction towards its basal tubular side (Fig. 3.12 A). To measure this effect, apical-basal tubular widths were measured before and after 30 minutes of exposure to EMD in both NMIIB-GFP-*PKD1*$^{-/-}$ and NMIIB-GFP-*PKD1*$^{+/+}$ organoids (Fig. 3.12 B). While EMD treatment caused a reduction in tubular width in both the NMIIB-GFP-*PKD1*$^{-/-}$ and NMIIB-GFP-*PKD1*$^{+/+}$ organoids, the NMIIB-GFP-*PKD1*$^{-/-}$ had a significantly stronger contractile response, suggesting that they are in a more contractile-ready state compared to their *PKD1*$^{+/+}$ counterparts (Fig. 3.12 C).

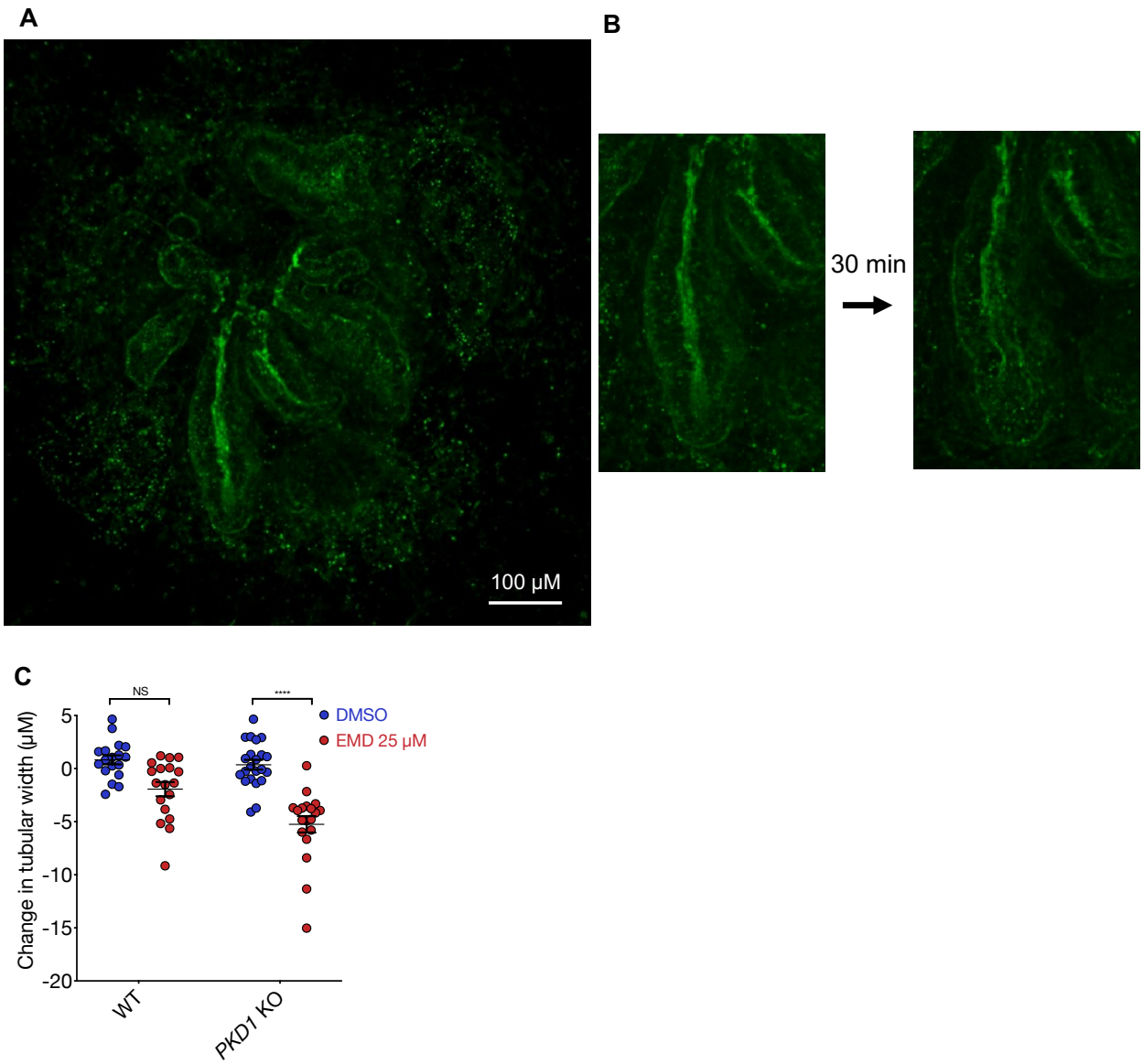

Figure 3.12. EMD contracts apical tubular membrane of kidney organoids.

A. Video of NMIIB-GFP-*PKD1*$^{-/-}$ organoid responding to EMD treatment over 30 minutes. B. Immunofluorescence image of organoid tubule before and after EMD treatment. C. Quantification of tubule width after drug treatment. Dots represent a kidney tubule. Mean ± SEM, n ≥ 3 organoids per treatment from three independent experiments. Two tailed T-test, ns $p > 0.05$, **** $p < 0.0001$.

3.3.4 *Phosphorylated myosin light chain expression coincides with PKD cyst growth and stromal expansion*

Increased presence of renal myofibroblasts is known to emerge and cause matrix deposition and fibrosis in polycystic kidney disease patients, reducing kidney functionality (200). Myofibroblasts are markers of wound healing and have high contractile force which can be advantageous for tissue remodeling but can be a detriment to tissue function (204). Due to myofibroblasts' role in worsening PKD prognosis and their contractile nature, we assessed their presence in both our cystic PKD and non-PKD organoids. Minimal levels of αSMA+ myofibroblasts were observed in non-PKD organoids, however detectable αSMA+ cells surrounding cystic epithelium were detected in our cystic PKD organoids (Fig. 3.13).

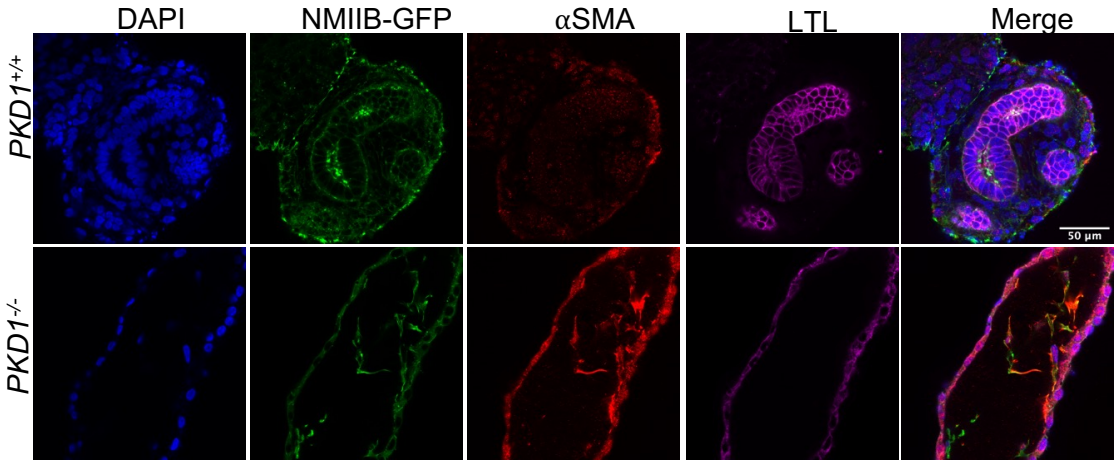

Figure 3.13. αSMA+ myofibroblasts arise primarily in cystic PKD organoids Representative immunofluorescent confocal images of cystic PKD and non-PKD organoids.

Due to EMD's and blebbistatin's opposing effects on myosin contractility, we assessed whether exposure to these drugs effected the presence of αSMA+ myofibroblasts in drug treated PKD organoids. αSMA+ myofibroblasts were present in all treatment conditions, particularly in the

attenuated cystic epithelium of the PKD cysts (Fig. 3.14). No obvious differences in myofibroblast presence were noticed with EMD or blebbistatin treatment.

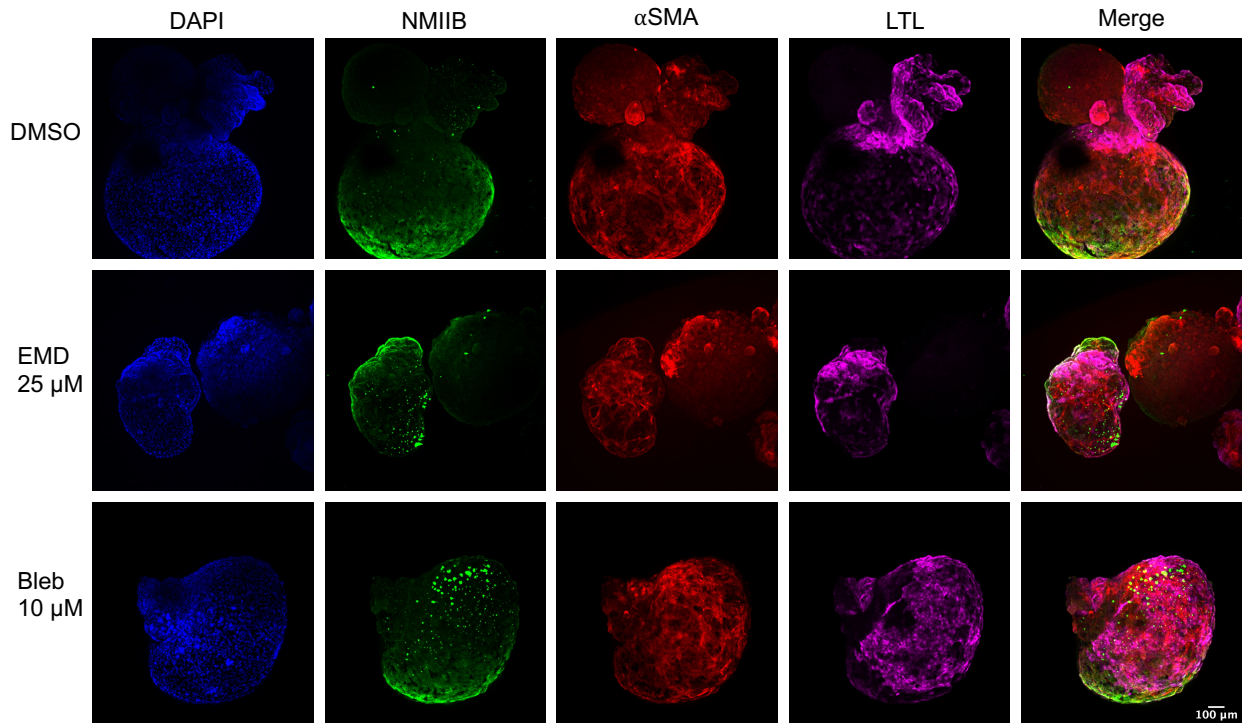

Figure 3.14. Myosin drugs do not have significant influence on αSMA+ myofibroblasts in PKD organoids.

Representative immunofluorescent confocal images of pre-cystic PKD organoids treated with drugs for 2 weeks.

Due to the progression of fibrosis in later stage PKD, we assessed the prominence of αSMA+ myofibroblasts and phosphorylated of myosin light chain 2 (pMLC2), a marker of myosin activation, in a slow progressing mouse model of PKD in which both alleles of *Pkd1* have a hypomorphic mutation orthologous to one found in human patients with mild PKD (177). Interestingly, seven-month-old $Pkd1^{RC/RC}$ mice had heightened levels of both αSMA+ myofibroblasts and pMLC2 expression which colocalized in the cystic kidney cortex stroma but

were minimally present in the age-matched non-cystic *Pkd1*$^{+/+}$ tissue and primarily localized to αSMA+ arterioles and glomeruli (Fig. 3.15).

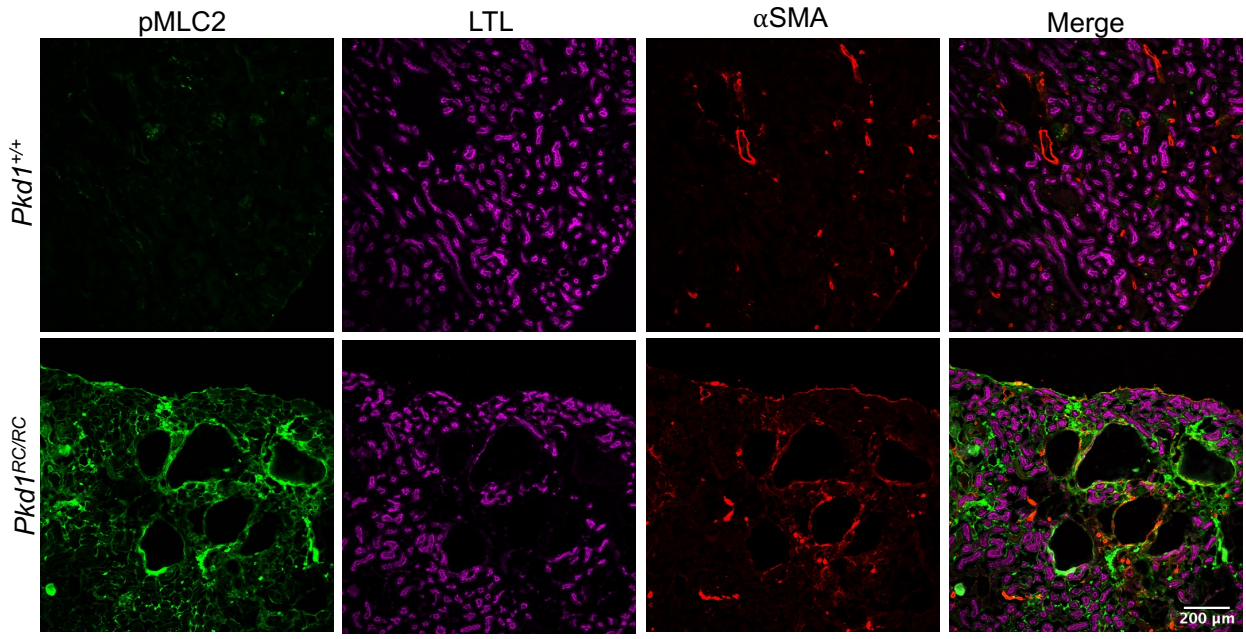

Figure 3.15 pMLC2 and αSMA levels are elevated in cystic compartments of *Pkd1*$^{RC/RC}$ mice.

Representative immunofluorescent images of seven-month-old *Pkd1*$^{RC/RC}$ and *Pkd1*$^{+/+}$ mice kidney cortex.

Due to the *Pkd1*$^{RC/RC}$ mice having a slow cystic progressing phenotype, we assessed whether pMLC2 expression correlated with the myofibroblast precursor pericyte expression and cyst growth by immunofluorescent staining of the pericyte maker, PDGFRß (205). Pericytes were present at all ages of *Pkd1*$^{RC/RC}$ mice but had notably increased expansion at 7 and 15 months where cysts have become prominent (Fig. 3.16). Interestingly, PDGFRß and pMLC2 expression similarly colocalized to the stromal space surrounding the cystic epithelium as seen in the αSMA+ myofibroblasts (Fig. 3.15). Notably, while PDGFRß expression was detectable in 1 month old *Pkd1*$^{RC/RC}$ mice tissue where cysts had not yet developed, pMLC2 expression was almost

undetectable, suggesting MLC2 phosphorylation is potentially triggered by cyst growth and cyst-induced damage, rather than being unique to *Pkd1*$^{RC/RC}$ entirely (Fig. 3.16).

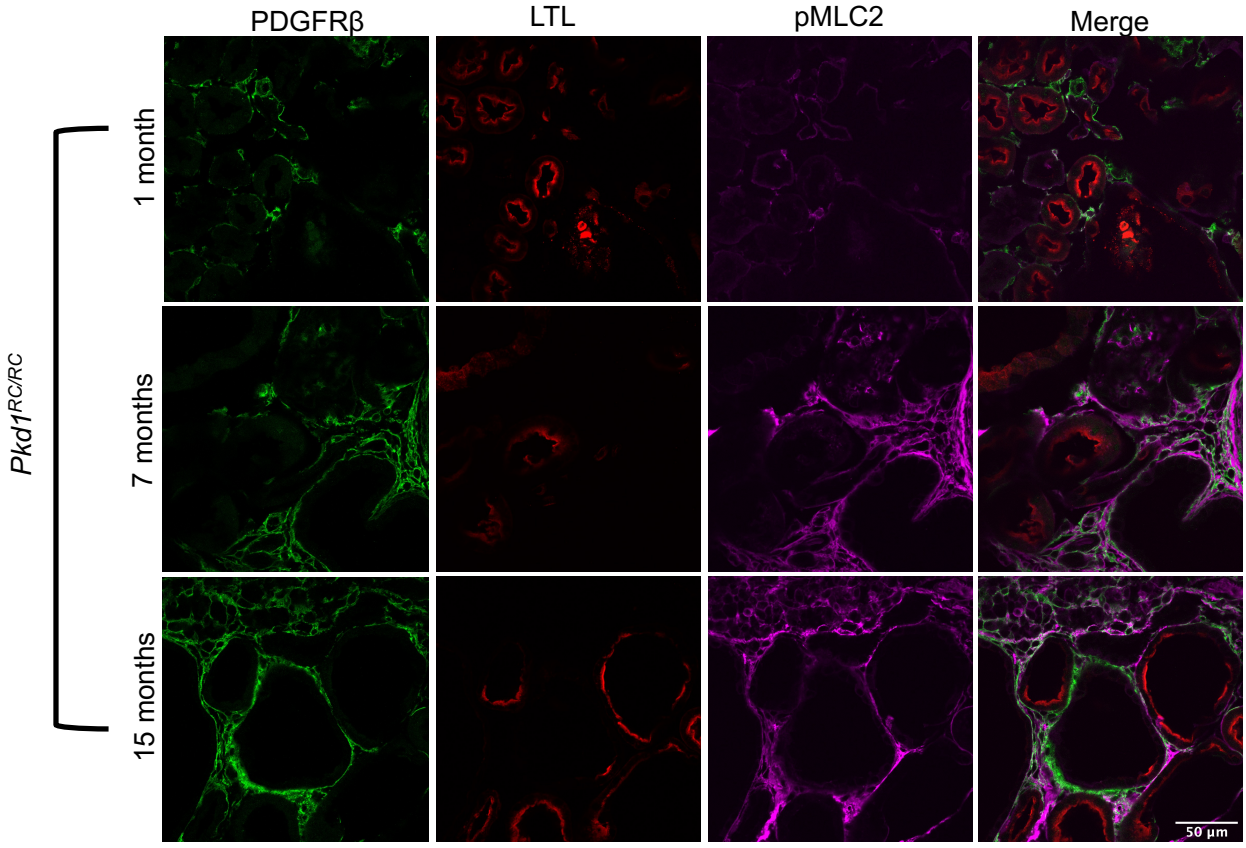

Figure 3.16 Stromal cell expansion correlates with pMLC2 expression and cyst growth. Representative immunofluorescent images of one-, seven-, and fifteen-month-old *Pkd1*$^{RC/RC}$ mice kidney cortex.

To compare whether pericyte expansion and pMLC2 expression also coincide with cyst expansion as observed in the *Pkd1*$^{RC/RC}$ mouse cortex, PKD organoids were differentiated and fixed at both pre- and post-cystic stages and assessed for relative expression and colocalization of both pMLC2 and PDGFRß (Fig. 3.17). Interestingly, both the pre- and post-cystic organoids had negligible levels of pMLC2 expression; the staining that was elicited is primarily background fluorescence. Additionally, expression of PDGFRß+ pericytes in pre-cystic PKD organoids were low and were

undetectable in cystic PKD organoids; the staining that was elicited is also primarily background fluorescence (Fig. 3.17). Together this suggests that the stromal cells in organoids are likely not pericytes, and that relative pMLC2 expression in PKD organoids is low at both pre- and post-cystic stages which differs dramatically compared to the highly expressing pMLC2+ stromal tissues in the *Pkd1*$^{RC/RC}$ mice (Table 3).

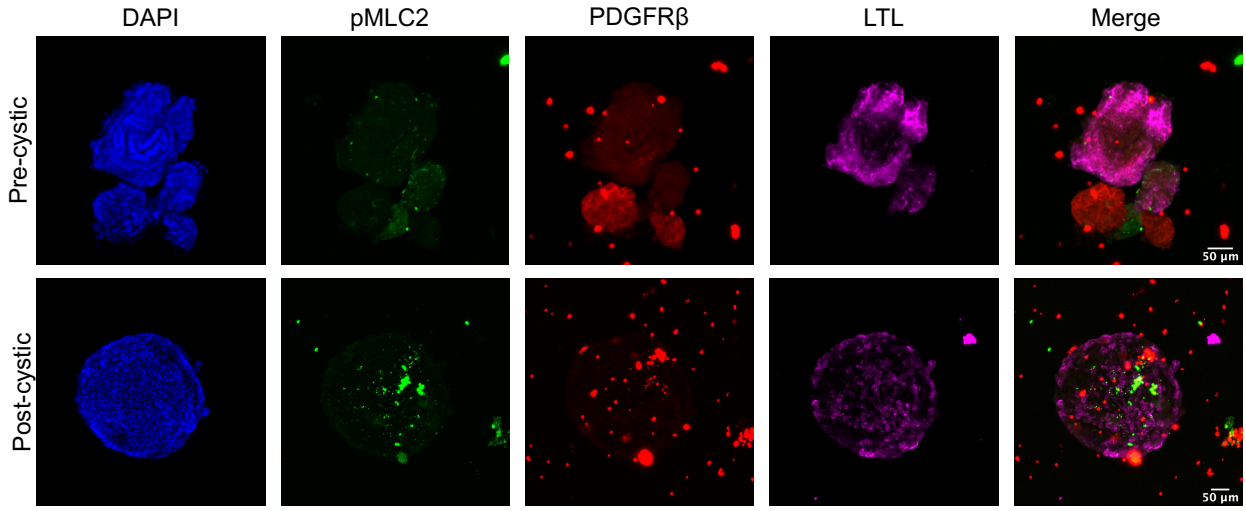

Figure 3.17 Pericyte and pMLC2 expression does not increase due to cyst expansion in PKD organoids.

Representative immunofluorescent images of pre- and post-cystic PKD organoids.

Table 3: Expression of markers in pre- and post-cystic PKD organoids and *Pkd1*$^{RC/RC}$ mice

	Model System	PDGFRβ	αSMA	pMLC2
Pre-cystic	*Organoid*	Minimal	Minimal	Minimal
	Pkd1$^{RC/RC}$ *Mouse*	Low: stromal space	Minimal	Low: stromal small
Post-cystic	*Organoid*	Minimal	High: cystic epithelium and stromal space	Minimal
	Pkd1$^{RC/RC}$ *Mouse*	High: stromal space	High: stromal space	High: stromal space

3.3.5 *EMD shows no significant rescue of cyst growth in Pkd1*$^{RC/RC}$ *mice*

Kidney organoids better recapitulate the phenotypic properties of PKD compared to simple mono-cellular *in vitro* models, but they do not fully capture the complexities of a mammalian kidney. To assess EMD's efficacy at treating PKD in a more complex model, we employed the slow

progressing *Pkd1*$^{RC/RC}$ model that phenocopies human PKD progression (177). *Pkd1*$^{RC/RC}$ mice were aged 6 months and then littermates were intraperitoneally treated with either 10 mg/kg EMD or DMSO 3 times per week for two weeks prior to organ harvesting (Fig. 3.18 A). Mice kidneys were sectioned and stained with Periodic acid-Schiff (PAS) and assessed for significant differences in cyst appearance, of which no visual differences could be observed (Fig. 3.18 B). Further, kidney weight/body weight (KW/BW) ratios reveal that 10 mg/kg EMD treatment had no effect at reducing KW/BW compared to DMSO controls, suggesting that EMD had no ability to rescue the overall cystic burden that contributes to KW (Fig. 3.18 C).

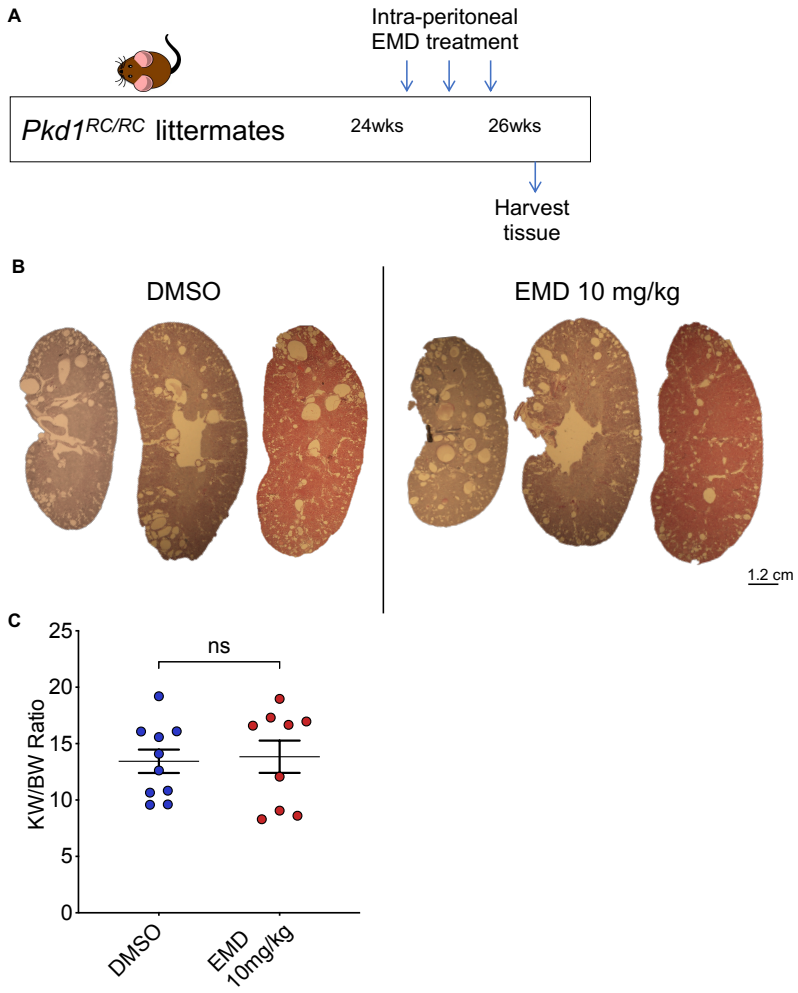

Figure 3.18 Two-week EMD treatment does not rescue cystic phenotype in 6-month-old *Pkd1*$^{RC/RC}$ mice.

A. Schematic of drug dosing of 6-month-old *Pkd1*$^{RC/RC}$ mice. B. Representative images of whole sections of PAS-stained kidneys from DMSO and EMD 10 mg/kg treated *Pkd1*$^{RC/RC}$ mice. C. Quantification of kidney weight/body weight ratio of drug treated *Pkd1*$^{RC/RC}$ mice. Each dot represents 1 mouse. Mean ± SEM, n ≥ 2 mouse per experiment from 3 independent experiments. Unpaired t-test, ns $p > 0.05$.

To assess if EMD was able to slow cystic progression in PKD cysts that are already developed as observed in PKD organoids, we tested the effects of a higher dose of EMD in 12-month-old *Pkd1*$^{RC/RC}$ mice (Fig. 3.19 A). After 2 weeks of intraperitoneal treatment, mice kidneys were

sectioned and stained with PAS and assessed for significant differences in cyst appearance, of which no visual differences could be observed (Fig. 3.19 B). Further, kidney weight/body weight (KW/BW) ratios reveal that 50 mg/kg EMD treatment had no effect at reducing KW/BW compared to DMSO controls, suggesting that EMD had no ability to rescue the overall cystic burden that contributes to KW (Fig. 3.19 C).

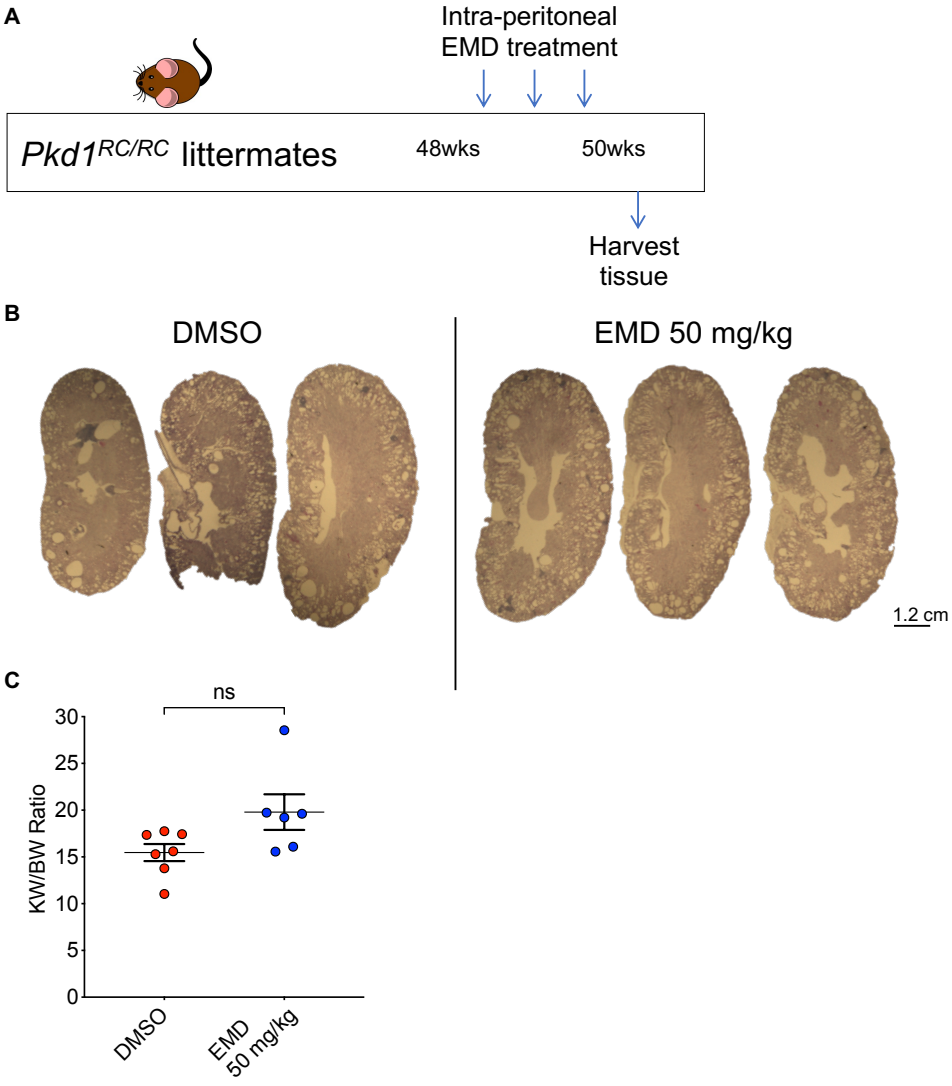

Figure 3.19 Two-week EMD treatment does not rescue cystic phenotype in 12-month-old *Pkd1*$^{RC/RC}$ mice.

A. Schematic of drug dosing of 12-month-old *Pkd1*$^{RC/RC}$ mice. B. Representative images of whole sections of PAS-stained kidneys from DMSO and EMD 50 mg/kg treated *Pkd1*$^{RC/RC}$ mice.

C. Quantification of kidney weight/body weight ratio of drug treated *Pkd1*$^{RC/RC}$ mice. Each dot represents 1 mouse. Mean ± SEM, n = 3-4 mouse per experiment from 2 independent experiments. Unpaired t-test, ns $p > 0.05$.

3.4 DISCUSSION

Myosin has recently been suggested as a targetable pathway to regulate PKD cyst growth, but the exact myosin target and function of myosin in tubules and cysts growth has remained unclear (33, 200). Using both pre- and post-cystic organoids and multiple myosin modulating drugs, we demonstrated that myosin activation via EMD treatment prior to cyst onset rescues cystogenesis in PKD organoids, and post-cystic treatment slows cyst expansion, but does not stop or revert cyst growth. Together, this suggests that myosin activation treatment needs to be timed early when treating PKD cystogenesis to have the strongest preventative effect. Interestingly, combination of 10 μM of EMD and 10 μM of the non-muscle myosin inhibitor blebbistatin significantly reduce cyst progression in PKD organoids better than 10 μM of EMD alone, suggesting a potential synergistic effect of co-treating with both myosin targeting drugs. Considering both EMD and blebbistatin act on the myosin heavy chain ATPase, this may suggest that an optimal amount of ATPase-induced myosin powerstroke activity required to maintain tubule integrity (201, 206).

To further investigate myosin's involvement in PKD, we induced *PKD1* mutations in an endogenously tagged NMIIB-GFP iPSC cell line from the Allen Cell Collection. *MYH10* encodes non-muscle myosin IIB, the most abundant form of two headed myosin in the kidney tubules and is expressed throughout the entirety of both *PKD1*$^{+/+}$ and *PKD1*$^{-/-}$ organoids. NMIIB expression is enriched in the apical membrane of organoid tubules which then gets dispersed as cysts emerge. During live-imaging on pre-cystic NMIIB-GFP-*PKD1*$^{+/+}$ and NMIIB-GFP-*PKD1*$^{-/-}$ organoids,

EMD treatment contracted the apical tubular membrane towards the basal membrane of both organoids, but more significantly in the NMIIB-GFP-*PKD1*$^{-/-}$ organoids. This increased contractile response to EMD in the NMIIB-GFP-*PKD1*$^{-/-}$ organoids suggested that the myosin in the NMIIB-GFP-*PKD1*$^{-/-}$ organoids was poised to contract, but potentially unable to do so on its own (207). Interestingly, both the rho-kinase inhibitor, ROCK, and the myosin light chain kinase inhibitor, ML7, who both prevent phosphorylation of the myosin light chains showed no significant ability to prevent or reduce cyst growth in our pre- or post-cystic PKD organoids, suggesting that targeting the myosin heavy chains with EMD and blebbistatin facilitates the most robust modulation of tubular cystogenesis.

Recent reports have suggested pMLC2 levels are increased in PKD models, but they did not specify where these elevated levels were localized (200). Immunofluorescent staining of our pre- and post-cystic organoids revealed negligible levels of pMLC2 expression. However, pMLC2 expression was abundant in the cystic cortex of 7-month old *Pkd1*$^{RC/RC}$ mice and colocalized with αSMA+ myofibroblasts in the extra-tubular stromal space. In contrast, negligible levels of pMLC2 expression or αSMA+ myofibroblasts were found in the non-cystic cortex of littermate matched 7-month old *Pkd1*$^{+/+}$ mice. Fibrotic depositions caused by matrix secretion from myofibroblasts in response to PKD cyst growth causes irreparable damage and reduce the kidney's ability to function (203). This abundance of pMLC2 in the cystic kidney stroma suggests that stromal cell myosin may be a worthy target of pMLC2 inhibitors to prevent fibrosis, rather than pMLC2 inhibitors treating tubular myosin. However, due to organoids having limited expression of pMLC2, this relationship is better suited for animal model investigation. Recent reports suggest that ROCK inhibitor treatment of *Pkd1*$^{flox/-}$:*KspCre* mice does slightly rescue KW/BW ratios,

however, the fibrotic response in this animal model does not correlate with human PKD due to its rapid inducible cystic onset (200, 208).

To explore whether heightened pMLC2 levels were a signature of *Pkd1*$^{RC/RC}$ mice throughout their cystic growth, a time-course analysis of *Pkd1*$^{RC/RC}$ revealed that pMLC2 levels were minimal at 1 month of age prior to the onset of cyst growth. However, as the mice developed cysts, only then did pMLC2 expression become detectable. Interestingly, pericyte expansion in the stromal space surrounding the cysts correlated and partially co-localized with the pMLC2 expression, suggesting that a population of the pMLC2+ cells are pericytes. Pericytes act as precursors to myofibroblasts in the kidney stroma, both of which are contractile cells involved in the fibrotic damage response pathway (209). This co-localization of both pericytes and myofibroblasts with pMLC2 supports the notion that pMLC2 expression correlates with stromal expansion rather than tubular cyst expansion. Further, pre- and post-cystic organoids stained with pMLC2 and of PDGFRß had undetectable levels of pMLC2 and pericyte presence was minimal in pre-cystic organoids and undetectable in post-cystic organoids, suggesting why we observed no obvious differences in cystogenesis or cyst growth in our ML7 and ROCK treated organoids due to lack of pMLC2+ target. Together, these data suggest that the fibrotic response in PKD is potential targetable by pMLC2 inhibitors. A study comparing *AhCre;Pkd1*$^{flox/flox}$;*Yap*$^{flox/flox}$ mice and *AhCre;Pkd1*$^{flox/flox}$ mice revealed that inducible knockout of yes-associated protein (YAP), of which ROCK is hypothesized to be an upstream activator of YAP, rescues some cyst growth and the KW/BW ratios (199). Interestingly, YAP activation is suggested to facilitate pericyte to myofibroblast transition, and ROCK inhibition can prevent the induction of αSMA+ cells, suggesting a regulatory role of myosin in YAP-induced fibrosis which contributes to late-stage

PKD pathogenesis (210, 211). Further work is required to evaluate the efficacy and specificity of ROCK inhibitors in treating kidney fibrosis.

To assess whether EMD treatment can rescue cyst growth in *Pkd1*$^{RC/RC}$ mice, 7-month old and 12-month old mice were treated with either 10 mg/kg or 50 mg/kg EMD respectively for two weeks. While no significant differences were observed in either their cystic presentation nor their KW/BW ratios, this is likely due to the poor solubility of which EMD is known to have (212). EMD is a calcium sensitizing drug previously developed to treat heart failure, but risks of side effects of phosphodiesterase 3 activation limited its translation to the clinic (201, 213–215). Many PKD patients experience cardiovascular abnormalities, specifically hypertension and left ventricular hypertrophy, suggesting a role of the polycystins in regulating cardiac function as well as kidney tubule stability (216). Interestingly, studies of PC-1 knockout mice exhibit decreased cardiac function and overexpression of a C-terminal fragment of PC-1 was sufficient to trigger neonatal rat ventricular myocyte hypertrophy, suggesting that PC-1 positively regulates cardiac function (217). iPSC derived cardiomyocytes from PKD patients also elicited reduced sarcoplasmic reticulum calcium content and had reduced beating rates (218). These studies suggest the polycystins have a potential positive regulation of cardiac contractile function, yet the relationship to cardiac myosin function has not yet been investigated.

Together, these data support a complex interplay of myosin contraction and phosphorylation that occur during different stages and in different kidney compartments in disease progression. Treating pre-cystic PKD organoids with the myosin activating drug EMD prevents cyst growth, suggesting that PKD tubules have reduced contractile forces that result in cyst emergence (Fig.

3.20 A). After cysts have emerged from PKD tubules, resident pericytes respond to cystic damage with increased levels of pMLC2 and differentiate into myofibroblasts who share these increased levels of pMLC2 expression (Fig. 3.20 B). This work suggests that early-stage myosin activating therapeutics could play a vital role in preventing PKD cystogenesis and that pMLC2 inhibitors may play a role in preventing stromal expansion and fibrotic responses in later stage cystic disease rather than directly modulating tubular cyst growth.

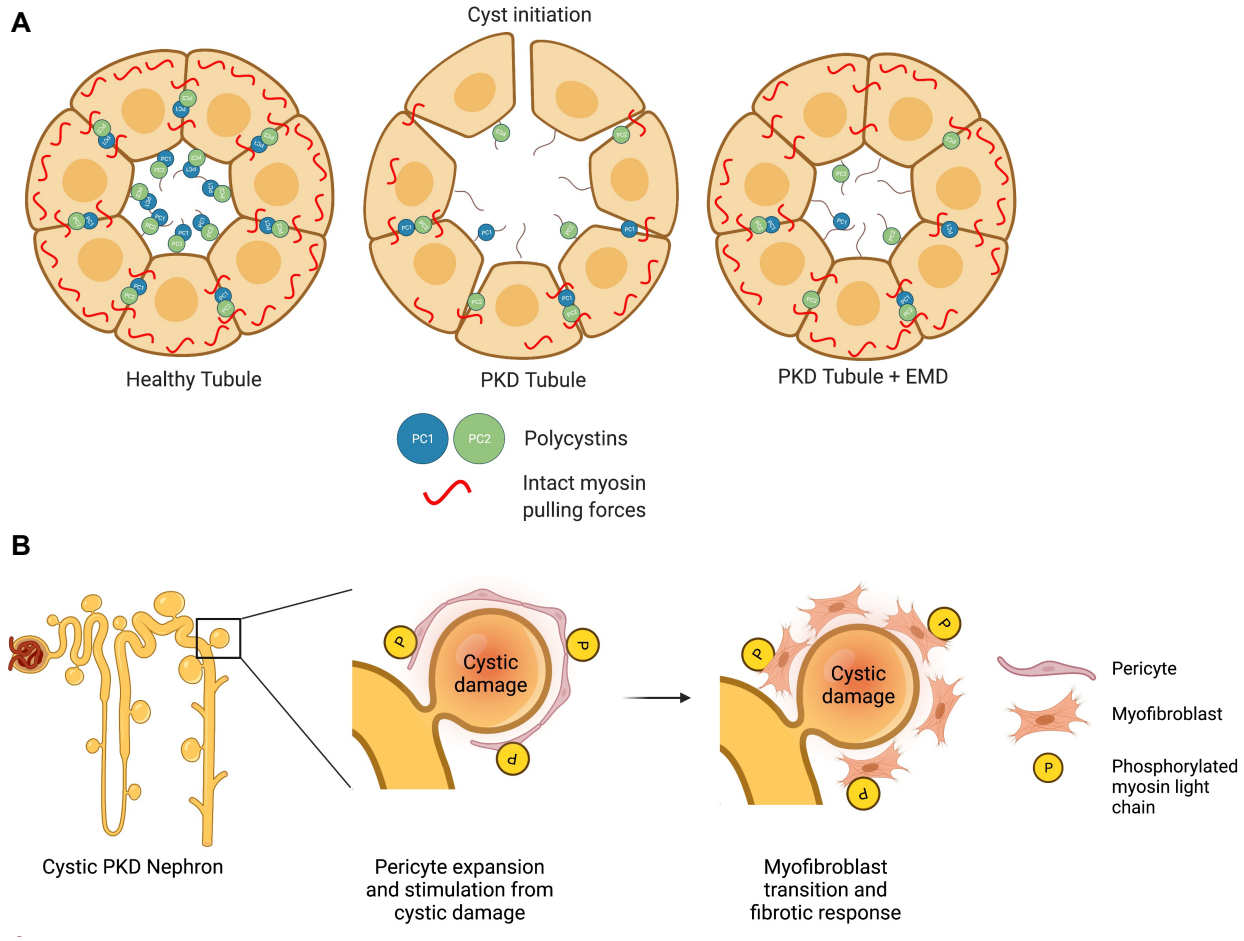

Figure 3.20 Myosin dynamics in PKD cystogenesis and stromal expansion. A. Graphical schematic of myosin pulling forces in healthy, PKD, and EMD treated tubules. B. Graphical schematic of cyst-induced stromal damage response.

Our work and others suggest a functional role of the polycystins in regulating PKD pathogenesis via myosin regulation, however different model systems and organisms produce differential results that require careful comparison (33, 199, 200). The role of myosin in PKD pathogenesis is still in early investigation and the combination of model systems that phenocopy PKD pathogenesis in its entirety are required to facilitate efficacious drug discovery.

Chapter 4. CONCLUSIONS AND FUTURE DIRECTIONS

4.1 Organoid Utility for Infectious Disease Modeling

The emergence of SARS-CoV-2 and the COVID-19 pandemic has been the biggest public health emergency since the 1918 Spanish flu (219). However, the massive difference in 101 years of science between these two pandemics is striking: approximately 10,000 scientific publications are released each month since the onset of COVID-19 and three vaccines have already received FDA approval with considerable efficacy even as new SARS-CoV-2 variants continue to emerge (220, 221). This is amazing. The scientific community's rapid response to the COVID-19 pandemic signifies the major advancements made in our ability to conduct research and translate results into efficacious solutions. However, SARS-CoV-2 appears to be shifting into an endemic phase: variants continue to emerge, vaccine hesitancy persists, and we still do not fully understand all the nuances of SARS-CoV-2's pathogenesis. Therefore, continued study of pathogenic mechanisms is needed to ensure preparedness for the next challenge posed by this virus.

Regarding the kidney, people with CKD are at a higher risk for developing severe COVID-19 as compared to those with chronic heart and lung disease, and patients who were infected with SARS-CoV-2 had higher rates incidence rates of AKI (222). Organoids provide an advantageous platform to study the complex mechanisms of these phenomena. In our work, we demonstrated the direct ability of SARS-CoV-2 to infect the proximal tubular epithelium in which ACE2 expression was required to facilitate viral entry. Using PKD organoids, we showed that SARS-CoV-2 infected cells had apoptotic signatures, suggesting that SARS-CoV-2 can cause direct damage to the kidney via infection. Urine from COVID-19^{+} patients had proteomic signatures of interferon upregulation that were reflected in our infected kidney organoids, supporting the human relevance of using organoid model systems.

Multiple other groups have demonstrated SARS-CoV-2 infection in a multitude of different organoids ranging from capillary, intestinal, lung, colonic, and even intestinal organoids from humans and bats, the hypothesized reservoir of SARS-CoV-2 (80, 82, 223–225). The previous gold standard model system for studying infectious diseases were Vero cells derived from the kidneys of African green monkeys due to their exceptional ability to produce virus. However, experiments performed in Vero cells suggested that hydroxychloroquine could block viral replication when clinical trials demonstrated hydroxychloroquine had no protective effect. Experiments performed in intestinal organoids revealed that hydroxychloroquine had no ability to block viral replication of SARS-CoV-2, validating the utility of organoids to model human responses (226). While organoids have provided valuable insight into our understanding of SARS-CoV-2 pathogenesis, no COVID-19 drugs have directly come from their studies yet despite thousands of drugs being screened in lung organoids, only candidate hits and remdesivir have been

identified (80). However, drug development takes time, and organoids provide significant human complexity and relevance that previous models fail to provide, suggesting that the first organoid-developed drugs will come to market in the near future.

Outside of the COVID-19 pandemic, organoids have shed insight into infectious disease mechanisms that other systems cannot recapitulate. One of the most famous applications is in the discovery that Zika virus only infecting replicating neuronal cells in brain organoids causing the microcephaly observed in developing fetuses (227). Brain organoids have also been used to study other neurotrophic viruses including HIV whereby HIV-infected microglia were added to brain organoids causing neuropathogenesis and inflammatory signatures (228). Human gastric organoids have been employed to study *H. pylori* infection revealing a relationship between the virulence factor Cytoxin-Associated Gene A (CagA) and the tyrosine-protein kinase Met (c-Met) receptor that induces epithelial growth (229). Collectively, organoids have demonstrated exceptional utility in modeling host-virus interactions and shed light into molecular mechanisms of infectious disease pathogenesis. Organoids have demonstrated direct relationships to human pathogenesis that previous model systems failed to predict and are currently being used to predict efficacy of viral therapeutics. While organoids cannot perfectly recapitulate the complexities of human organs yet, the pace of discovery and innovation in this field is bound to improve upon our existing technologies.

4.2 Organoid Utility for Drug Development

The classic drug developmental process has relied upon 2D cell culture models and animal models to predict efficacy and toxicity of therapeutics in humans, resulting in 12 percent of drugs entering

clinical trials to reach approval by the FDA (230). This drug development success rate is extremely low, especially considering it can cost over $2 billion dollars to develop a new drug. 2D cell models have received scrutiny for their inability to recapitulate the complexities of human physiology and have drawn criticism for their predictive power in the drug development process. To overcome this barrier, 3D cell culture models, including organoids, have become increasingly popular for their ability to better recapitulate cellular morphology and tissue structure, responses to stimulation, and drug metabolism (231). Organoids have been a desirable tool for their ability to be patient specific and to mimic *in vivo* complexities and architecture better than spheroids, scaffold model systems, and organ-on-a-chip systems.

While no drugs developed in organoids have yet to reach the market in 2022, the use of organoids to predict drug responses and develop targeted therapeutics has gained traction in the last decade. Kidney organoids grown in 384-well plate format have been used to predict nephrotoxicity in chemotherapeutic agents and identify novel druggable pathways for PKD of which part of this thesis work was based on (33). Our work investigating myosin activators as therapeutics revealed a temporal and compartmental contribution of myosin in PKD cyst growth and the fibrotic response to cyst-induced damage. Using organoids provided a useful tool to study the effects of myosin drugs on PKD cystogenesis and explore myosin as a druggable pathway, but the complementary $Pkd1^{RC/RC}$ mouse model added valuable insight in stromal cell contributions to PKD pathogenesis that the organoids lacked.

Outside of the kidney, genetically engineering colorectal cancer (CRC) organoids harboring a Kirsten Rat Sarcoma Virus (KRAS) mutation were used to screen 2036 FDA-approved compounds

suggesting that bortezomib, currently being used to treat non-small cell lung cancer, was efficacious in CRC organoids (232). Patient-derived tumor organoids retain cell-cell interactions and microenvironmental factors of the sample and patient they are derived from providing an optimal drug screening platform to investigate efficacy of therapeutics. Tumor organoids derived from ovarian cancer samples were used to screen 240 kinase inhibitors, providing results in a week post-biopsy to inform therapeutic decision making (233). Liver organoids with hepatocyte-like features were used to perform high-throughput live imaging screens of 238 marketed pharmaceutical compounds assessing bile acid transport and viability, revealing high levels of sensitivity and specificity for predicting liver toxicity (234). While all these studies aim to evaluate efficacy and toxicity of therapeutics, follow-up studies are required to understand molecular mechanisms involved in the disease the drugs are modifying.

Due to the lack of vasculature, functional connection to other organs, and immature developmental phenotype of stem cell derived human organoids, there remains a reliance upon other model systems to validate drug efficacy prior to testing in humans. While efforts are being made to improve differentiations and organoid modeling, this requires significant work, and will take years to accomplish. In the meantime, organoid studies can help identify efficacious candidates more accurately than basic 2D model systems. Animal models still remain an invaluable tool in assessing off-target effects and whole-animal toxicity responsiveness but may be less relied upon for assessing phenotypic efficacy due to significant species barriers that organoids can bridge.

4.3 Final Remarks

While organoids and kidney organoids specifically, have inherent limitations, they have made major improvements in *in vitro* organ modeling. Multiple companies have emerged employing organoid technology to screen, develop, and discover new therapeutics. Goldfinch Bio, one of the first kidney-focused companies using kidney organoid technology, claim to be developing precision kidney medicine and were valued at $250 million dollars in 2020 with multiple drugs in their pre-clinical pipeline and GFB-887 in a Phase 2 clinical trial for treating focal segmental glomerulosclerosis (Pitchbook). STEMCELL Technologies licensed our differentiation protocol to make a kidney organoid differentiation kit, amongst other organoid options. SEngine Precision Medicine, a local Seattle startup using high-throughput screening of patient-derived tumor organoids to predict and develop cancer-fighting drug, was recently valued at $34 million dollars in 2021 and has developed a Clinical Laboratory Improvement Amendment certification for their solid tumor screen (Pitchbook). Together, these companies demonstrate the translational applicability of organoids from disease modeling to drug development.

The total global market for organoid technologies reached $130 million in 2021 and is expected to experience a 27.3% compound annual growth rate through 2023 (235). This massive growth of the organoid market is driven by the hope that organoids will facilitate more efficacious drugs specific to humans which attracted significant commercial attention and investment. While no organoid companies have produced FDA approved drugs yet, the promise organoids hold remains bright due to the continuous efforts to make more mature, functionally relevant organoid systems to increase the translational applicability of organoids to all facets of research and development.

My graduate research has clearly demonstrated how kidney organoids can be used to elucidate the pathogenesis of infectious diseases in specific organ systems and used to investigate new molecular pathways for drug development to modulate PKD pathogenesis. My work has also revealed the limitations of the organoid model system with which we employed clinical sample and animal model supplementation to fill those gaps. Collectively, these findings demonstrate the valuable role organoids will play in our continuous efforts to study human biology and disease.

BIBLIOGRAPHY

1. Quaggin SE. Clinical Implications of Basic Research Kindling the Kidney. *New England Journal of Medicine* 2016;281–283.
2. Al-Awqati Q, Oliver JA. Stem cells in the kidney. *Kidney International* 2002;61(2):387–395.
3. Hansen J et al. A reference tissue atlas for the human kidney2021;
4. Kalra S, Bandgar T, Sahay M. Renal endocrinology: The new frontier. *Indian Journal of Endocrinology and Metabolism* 2012;16(2):154.
5. Du B et al. Glomerular barrier behaves as an atomically precise bandpass filter in a sub-nanometre regime. *Nature Nanotechnology* 2017;12(11):1096–1102.
6. Ebefors K, Lassén E, Anandakrishnan N, Azeloglu EU, Daehn IS. Modeling the Glomerular Filtration Barrier and Intercellular Crosstalk. *Frontiers in Physiology* 2021;12(June). doi:10.3389/fphys.2021.689083
7. Walker KA, Bertram JF. Kidney development: Core curriculum in Nephrology. *American Journal of Kidney Diseases* 2011;57(6):948–958.
8. Sweeney D, Lindström N, Davies JA. Developmental plasticity and regenerative capacity in the renal ureteric bud/collecting duct system. *Development* 2008;135(15):2505–2510.
9. Brodbeck S, Besenbeck B, Englert C. The transcription factor Six2 activates expression of the Gdnf gene as well as its own promoter. *Mechanisms of Development* 2004;121(10):1211–1222.
10. Little MH, McMahon AP. Mammalian kidney development: Principles, progress, and projections. *Cold Spring Harbor Perspectives in Biology* 2012;4(5):3.
11. Carroll TJ, Park JS, Hayashi S, Majumdar A, McMahon AP. Wnt9b plays a central role in the regulation of mesenchymal to epithelial transitions underlying organogenesis of the mammalian urogenital system. *Developmental Cell* 2005;9(2):283–292.
12. Krause M, Rak-Raszewska A, Pietilä I, Quaggin SE, Vainio S. Signaling during kidney development. *Cells* 2015;4(2):112–132.
13. Edith L. Potter, M.D., PH.D., and Samuel Thierstein MD. Glomerular development in the kidney as an index of fetal maturity. *The Journal of Pediatrics* 1943;22(6):695–706.
14. Haller H, de Groot K, Bahlmann F, Elger M, Fliser D. Stem cells and progenitor cells in renal disease. *Kidney International* 2005;68(5):1932–1936.
15. Cochrane AL et al. Renal structural and functional repair in a mouse model of reversal of ureteral obstruction. *Journal of the American Society of Nephrology* 2005;16(12):3623–3630.
16. Nagaike M et al. Renotropic functions of hepatocyte growth factor in renal regeneration after unilateral nephrectomy. *Journal of Biological Chemistry* 1991;266(34):22781–22784.
17. Rinkevich Y et al. In vivo clonal analysis reveals lineage-restricted progenitor characteristics in mammalian kidney development, maintenance, and regeneration. *Cell Reports* 2014;7(4):1270–1283.
18. López-Novoa JM, Martínez-Salgado C, Rodríguez-Peña AB, Hernández FJL. Common pathophysiological mechanisms of chronic kidney disease: Therapeutic perspectives. *Pharmacology and Therapeutics* 2010;128(1):61–81.
19. Disease CK et al. CKD in the General Population. *USRDS 2021 Annual Data Report* 2018;1–8.
20. Thomson JA. Embryonic stem cell lines derived from human blastocysts. *Science* 1998;282(5391):1145–1147.

21. Takahashi K, Yamanaka S. Induction of Pluripotent Stem Cells from Mouse Embryonic and Adult Fibroblast Cultures by Defined Factors. *Cell* 2006;126(4):663–676.
22. Takahashi K et al. Induction of Pluripotent Stem Cells from Adult Human Fibroblasts by Defined Factors. *Cell* 2007;131(5):861–872.
23. Watanabe K et al. Directed differentiation of telencephalic precursors from embryonic stem cells. *Nature Neuroscience* 2005;8(3):288–296.
24. Keller G, Kennedy M, Papayannopoulou T, Wiles M v. Hematopoietic commitment during embryonic stem cell differentiation in culture. *Molecular and Cellular Biology* 1993;13(1):473–486.
25. Spence JR et al. Directed differentiation of human pluripotent stem cells into intestinal tissue in vitro. *Nature* 2011;470(7332):105–110.
26. Lancaster MA et al. Cerebral organoids model human brain development and microcephaly. *Nature* 2013;501(7467):373–379.
27. Nakano T et al. Self-formation of optic cups and storable stratified neural retina from human ESCs. *Cell Stem Cell* 2012;10(6):771–785.
28. Freedman BS et al. Modelling kidney disease with CRISPR-mutant kidney organoids derived from human pluripotent epiblast spheroids. *Nature Communications* 2015;6(May). doi:10.1038/ncomms9715
29. Kim J, Koo BK, Knoblich JA. Human organoids: model systems for human biology and medicine. *Nature Reviews Molecular Cell Biology* 2020;21(10):571–584.
30. Morizane R et al. Nephron organoids derived from human pluripotent stem cells model kidney development and injury. *Nature Biotechnology* 2015;33(11):1193–1200.
31. Takasato M et al. Kidney organoids from human iPS cells contain multiple lineages and model human nephrogenesis. *Nature* 2015;526(7574):564–568.
32. Wu H et al. Comparative Analysis and Refinement of Human PSC-Derived Kidney Organoid Differentiation with Single-Cell Transcriptomics. *Cell Stem Cell* 2018;23(6):869-881.e8.
33. Czerniecki SM et al. High-Throughput Screening Enhances Kidney Organoid Differentiation from Human Pluripotent Stem Cells and Enables Automated Multidimensional Phenotyping. *Cell Stem Cell* 2018;22(6):929-940.e4.
34. Mae SI et al. Generation of branching ureteric bud tissues from human pluripotent stem cells. *Biochemical and Biophysical Research Communications* 2018;495(1):954–961.
35. Mae SI et al. Expansion of Human iPSC-Derived Ureteric Bud Organoids with Repeated Branching Potential. *Cell Reports* 2020;32(4):107963.
36. Zeng Z et al. Generation of patterned kidney organoids that recapitulate the adult kidney collecting duct system from expandable ureteric bud progenitors. *Nature Communications* 2021;12(1):1–15.
37. Tanigawa S et al. Generation of the organotypic kidney structure by integrating pluripotent stem cell-derived renal stroma.. *Nature communications* 2022;13(1):611.
38. Sato T et al. Single Lgr5 stem cells build crypt-villus structures in vitro without a mesenchymal niche. *Nature* 2009;459(7244):262–265.
39. Drost J, Clevers H. Translational applications of adult stem cell-derived organoids. *Development (Cambridge)* 2017;144(6):968–975.
40. Dvela-Levitt M et al. Small Molecule Targets TMED9 and Promotes Lysosomal Degradation to Reverse Proteinopathy. *Cell* 2019;178(3):521-535.e23.
41. Ameku T et al. Identification of MMP1 as a novel risk factor for intracranial aneurysms in ADPKD using iPSC models. *Scientific Reports* 2016;6(June):1–14.

42. Forbes TA et al. Patient-iPSC-Derived Kidney Organoids Show Functional Validation of a Ciliopathic Renal Phenotype and Reveal Underlying Pathogenetic Mechanisms. *American Journal of Human Genetics* 2018;102(5):816–831.
43. Low JH et al. Generation of Human PSC-Derived Kidney Organoids with Patterned Nephron Segments and a De Novo Vascular Network. *Cell Stem Cell* 2019;25(3):373-387.e9.
44. Fluhr TL et al. Generation of an induced pluripotent stem cell line (DHMCi006-A) from a patient with autosomal recessive polycystic kidney disease (ARPKD) carrying a compound heterozygous missense mutation in the fibrocystin encoding PKHD1 gene. *Stem Cell Research* 2021;57. doi:10.1016/j.scr.2021.102579
45. Liu E et al. Profiling APOL1 Nephropathy Risk Variants in Genome-Edited Kidney Organoids with Single-Cell Transcriptomics . *Kidney360* 2020;1(3):203–215.
46. Hollywood JA et al. Use of Human Induced Pluripotent Stem Cells and Kidney Organoids To Develop a Cysteamine / mTOR Inhibition Combination Therapy for Cystinosis2020;1–21.
47. Homan KA et al. Flow-enhanced vascularization and maturation of kidney organoids in vitro. *Nature Methods* 2019;16(3):255–262.
48. Wilmer MJ et al. Kidney-on-a-Chip Technology for Drug-Induced Nephrotoxicity Screening. *Trends in Biotechnology* 2016;34(2):156–170.
49. Yeung CK, Himmelfarb J. Kidneys on Chips. *Clinical Journal of the American Society of Nephrology* 2019;14(1):144 LP – 146.
50. Yokoo T et al. Human mesenchymal stem cells in rodent whole-embryo culture are reprogrammed to contribute to kidney tissues. *Proceedings of the National Academy of Sciences of the United States of America* 2005;102(9):3296–3300.
51. van den Berg CW et al. Renal Subcapsular Transplantation of PSC-Derived Kidney Organoids Induces Neo-vasculogenesis and Significant Glomerular and Tubular Maturation In Vivo. *Stem Cell Reports* 2018;10(3):751–765.
52. Tajiri S et al. Regenerative potential of induced pluripotent stem cells derived from patients undergoing haemodialysis in kidney regeneration. *Scientific Reports* 2018;8(1):1–12.
53. Bantounas I et al. Generation of Functioning Nephrons by Implanting Human Pluripotent Stem Cell-Derived Kidney Progenitors. *Stem Cell Reports* 2018;10(3):766–779.
54. Nam SA et al. Graft immaturity and safety concerns in transplanted human kidney organoids. *Experimental and Molecular Medicine* 2019;51(11). doi:10.1038/s12276-019-0336-x
55. Porrett PM et al. First clinical-grade porcine kidney xenotransplant using a human decedent model. *American Journal of Transplantation* [published online ahead of print: 2022]; doi:10.1111/ajt.16930
56. Zhang W et al. Kidney Organoids as a Novel Platform to Evaluate Lipopolysaccharide-Induced Oxidative Stress and Apoptosis in Acute Kidney Injury. *Frontiers in Medicine* 2021;8(November):1–11.
57. Wyatt CM, Klotman PE. HIV-associated Nephropathy. *Genetic Diseases of the Kidney* 2009;20(3):793–813.
58. Wysocki J et al. A novel soluble ACE2 variant with prolonged duration of action neutralizes SARS-CoV-2 infection in human kidney organoids. *Journal of the American Society of Nephrology* 2021;32(4):795–803.
59. Omer D et al. Human Kidney Spheroids and Monolayers Provide Insights into SARS-CoV-2 Renal Interactions. *Journal of the American Society of Nephrology* 2021;ASN.2020111546.
60. Menon R et al. SARS-CoV-2 receptor networks in diabetic and COVID-19–associated kidney disease. *Kidney International* 2020;98(6):1502–1518.

61. Helms L et al. Cross-validation of SARS-CoV-2 responses in kidney organoids and clinical populations. *JCI Insight* 2021;6(24). doi:10.1172/jci.insight.154882
62. Zhu N et al. A Novel Coronavirus from Patients with Pneumonia in China, 2019. *New England Journal of Medicine* 2020;382(8):727–733.
63. Rabaan AA et al. SARS-CoV-2, SARS-CoV, and MERS-CoV: A comparative overview. *Infezioni in Medicina* 2020;28(2):174–184.
64. Swai J. Letter to the editor - Mortality rate of acute kidney injury in SARS, MERS, and COVID-19 infection: A systematic review and meta-analysis. *Critical Care* 2020;24(1):1–4.
65. Yeung ML et al. MERS coronavirus induces apoptosis in kidney and lung by upregulating Smad7 and FGF2. *Nature Microbiology* 2016;1(3):1–8.
66. Alsaad KO et al. Histopathology of Middle East respiratory syndrome coronavirus (MERS-CoV) infection – clinicopathological and ultrastructural study. *Histopathology* 2018;72(3):516–524.
67. Diao B et al. Human kidney is a target for novel severe acute respiratory syndrome coronavirus 2 infection. *Nature Communications* 2021;12(1):1–9.
68. Hoffmann M et al. SARS-CoV-2 Cell Entry Depends on ACE2 and TMPRSS2 and Is Blocked by a Clinically Proven Protease Inhibitor. *Cell* 2020;181(2):271-280.e8.
69. Wysocki J, Lores E, Ye M, Soler MJ, Batlle D. Kidney and Lung ACE2 Expression after an ACE Inhibitor or an Ang II Receptor Blocker: Implications for COVID-19. *Journal of the American Society of Nephrology* 2020;31(9):1941–1943.
70. Ye M et al. Glomerular localization and expression of angiotensin-converting enzyme 2 and angiotensin-converting enzyme: Implications for albuminuria in diabetes. *Journal of the American Society of Nephrology* 2006;17(11):3067–3075.
71. Shang J et al. Cell entry mechanisms of SARS-CoV-2. *Proceedings of the National Academy of Sciences of the United States of America* 2020;117(21). doi:10.1073/pnas.2003138117
72. Hamming I et al. Tissue distribution of ACE2 protein, the functional receptor for SARS coronavirus. A first step in understanding SARS pathogenesis. *Journal of Pathology* 2004;203(2):631–637.
73. Braun F et al. SARS-CoV-2 renal tropism associates with acute kidney injury. *The Lancet* 2020;396(10251):597–598.
74. Ramanathan K et al. Histopathology and ultrastructural findings of fatal COVID-19 infections in Washington State: case series2020;(January):19–21.
75. Kral AH, Lambdin BH, Wenger LD, Davidson PJ. Evaluation of an Unsanctioned Safe Consumption Site in the United States. *New England Journal of Medicine* 2020;383(6):589–590.
76. Hanley B et al. Histopathological findings and viral tropism in UK patients with severe fatal COVID-19: a post-mortem study. *The Lancet Microbe* 2020;1(6):e245–e253.
77. Kim JM et al. Original Article Detection and Isolation of SARS-CoV-2 in Serum, Urine, and Stool Specimens of COVID-19 Patients from the Republic of Korea. *Osong Public Health and Research Perspectives* 2020;11(3):112–117.
78. Sun J et al. Isolation of infectious SARS-CoV-2 from urine of a COVID-19 patient. *Emerging Microbes and Infections* 2020;9(1):991–993.
79. Marchiano S et al. SARS-CoV-2 Infects Human Pluripotent Stem Cell-Derived Cardiomyocytes, Impairing Electrical and Mechanical Function. *Stem Cell Reports* 2021;16(3):478–492.
80. Han Y et al. Identification of SARS-CoV-2 inhibitors using lung and colonic organoids. *Nature* 2021;589(7841):270–275.

81. Bermejo JAP et al. SARS-CoV-2 infection of human iPSC derived cardiac cells reflects cytopathic features in hearts of patients with COVID-19. *Science Translational Medicine* 2021;13(590):1–15.
82. Monteil V et al. Inhibition of SARS-CoV-2 Infections in Engineered Human Tissues Using Clinical-Grade Soluble Human ACE2. *Cell* 2020;181(4):905-913.e7.
83. Monteil V et al. Human soluble ACE2 improves the effect of remdesivir in SARS-CoV-2 infection. *EMBO Molecular Medicine* 2021;13(1):1–8.
84. Li M, Izpisua Belmonte JC. Organoids — Preclinical Models of Human Disease. *New England Journal of Medicine* 2019;380(6):569–579.
85. Dinnon KH et al. A mouse-adapted model of SARS-CoV-2 to test COVID-19 countermeasures. *Nature* 2020;586(7830):560–566.
86. Taguchi A et al. Redefining the in vivo origin of metanephric nephron progenitors enables generation of complex kidney structures from pluripotent stem cells. *Cell Stem Cell* 2014;14(1):53–67.
87. Shi P-Y et al. An Infectious cDNA Clone of SARS-CoV-2. *Cell Host and Microbe* 2020;27(May):841–848.
88. Harder JL et al. Organoid single cell profiling identifies a transcriptional signature of glomerular disease. *JCI Insight* 2019;4(1). doi:10.1172/jci.insight.122697
89. Kim YK et al. Gene-Edited Human Kidney Organoids Reveal Mechanisms of Disease in Podocyte Development. *Stem Cells* 2017;35(12):2366–2378.
90. Tanigawa S et al. Organoids from Nephrotic Disease-Derived iPSCs Identify Impaired NEPHRIN Localization and Slit Diaphragm Formation in Kidney Podocytes. *Stem Cell Reports* 2018;11(3):727–740.
91. Cruz NM et al. Organoid cystogenesis reveals a critical role of microenvironment in human polycystic kidney disease. *Nature Materials* 2017;16(11):1112–1119.
92. Bhatraju PK et al. Comparison of host endothelial, epithelial and inflammatory response in ICU patients with and without COVID-19: a prospective observational cohort study. *Critical Care* 2021;25(1):1–12.
93. Rohloff JC et al. Nucleic acid ligands with protein-like side chains: Modified aptamers and their use as diagnostic and therapeutic agents. *Molecular Therapy - Nucleic Acids* 2014;3(October):e201.
94. Williams SA et al. Plasma protein patterns as comprehensive indicators of health. *Nature Medicine* 2019;25(12):1851–1857.
95. Kim CH et al. Stability and reproducibility of proteomic profiles measured with an aptamer-based platform. *Scientific Reports* 2018;8(1):1–10.
96. Candia J et al. Assessment of Variability in the SOMAscan Assay. *Scientific Reports* 2017;7(1):1–13.
97. Cao L et al. De novo design of picomolar SARS-CoV-2 miniprotein inhibitors. *Science* 2020;370(6515):426–431.
98. Merico D, Isserlin R, Stueker O, Emili A, Bader GD. Enrichment map: A network-based method for gene-set enrichment visualization and interpretation. *PLoS ONE* 2010;5(11). doi:10.1371/journal.pone.0013984
99. Gene T, Consortium O. Gene Ontology : tool for the. *Gene Expression* 2000;25(may):25–29.
100. Sun R, Hui S, Bader GD, Lin X, Kraft P. Powerful Gene Set Analysis in GWAS with the Generalized Berk-Jones Statistic. *Powerful gene set analysis in GWAS with the generalized berk-jones statistic* 2018;361436.

101. Gaynor SM, Sun R, Lin X, Quackenbush J. Identification of differentially expressed gene sets using the Generalized Berk-Jones statistic. *Bioinformatics* 2019;35(22):4568–4576.
102. Sun R, Lin X. Genetic Variant Set-Based Tests Using the Generalized Berk–Jones Statistic With Application to a Genome-Wide Association Study of Breast Cancer. *Journal of the American Statistical Association* 2020;115(531):1079–1091.
103. Giroglou T et al. Retroviral Vectors Pseudotyped with Severe Acute Respiratory Syndrome Coronavirus S Protein. *Journal of Virology* 2004;78(17):9007–9015.
104. Henry BM, Lippi G. Chronic kidney disease is associated with severe coronavirus disease 2019 (COVID-19) infection. *International Urology and Nephrology* 2020;52(6):1193–1194.
105. Zhu L et al. Single-Cell Sequencing of Peripheral Mononuclear Cells Reveals Distinct Immune Response Landscapes of COVID-19 and Influenza Patients. *Immunity* 2020;53(3):685-696.e3.
106. Lee JS, Shin EC. The type I interferon response in COVID-19: implications for treatment. *Nature Reviews Immunology* 2020;20(10):585–586.
107. Zhou Z et al. Heightened Innate Immune Responses in the Respiratory Tract of COVID-19 Patients. *Cell Host and Microbe* 2020;27(6):883-890.e2.
108. Sinuani I, Beberashvili I, Averbukh Z, Sandbank J. Role of IL-10 in the progression of kidney disease. *World Journal of Transplantation* 2013;3(4):91.
109. Duffy S. Why are RNA virus mutation rates so damn high?. *PLoS Biology* 2018;16(8):1–6.
110. Plante JA et al. Spike mutation D614G alters SARS-CoV-2 fitness. *Nature* 2021;592(7852):116–121.
111. Lauring AS, Hodcroft EB. Genetic Variants of SARS-CoV-2 - What Do They Mean?. *JAMA - Journal of the American Medical Association* 2021;325(6):529–531.
112. Abdelnabi R et al. Comparing infectivity and virulence of emerging SARS-CoV-2 variants in Syrian hamsters. *EBioMedicine* 2021;68:103403.
113. Panzera Y et al. A deletion in SARS-CoV-2 ORF7 identified in COVID-19 outbreak in Uruguay. *Transboundary and Emerging Diseases* 2021;(December 2020):1–8.
114. Foster CSP, Rawlinson WD. Rapid spread of a SARS-CoV-2 Delta variant with a frameshift deletion in ORF7a. *medRxiv* 2021;(August):2021.08.18.21262089.
115. Feder KA, Pearlowitz M, Goode A, Duwell M, Williams TW. Linked Clusters of SARS-CoV-2 Variant B . 1 . 351 — Maryland , January – February 20212021;70(17):627–631.
116. Firestone MJ et al. First Identified Cases of SARS-CoV-2 Variant P.1 in the United States — Minnesota, January 2021. *MMWR Surveillance Summaries* 2021;70(10):345–346.
117. States U, Galloway SE, Paul P, Maccannell DR, Johansson MA. Emergence of SARS-CoV-2 B . 1 . 1 . 7 Lineage —2021;70(3):95–99.
118. Bedford T et al. Cryptic transmission of SARS-CoV-2 in Washington state. *Science* 2020;370(6516):571–575.
119. Verdecchia P, Cavallini C, Spanevello A, Angeli F. The pivotal link between ACE2 deficiency and SARS-CoV-2 infection. *Elsevier* 2020;(January):14–20.
120. Twomey JD et al. COVID-19 update: The race to therapeutic development. *Drug Resistance Updates* 2020;53(October):100733.
121. Wang Y et al. Remdesivir in adults with severe COVID-19: a randomised, double-blind, placebo-controlled, multicentre trial. *The Lancet* 2020;395(10236):1569–1578.
122. Thakare S et al. Safety of Remdesivir in Patients With Acute Kidney Injury or CKD. *Kidney International Reports* 2021;6(1):206–210.

123. Chouchana, Laurent, Preta, Laure-Helene, Tisseyre, Mylene, Terrier, Benjamin, Treluyer, Jean-Marc, Montastruc F. Kidney disorders as serious adverse drug reactions of remdesivir in coronavirus disease 2019: a retrospective case-noncase study2020;(January).
124. Adamsick ML et al. Remdesivir in patients with acute or chronic kidney disease and COVID-19. *Journal of the American Society of Nephrology* 2020;31(7):1384–1386.
125. Repurposed Antiviral Drugs for Covid-19 — Interim WHO Solidarity Trial Results. *New England Journal of Medicine* 2021;384(6):497–511.
126. Barratt-Due A et al. Evaluation of the Effects of Remdesivir and Hydroxychloroquine on Viral Clearance in COVID-19. *Annals of Internal Medicine* [published online ahead of print: 2021]; doi:10.7326/m21-0653
127. Case JB et al. Ultrapotent miniproteins targeting the SARS-CoV-2 receptor-binding domain protect against infection and disease. *Cell Host and Microbe* 2021;29(7):1151-1161.e5.
128. Howden SE et al. Plasticity of distal nephron epithelia from human kidney organoids enables the induction of ureteric tip and stalk. *Cell Stem Cell* 2021;28(4):671-684.e6.
129. Cui X, Gallini JW, Jasien CL, Mrug M. Autosomal Dominant Polycystic Kidney Disease does not significantly alter major COVID-19 outcomes among veterans. *Kidney360* 2021;2:10.34067/KID.0007282020.
130. Xu J et al. SARS-CoV-2 induces transcriptional signatures in human lung epithelial cells that promote lung fibrosis. *Respiratory Research* 2020;21(1):1–12.
131. Zhang M et al. Biomimetic Human Disease Model of SARS-CoV-2-Induced Lung Injury and Immune Responses on Organ Chip System. *Advanced Science* 2021;8(3):1–14.
132. Chilosi M et al. The pathogenic role of epithelial and endothelial cells in early-phase COVID-19 pneumonia: victims and partners in crime. *Modern Pathology* [published online ahead of print: 2021]; doi:10.1038/s41379-021-00808-8
133. Lazzeri E et al. Endocycle-related tubular cell hypertrophy and progenitor proliferation recover renal function after acute kidney injury. *Nature Communications* 2018;9(1):1–18.
134. Järhult JD, Hultström M, Bergqvist A, Frithiof R, Lipcsey M. The impact of viremia on organ failure, biomarkers and mortality in a Swedish cohort of critically ill COVID-19 patients. *Scientific Reports* 2021;11(1):1–8.
135. Li Y et al. SARS-CoV-2 viremia is associated with distinct proteomic pathways and predicts COVID-19 outcomes. *Journal of Clinical Investigation* 2021;131(13). doi:10.1172/JCI148635
136. Myhre PL, Prebensen C, Jonassen CM, Berdal JE, Omland T. SARS-CoV-2 viremia is associated with inflammatory, but not cardiovascular biomarkers, in patients hospitalized for COVID-19. *Journal of the American Heart Association* 2021;10(9):1–5.
137. Shetty AA et al. COVID-19-associated glomerular disease. *Journal of the American Society of Nephrology* 2021;32(1):33–40.
138. Kissling S et al. Collapsing glomerulopathy in a COVID-19 patient. *Kidney International* 2020;98(1):228–231.
139. Reich HN, Oudit GY, Penninger JM, Scholey JW, Herzenberg AM. Decreased glomerular and tubular expression of ACE2 in patients with type 2 diabetes and kidney disease. *Kidney International* 2008;74(12):1610–1616.
140. Beckerman P et al. Transgenic expression of human APOL1 risk variants in podocytes induces kidney disease in mice. *Nature Medicine* 2017;23(4):429–438.
141. Aghajan M et al. Antisense oligonucleotide treatment ameliorates IFN-γ-induced proteinuria in APOL1-transgenic mice. *JCI Insight* 2019;4(12):0–19.

142. Nichols B et al. Innate immunity pathways regulate the nephropathy gene Apolipoprotein L1. *Kidney International* 2015;87(2):332–342.
143. EMA. Summary on compassionate use Remdesivir Gilead International Nonproprietary Name : remdesivir. *European Medicines Agency* 2020;31(April):41.
144. Tempestilli M et al. Pharmacokinetics of remdesivir and GS-441524 in two critically ill patients who recovered from COVID-19. *Journal of Antimicrobial Chemotherapy* 2020;75(10):2977–2980.
145. Hunt AC et al. Multivalent designed proteins protect against SARS-CoV-2 variants of concern. *bioRxiv* 2021;2021.07.07.451375.
146. Rodrigues C. Clinical Infectious Diseases Society Clinical Infectious Diseases Society. *Clinical Infectious Diseases* 2021;2–3.
147. Khan A et al. Higher infectivity of the SARS-CoV-2 new variants is associated with K417N/T, E484K, and N501Y mutants: An insight from structural data. *Journal of Cellular Physiology* 2021;(March):1–13.
148. Cheng MH, Krieger JM, Kaynak B, Arditi M, Bahar I. Impact of South African 501.V2 variant on SARS-CoV-2 spike infectivity and neutralization: A structure-based computational assessment. *bioRxiv* [published online ahead of print: 2021]; doi:10.1101/2021.01.10.426143
149. Redondo N, Zaldívar-López S, Garrido JJ, Montoya M. SARS-CoV-2 Accessory Proteins in Viral Pathogenesis: Knowns and Unknowns. *Frontiers in Immunology* 2021;12(December 2019):1–8.
150. Sims AC et al. Severe Acute Respiratory Syndrome Coronavirus Infection of Human Ciliated Airway Epithelia: Role of Ciliated Cells in Viral Spread in the Conducting Airways of the Lungs. *Journal of Virology* 2005;79(24):15511–15524.
151. Charytan DM et al. Decreasing Incidence of Acute Kidney Injury in Patients with COVID-19 Critical Illness in New York City. *Kidney International Reports* 2021;6(4):916–927.
152. Smith KD, Akilesh S. Pathogenesis of coronavirus disease 2019-associated kidney injury. *Current opinion in nephrology and hypertension* 2021;30(3):324–331.
153. Chapin HC, Caplan MJ. The cell biology of polycystic kidney disease. *Journal of Cell Biology* 2010;191(4):701–710.
154. Budhram B et al. End-Stage Kidney Disease in Patients With Autosomal Dominant Polycystic Kidney Disease: A 12-Year Study Based on the Canadian Organ Replacement Registry. *Canadian Journal of Kidney Health and Disease* 2018;5. doi:10.1177/2054358118778568
155. Hughes J et al. The polycystic kidney disease 1 (PKD1) gene encodes a novel protein with multiple cell recognition domains1995;10(june).
156. Hogan MC et al. Identification of biomarkers for PKD1 using urinary exosomes. *Journal of the American Society of Nephrology* 2015;26(7):1661–1670.
157. Ibraghimov-Beskrovnaya O et al. Polycystin: In vitro synthesis, in vivo tissue expression, and subcellular localization identifies a large membrane-associated protein. *Proceedings of the National Academy of Sciences of the United States of America* 1997;94(12):6397–6402.
158. Tsiokas L et al. Specific association of the gene product of PKD2 with the TRPC1 channel. *Proceedings of the National Academy of Sciences of the United States of America* 1999;96(7):3934–3939.
159. Qian Q et al. Pkd2 haploinsufficiency alters intracellular calcium regulation in vascular smooth muscle cells. *Human Molecular Genetics* 2003;12(15):1875–1880.

160. Mohammed SG et al. Primary cilia–regulated transcriptome in the renal collecting duct. *FASEB Journal* 2018;32(7):3653–3668.
161. Ma M, Tian X, Igarashi P, Pazour GJ, Somlo S. Loss of cilia suppresses cyst growth in genetic models of autosomal dominant polycystic kidney disease. *Nature Genetics* 2013;45(9):1004–1012.
162. Dong K et al. Renal plasticity revealed through reversal of polycystic kidney disease in mice. *Nature Genetics* 2021;53(12):1649–1663.
163. Jinek M et al. A Programmable Dual-RNA – Guided DNA Endonuclease in Adaptive Bacterial Immunity. *Science* 2012;337(August):816–822.
164. Grantham JJ et al. Chemical modification of cell proliferation and fluid secretion in renal cysts. *Kidney International* 1989;35(6):1379–1389.
165. Roberto Mangoo-Karim, Marie E. Uchic, Michael Grant, Wendy A. Shumate, James P. Calvet, Chan H. Park JJG. Renal epithelial fluid secretion and cyst growth: the role of cyclic AMP. *The Federation of American Societies of Experimental Biology* 1989;3(14):2629–2632.
166. Silva LM et al. Inhibition of Hedgehog signaling suppresses proliferation and microcyst formation of human Autosomal Dominant Polycystic Kidney Disease cells. *Scientific Reports* 2018;8(1):1–12.
167. Wilson PD et al. Reversed polarity of Na+-K+-ATPase: Mislocation to apical plasma membranes in polycystic kidney disease epithelia. *American Journal of Physiology - Renal Fluid and Electrolyte Physiology* 1991;260(3 29-3):420–430.
168. Idowu J et al. Aberrant Regulation of Notch3 Signaling Pathway in Polycystic Kidney Disease. *Scientific Reports* 2018;8(1):1–12.
169. Grant E et al. Arginine Vasopressin Stimulates Net Fluid Secretion in a Polarized Subculture of Cyst-Forming MDCK Cells. *Journal of the American Society of Nephrology : JASN* 1991;219–227.
170. Grant M et al. Cyst Fluid From Human Autosomal Dominant Polycystic Kidneys Promotes Cyst Formation and Expansion by Renal Epithelial Cells In Vitro. *The Journal of the American Society of Nephrology* 1992;3(4).
171. Kuo IY et al. Cyst formation following disruption of intracellular calcium signaling. *Proceedings of the National Academy of Sciences of the United States of America* 2014;111(39):14283–14288.
172. Romero-Guevara R, Ioannides A, Xinaris C. Kidney Organoids as Disease Models: Strengths, Weaknesses and Perspectives. *Frontiers in Physiology* 2020;11(November):1–10.
173. Boulter C et al. Cardiovascular, skeletal, and renal defects in mice with a targeted disruption of the Pkd1 gene. *Proceedings of the National Academy of Sciences of the United States of America* 2001;98(21):12174–12179.
174. Wu G et al. Cardiac defects and renal failure in mice with targeted mutations in Pkd2. *Nature Genetics* 2000;24(1):75–78.
175. Pennekamp P et al. The ion channel polycystin-2 is required for left-right axis determination in mice. *Current Biology* 2002;12(11):938–943.
176. Piontek K, Menezes LF, Garcia-Gonzalez MA, Huso DL, Germino GG. A critical developmental switch defines the kinetics of kidney cyst formation after loss of Pkd1. *Nature Medicine* 2007;13(12):1490–1495.
177. Rossetti S et al. Incompletely penetrant PKD1 alleles suggest a role for gene dosage in cyst initiation in polycystic kidney disease. *Kidney International* 2009;75(8):1–14.

178. Katharina Hopp, Christopher J. Ward, Cynthia J. Hommerding, Samih H. Nasr, Han-Fang Tuan, Vladimir G. Gainullin, Sandro Rossetti, Vicente E. Torres and PCH. Functional polycystin-1 dosage governs autosomal dominant polycystic kidney disease severity. *The Journal of Clinical Investigation* 2012;122(11):55–59.
179. Torres VE et al. Effective treatment of an orthologous model of autosomal dominant polycystic kidney disease. *Nature Medicine* 2004;10(4):363–364.
180. Wang X, Gattone V, Harris PC, Torres VE. Effectiveness of vasopressin V2 receptor antagonists OPC-31260 and OPC-41061 on polycystic kidney disease development in the PCK rat. *Journal of the American Society of Nephrology* 2005;16(4):846–851.
181. Wang X, Wu Y, Ward CJ, Harris PC, Torres VE. Vasopressin directly regulates cyst growth in polycystic kidney disease. *Journal of the American Society of Nephrology* 2008;19(1):102–108.
182. Torres VE et al. Tolvaptan in Patients with Autosomal Dominant Polycystic Kidney Disease. *New England Journal of Medicine* 2012;367(25):2407–2418.
183. Ravichandran K, Zafar I, Ozkok A, Edelstein CL. An mTOR kinase inhibitor slows disease progression in a rat model of polycystic kidney disease. *Nephrology Dialysis Transplantation* 2015;30(1):45–53.
184. Shillingford JM et al. The mTOR pathway is regulated by polycystin-1, and its inhibition reverses renal cystogenesis in polycystic kidney disease. *Proceedings of the National Academy of Sciences of the United States of America* 2006;103(14):5466–5471.
185. Watnick T, Germino GG. mTOR Inhibitors in Polycystic Kidney Disease. *New England Journal of Medicine* 2010;363(9):879–881.
186. Serra AL et al. Sirolimus and Kidney Growth in Autosomal Dominant Polycystic Kidney Disease. *New England Journal of Medicine* 2010;363(9):820–829.
187. Masyuk T v., Masyuk AI, Torres VE, Harris PC, Larusso NF. Octreotide Inhibits Hepatic Cystogenesis in a Rodent Model of Polycystic Liver Disease by Reducing Cholangiocyte Adenosine 3′,5′-Cyclic Monophosphate. *Gastroenterology* 2007;132(3):1104–1116.
188. Lin C, Happé H, Veraar K, Scharpfenecker M, Peters DJM. The expression of somatostatin receptor 2 decreases during cyst growth in mice with polycystic kidney disease. *Experimental Biology and Medicine* 2018;243(13):1092–1098.
189. Caroli A et al. Effect of longacting somatostatin analogue on kidney and cyst growth in autosomal dominant polycystic kidney disease (ALADIN): A randomised, placebo-controlled, multicentre trial. *The Lancet* 2013;382(9903):1485–1495.
190. Meijer E et al. Effect of lanreotide on kidney function in patients with autosomal dominant polycystic kidney disease the DIPAK 1 randomized clinical trial. *JAMA - Journal of the American Medical Association* 2018;320(19):2010–2019.
191. Gevers TJG et al. Effect of lanreotide on polycystic liver and kidneys in autosomal dominant polycystic kidney disease: An observational trial. *Liver International* 2015;35(5):1607–1614.
192. Sweeney WE, Frost P, Avner ED. Tesevatinib ameliorates progression of polycystic kidney disease in rodent models of autosomal recessive polycystic kidney disease. *World Journal of Nephrology* 2017;6(4):188.
193. Betapudi V. Life without double-headed non-muscle myosin II motor proteins. *Frontiers in Chemistry* 2014;2(July):1–13.
194. Menon R et al. Single cell transcriptomics identifies focal segmental glomerulosclerosis remission endothelial biomarker. *JCI Insight* 2020;5(6):1–21.

195. Vicente-Manzanares M, Ma X, Adelstein RS, Horwitz AR. Non-muscle myosin II takes centre stage in cell adhesion and migration. *Nature Reviews Molecular Cell Biology* 2009;10(11):778–790.
196. Recuenco MC et al. Nonmuscle Myosin II Regulates the Morphogenesis of Metanephric Mesenchyme–Derived Immature Nephrons. *Journal of the American Society of Nephrology* 2015;26(5):1081–1091.
197. Haque F et al. Non-muscle myosin II deletion in the developing kidney causes ureter-bladder misconnection and apical extrusion of the nephric duct lineage epithelia. *Developmental Biology* 2017;427(1):121–130.
198. Doerr N et al. Regulation of polycystin-1 function by calmodulin binding. *PLoS ONE* 2016;11(8):1–21.
199. Cai J et al. A RhoA–YAP–c-Myc signaling axis promotes the development of polycystic kidney disease. *Genes and Development* 2018;32(11–12):781–793.
200. Nigro EA et al. Polycystin-1 Regulates Actomyosin Contraction and the Cellular Response to Extracellular Stiffness. *Scientific Reports* 2019;9(1):16640.
201. Radke MB et al. Small molecule-mediated refolding and activation of myosin motor function. *eLife* 2014;3. doi:10.7554/eLife.01603
202. Roberts B et al. Systematic gene tagging using CRISPR/Cas9 in human stem cells to illuminate cell organization. *Molecular Biology of the Cell* 2017;28(21):2854–2874.
203. Cheng Jack Song, Kurt A. Zimmerman, Scott J. Henke BKY. Inflammation and Fibrosis in Polycystic Kidney Disease. *Physiology & behavior* 2016;176(1):139–148.
204. Hinz B. Formation and function of the myofibroblast during tissue repair. *Journal of Investigative Dermatology* 2007;127(3):526–537.
205. Chen YT et al. Platelet-derived growth factor receptor signaling activates pericyte-myofibroblast transition in obstructive and post-ischemic kidney fibrosis. *Kidney International* 2011;80(11):1170–1181.
206. Zhang M, Rao PV. Blebbistatin, a novel inhibitor of myosin II ATPase activity, increases aqueous humor outflow facility in perfused enucleated porcine eyes. *Investigative Ophthalmology and Visual Science* 2005;46(11):4130–4138.
207. Newell-Litwa KA, Horwitz R, Lamers ML. Non-muscle myosin II in disease: mechanisms and therapeutic opportunities. *Disease Models & Mechanisms* 2015;8(12):1495–1515.
208. Podrini C et al. Dissection of metabolic reprogramming in polycystic kidney disease reveals coordinated rewiring of bioenergetic pathways. *Communications Biology* 2018;1(1). doi:10.1038/s42003-018-0200-x
209. Chang FC, Chou YH, Chen YT, Lin SL. Novel insights into pericyte-myofibroblast transition and therapeutic targets in renal fibrosis. *Journal of the Formosan Medical Association* 2012;111(11):589–598.
210. Feng F, Feng X, Zhang D, Li Q, Yao L. Matrix Stiffness Induces Pericyte-Fibroblast Transition Through YAP Activation. *Frontiers in Pharmacology* 2021;12(May):1–12.
211. Liu Z et al. RhoA/ROCK-YAP/TAZ Axis Regulates the Fibrotic Activity in Dexamethasone-Treated Human Trabecular Meshwork Cells. *Frontiers in Molecular Biosciences* 2021;8(September):1–14.
212. Schamp K, Schreder SA, Dressman J. Development of an in vitro/in vivo correlation for lipid formulations of EMD 50733, a poorly soluble, lipophilic drug substance. *European Journal of Pharmaceutics and Biopharmaceutics* 2006;62(3):227–234.

213. Haeusler, Guenther; Jonas, Rochus; Minck, Karl-Otto; Schliep, Hans-Jochen; Schelling, Pierre; Weygandt, Heinrich; Lues I. In Vivo Evidence of Positive Inotropism of EMD 57 033 Through Calcium Sensitization. *Journal of Cardiovascular Pharmacology* 1997;29(5):647–655.
214. Senzaki H et al. Improved mechanoenergetics and cardiac rest and reserve function of in vivo failing heart by calcium sensitizer EMD-57033. *Circulation* 2000;101(9):1040–1048.
215. Rodriguez AG, Rodriguez ML, Han SJ, Sniadecki NJ, Regnier M. Enhanced contractility with 2-deoxy-ATP and EMD 57033 is correlated with reduced myofibril structure and twitch power in neonatal cardiomyocytes. *Integrative Biology (United Kingdom)* 2013;5(11):1366–1373.
216. Ecder T, Schrier RW. Cardiovascular abnormalities in autosomal-dominant polycystic kidney disease. *Nature Reviews Nephrology* 2009;5(4):221–228.
217. Pedrozo Z et al. Polycystin-1 is a cardiomyocyte mechanosensor that governs L-type Ca2+ channel protein stability. *Circulation* 2015;131(24):2131–2142.
218. Lee JJ et al. Primary cardiac manifestation of autosomal dominant polycystic kidney disease revealed by patient induced pluripotent stem cell-derived cardiomyocytes. *EBioMedicine* 2019;40:675–684.
219. Morens DM, Taubenberger JK, Fauci AS. A centenary tale of two pandemics: The 1918 influenza pandemic and COVID-19, Part I. *American Journal of Public Health* 2021;111(6):1086–1094.
220. Chen Q, Allot A, Lu Z. LitCovid: An open database of COVID-19 literature. *Nucleic Acids Research* 2021;49(D1):D1534–D1540.
221. Vasireddy D, Atluri P, Malayala SV, Vanaparthy R, Mohan G. Review of COVID-19 Vaccines Approved in the United States of America for Emergency Use. *Journal of Clinical Medicine Research* 2021;13(4):204–213.
222. Gansevoort RT, Hilbrands LB. CKD is a key risk factor for COVID-19 mortality. *Nature Reviews Nephrology* 2020;16(12):705–706.
223. Zhou P et al. A pneumonia outbreak associated with a new coronavirus of probable bat origin. *Nature* 2020;579(7798):270–273.
224. Zhou J et al. Infection of bat and human intestinal organoids by SARS-CoV-2. *Nature Medicine* 2020;26(7):1077–1083.
225. Lamers MM et al. SARS-CoV-2 productively infects human gut enterocytes. *Science* 2020;369(6499):50–54.
226. Beumer J et al. A CRISPR/Cas9 genetically engineered organoid biobank reveals essential host factors for coronaviruses. *Nature Communications* 2021;12(1). doi:10.1038/s41467-021-25729-7
227. Garcez PP et al. Zika virus impairs growth in human neurospheres and brain organoids. *Science* 2016;352(6287):816–818.
228. dos Reis RS, Sant S, Keeney H, Wagner MCE, Ayyavoo V. Modeling HIV-1 neuropathogenesis using three-dimensional human brain organoids (hBORGs) with HIV-1 infected microglia. *Scientific Reports* 2020;10(1):1–17.
229. McCracken KW et al. Modelling human development and disease in pluripotent stem-cell-derived gastric organoids. *Nature* 2014;516(7531):400–404.
230. Austin D, Hayford T. Development in the Pharmaceutical Industry At a Glance2021;
231. Anton D, Burckel H, Josset E, Noel G. Three-dimensional cell culture: A breakthrough in vivo. *International Journal of Molecular Sciences* 2015;16(3):5517–5527.

232. Du Y et al. Development of a miniaturized 3D organoid culture platform for ultra-high-throughput screening. *Journal of Molecular Cell Biology* 2020;12(8):630–643.
233. Phan N et al. A simple high-throughput approach identifies actionable drug sensitivities in patient-derived tumor organoids. *Communications Biology* 2019;2(1):1–11.
234. Shinozawa T et al. High-Fidelity Drug-Induced Liver Injury Screen Using Human Pluripotent Stem Cell-Derived Organoids. *Gastroenterology* 2021;160(3):831–846.
235. Market O. Organoids Market Breakdown by Technology. *BCC Research* 2019;89–110.

APPENDIX A

FIGURE 1.1 RIGHTS TO USE

ELSEVIER LICENSE
TERMS AND CONDITIONS
Feb 08, 2022

This Agreement between University of Washington -- Louisa Helms ("You") and Elsevier ("Elsevier") consists of your license details and the terms and conditions provided by Elsevier and Copyright Clearance Center.

License Number	5244390218794
License date	Feb 08, 2022
Licensed Content Publisher	Elsevier
Licensed Content Publication	American Journal of Kidney Diseases
Licensed Content Title	Kidney Development: Core Curriculum 2011
Licensed Content Author	Kenneth A. Walker,John F. Bertram
Licensed Content Date	Jun 1, 2011
Licensed Content Volume	57
Licensed Content Issue	6
Licensed Content Pages	11
Start Page	948
End Page	958
Type of Use	reuse in a thesis/dissertation
Portion	figures/tables/illustrations
Number of figures/tables/illustrations	1
Format	both print and electronic
Are you the author of this Elsevier article?	No
Will you be translating?	No

Title	Kidney organoid utility for dynamic disease modeling and drug development
Institution name	University of Washington
Expected presentation date	Mar 2022
Portions	Figure 1 in Kidney Development
Requestor Location	University of Washington 850 Republican Street SEATTLE, WA 98109 United States Attn: University of Washington
Publisher Tax ID	98-0397604
Total	0.00 USD

VITA

Louisa Marie Helms, formerly Pendergast, grew up in Snohomish, Washington and was inspired to pursue science from her high school teacher, Tami Caraballo. Louisa went on to pursue a Bachelor's degree in biological sciences at Carnegie Mellon where she interned at the Mellon College of Science, Immunetrics, and The Institute for Systems Biology. After undergrad, Louisa returned to Seattle to work in the lab of Dr. Michael Emerman at the Fred Hutchinson Cancer Research Center studying viral restriction factors under the guidance of Dr. Molly OhAinle. She then joined the Molecular Medicine and Mechanisms of Disease graduate program at the University of Washington in 2018 where she studied human stem cell derived kidney organoids under Dr. Beno Freedman. During her time at UW, she was awarded multiple research grants, worked as a venture analyst at the Washington Research Foundation, consulted with a cell therapy startup, Modulus Therapeutics, and explored the opportunities available through the Buerk Center for Entrepreneurship at UW's Foster School of Business. Louisa earned her Doctor of Philosophy from UW in 2022.